DEVELOPMENT OF METHANOL ELECTRO-OXIDATION CATALYSTS FOR DIRECT METHANOL FUEL CELL APPLICATION

BY

MUKHTAR BELLO

A Dissertation Presented to the

DEANSHIP OF GRADUATE STUDIES

KING FAHD UNIVERSITY OF PETROLEUM & MINERALS

DHAHRAN, SAUDI ARABIA

In Partial Fulfillment of the

Requirements for the Degree of

DOCTOR OF PHILOSOPHY

In

CHEMICAL ENGINEERING

JULY 2011

KING FAHD UNIVERSITY OF PETROLEUM & MINERALS
DHAHRAN, SAUDI ARABIA

DEANSHIP OF GRADUATE STUDIES

This dissertation, written by Mukhtar Bello under the direction of his dissertation advisor and approved by his dissertation committee, has been presented to and accepted by the Dean of Graduate Studies, in partial fulfillment of the requirements for the degree of DOCTOR OF PHILOSOPHY IN CHEMICAL ENGINEERING.

Dissertation Committee

Dr. S. M. Javaid Zaidi
(Dissertation Advisor)

Dr. Sleem-ur-Rahman
(Co-advisor)

Dr. Usamah Al-Mubaiyedh
(Department Chairman)

Prof. Adnan M. Al-Amer
(Member)

Dr. Salam Zummo
(Dean of Graduate Studies)

Dr. Shakeel Ahmed
(Member)

Date 16/7/2011

Prof. Ajayan Vinu
(Member)

DEDICATION

This work is dedicated to my parents, uncles and family.

ACKNOWLEDGEMENT

In the name of Allah, the most beneficent, the most merciful

All praises are due to Allah (SWT) for His guidance and continuous support for me. May the peace and blessings of Allah be upon His noble prophet, Muhammad, his household and companions.

I wish to express my appreciation to Ahmadu Bello University-Zaria, Nigeria, for awarding me a study fellowship, King Fahd University of Petroleum & Minerals, Dhahran, Saudi Arabia for providing the necessary facilities and support for my studies and National Institute for Materials Science – Japan for awarding me internship fellowship to carry out part of this work. Also, I am grateful to the Faculty Members, Staff, and Technicians of the Chemical Engineering Department, King Fahd University of Petroleum & Minerals for their support.

With deep sense of gratitude, I would like to express my appreciation to my thesis committee members: Dr. S. M. Javaid Zaidi, Dr. Sleem-ur-Rahman, Dr. Shakeel Ahmad, Prof. Adnan Al-Amer and Prof. Ajayan Vinu for their immense contributions and support throughout the period of this work. I thank them very much for their excellent cooperation, friendliness and unlimited accessibility. I am also grateful for the moral support of Prof. Abdallah A. Shaikh and Prof. Naim M. Faqir. Special thanks to the ChE Department Laboratory and Secretariat Staff: Mr. Kamal Mahgoub, Mr. Mofiz, Mr. Mariano, Mr. Romeo, Hejji Taher Al-Helaili, Abdallah M. Al-Khalaf, Shaji K. Thaniyullah and Jefrey A. Comedia. I also thank Mr. Farooq (glass blower, Chemistry Dept.) for his assistance in fabricating some equipment used in this work. Furthermore, I wish to acknowledge the cooperation and support of Prof. Vinu's research group members during my internship visit, especially, Mr. Anand, Mr. Mano and Ms Rajeshree.

I thank all the members of our Research Group, in particular, Dr. Amir Al-Ahmed and all the Chemical Engineering Graduate Students, especially my office mate, Mr. Muhammad Al-Ya'ari. Also, I highly appreciate the good relationship and support of the Nigerian Community in Dhahran/Damman.

Finally, but very importantly, special thanks to my wife Saudatu for her love, support and patience, my daughter Maryam (Daddy's Princess) for making me happy most of the time, all my relatives and friends for their continuous prayers and enduring missing me among them.

TABLE OF CONTENTS

TITLE PAGE

LIST OF TABLES

TABLE PAGE

LIST OF FIGURES

TITLE PAGE

ABSTRACT

NAME OF STUDENT **Mukhtar Bello**

TITLE OF STUDY **Development of Methanol Electro-Oxidation Catalysts for Direct Methanol Fuel Cell Application**

MAJOR FIELD **Chemical Engineering**

DATE OF DEGREE **July 2011**

Low activity of the methanol electro-oxidation catalysts and poisoning of the catalysts by intermediate organic compounds produce during the reaction is one of the biggest challenges facing the direct methanol fuel cell (DMFC) technology. In this work, several catalysts were prepared for methanol electro-oxidation. In the first part, performance of PtRu catalysts supported on mesoporous carbon nitrides (MCN) was studied and compared with the performance of PtRu supported on Vulcan XC-72 and multi-walled carbon nanotubes. The MCN was synthesized using SBA-15 as a template with different aging temperatures of 100, 130 and 150 °C. The Pt-Ru/MCN-150 catalyst showed the highest activity, about 30% more than that of the commercial Pt-Ru/C (E-TEK).

In the second part, a novel approach was used to prepare Pt-Ru/Fe_2O_3-MC, Pt-Ru/CoO-MC and Pt-Ru/NiO-MC catalysts by synthesizing high surface area Fe_2O_3-MC, CoO-MC and NiO-MC and then followed by impregnation with PtRu. The Pt-Ru/NiO-MC catalyst showed the highest activity, about 18% greater than the commercial Pt-Ru/C (E-TEK).

In the third part, Pt/CeO_2-MC, Pt/PrO_2-MC, Pt/NdO_2-MC, and Pt/SmO_2-MC catalysts were prepared by synthesizing high-surface area CeO_2-MC, PrO_2-MC, NdO_2-MC, and SmO_2-MC, followed by impregnation with Pt. The Pt/CeO_2-MC catalyst showed the highest activity, about 3.5% more than that of the commercial Pt-Ru/C (E-TEK) catalyst.

All the prepared catalysts showed reasonable stability. The metal nano-oxides & catalysts were characterized using FESEM, BET surface area, FT-IR, UV-Vis, EDS and XRD.
Finally, from the cyclic voltammetric results, Pt-Ru/MCN150, Pt-Ru/MCN130, Pt-Ru/MCN100, Pt-Ru/F-MWCNTs, Pt-Ru/Vulcan XC-72, and Pt-Ru/C (E-TEK) were selected and used to fabricate membrane electrode assemblies (MEAs). The MEAs were tested in a practical DMFC. The MEA in which Pt-Ru/MCN150 was used as the anode catalyst showed the highest power density of 56.3 mW/cm^2 at 80 °C.

Doctor of Philosophy
King Fahd University of Petroleum & Minerals
Dhahran, Saudi Arabia
July2011

الخلاصة

تعتبر الفعالية المنخفضة لحفازات الأكسدة الكهربائية للميثانول، و تسمم هذه الحفازات - ببعض المركبات العضوية البينية المنتجة خلال التفاعل- أحد التحديات الكبيرة التي تواجة تقنية خلية وقود الميثانول المباشر. في هذه الدراسة، تم تحضيرالعديد من حفازات الأكسدة الكهربائية للميثانول. في الجزء الأول، تمت دراسة أداء حفازات (البلاتين-الذهب) المدعومة بنتريدات الكربون الميزومسامية. كما تمت مقارنة أداءها مع أداء حفازات (البلاتين-الذهب) المدعومة بال(فولكان -72) والمدعومة أيضا" بالأنابيب النانومترية الكربونية المتعددة الجدران. أنتجت نتريدات الكربون الميزومسامية بإستخدام ال (إس بي إيه-15) كإطار عند 100، 130 و 150 درجة مئوية. في هذه الدراسة، وجد أن حفازات (البلاتين-الذهب)- المدعومة بنتريدات الكربون الميزومسامية المنتجة عند 150 درجة مئوية- هي أعلى الحفازات فعالية، و تفوق الحفازات التجارية- المعروفة ب(إي-تيك)- بحوالي 30%.

في الجزء الثاني، تم إعداد حفازات (البلاتين-الذهب) بإستخدام منهجية جديدة و ذلك بتخليق مساحة سطحية عالية وذلك بإضافة أكاسيد الحديد، والكوبلت والنيكل لدعامة الكربون الميزومسامية، بعدها يتم التطعيم بالبلاتين والذهب. فعالية الحفازات المدروسة تناقصت-إعتمادا" على أكاسيد المعادن المضافة- على النحو التالي:

المدعومة بإضافة أكسيد النيكل> المدعومة بأكسيد الكوبلت> المدعومة بأكسيد الحديد الثلاثي> إي-تيك

في الجزء الثالث، تم إعداد حفازات البلاتين المدعومة بالكربون الميزومسامي المضاف له أكاسيد السيريوم، البراسيوديميوم، النيوديميوم والساماريوم (لتخليق مساحة سطحية عالية) متبوعة" بتطعيمها بالبلاتين. أظهرت النتائج أن حفاز البلاتين المدعوم بالكربون الميزومسامي المضاف له أكسيد السيريوم هو الأعلى فعالية، و يفوق الحفازات التجارية المعروفة بال (إي-تيك) بحوالي 3.5 %.

أظهرت كل الحفازات- المعدة في هذه الدراسة- ثباتية مقبولة. درست خصائص الحفازات و المعادن ذات الأكاسيد النانومترية- المعدة في هذه الدراسة- بإستخدام التقنيات التاليه:

FESEM, BET surface area, FT-IR, UV-Vis, EDS and XRD

أخيرا"،من خلال نتائج الفولتية الدورية،ولصناعة الأغشية القطبية أختيرت حفازات ال(إي-تيك) و حفازات (البلاتين-الذهب)التالية:المدعومة بنتريدات الكربون الميزومسامية عند(150، 130 و 100 درجة مئوية)،المدعومة بال(إف) أنابيب الكربون النانومترية المتعددة الجدران، المدعومة بال(فولكان-72). بعد ذلك تم إختبار الأغشية القطبية المصنعة في تقنية خلية وقود الميثانول المباشر. أعلى كثافة طاقة – بمقدار 56.3 ملي وات لكل سنتيمتر مربع عند 80 درجة مئوية- أنتجت عند إستخدام حفازات (البلاتين-الذهب) المدعومة بنتريدات الكربون الميزومسامية، كحفازات أنودية.

CHAPTER 1

1. INTRODUCTION

Within the last two decades, the search for more efficient and cleaner energy conversion technologies and the need for alternative renewable fuels have increased the interest on fuel cell research and development. Fuel cells are seen as promising energy conversion technologies for the 21st century due to their high efficiency, flexibility in power supply and environmental friendliness. The electrochemical reactions taking place in fuel cells produce significantly less amount of by-products that pollute the planet in comparison with the chemical combustion occurring in conventional energy conversion devices such as an internal combustion engine. Fuel cells can generate power from a fraction of watt to thousands of kilowatts. Because of this, they can be used in almost every application where local electricity generation is needed. Application of fuel cells in stationary power generation, automobiles and portable electronics have been demonstrated [1].

A fuel cell is an electrochemical engine which continuously converts the chemical energy of a fuel into direct current electrical energy. This is similar to the combustion process which occurs in a heat engine, but in a fuel cell this can take place at much lower temperature, high energy efficiency and reduced polluting emissions. For these

reasons, fuel cells are expected to play an important role in the replacement of the internal combustion engine. A fuel cell is also similar to a battery in some aspects. It has an electrolyte, negative and positive electrodes, and it generates direct current electricity through electrochemical reactions. However, unlike a battery, a fuel cell supplies power as long as there is a supply of fuel and oxidant. Also, the electrodes in a fuel cell do not undergo chemical changes.

There are several kinds of fuel cells and a lot of research has been carried out and is currently being conducted on the different types of fuel cells. Hydrogen as an energy carrier is the common fuel for fuel cells but is not readily available. Presently organic fuels are steam reformed to hydrogen-rich gas before entry into the anode side of a fuel cell. The size of the system due to the presence of the reformer complicates the design. In addition, because the concept of "Hydrogen Energy Economy" is yet to be fully realized there are no infrastructural networks to support the distribution of hydrogen easily and its storage is equally challenging. Thus, research efforts are geared towards designing a fuel cell that would directly oxidize a liquid fuel at the anode and will have improved overall cell performance.

Direct methanol fuel cell (DMFC), where methanol (CH_3OH) fuel is supplied directly to the anode of the cell is one of the promising candidates. Much attention is now focused on it worldwide especially in the US, Canada, Japan, and Germany. DMFC technology is attractive for the automobile and electronic industries. Recently, it has been receiving increasing attention as a power source for small portable electronic devices, such as military navigation equipment, laptops and mobile phones [1]. It has

the advantage of not requiring a fuel reformer, which allows simple and compact design. For the transportation sector, the existing gasoline transportation infrastructure can be used without significant changes. Furthermore, variation in power demand can be accommodated simply by alteration in supply of CH_3OH feed and because of its low operating temperature there is no production of NO_X [2]. As a fuel, CH_3OH has some advantages over hydrogen; it is liquid at room temperature and pressure, it requires no preprocessing modules such as reformers, it is stable in contact with acidic membranes, has limited toxicity, high energy density (3800 kcal/liter) compared to hydrogen at 360 atm (658 kcal/liter) and low theoretical electro-oxidation potential ($E°$) comparable to that of hydrogen. In addition, it is cheaper to manufacture and easier to handle and transport [3].

However, despite these advantages, there are two major constraints inhibiting large scale commercialization of the DMFC. Firstly, problems relating to Nafion® membranes, which are used as polymer electrolyte membranes. Nafion® membranes permit CH_3OH crossover from the anode to the cathode and are costly [4]. In addition, its proton conductivity decreases at high temperature ~ above 90 °C. The crossover is caused by diffusion of CH_3OH due to concentration gradient and by molecular transport due to electro-osmotic drag. The CH_3OH transported through the membrane reduces the effective area of the cathode by utilizing cathode Pt sites for the direct reaction between the CH_3OH and oxygen. This leads to secondary reactions, mixed potentials, decreasing energy and power density, generation of additional water that must be managed, increasing oxygen stoichiometric ratio, and hence reduced overall performance [5]. However, a lot of progress has been achieved in solving the CH_3OH

crossover problem by modifying the Nafion® membranes and developing alternative membranes such as composite SPEEK membranes and sulfonated polystyrene/poly-tetrafluoroethylene (SPS/PTFE) composite membranes [6-12].

Secondly, low activity of the CH_3OH electro-oxidation catalysts and poisoning of the catalysts by the intermediate organic compounds such as carbon monoxide (CO), which are produced during the CH_3OH electro-oxidation reaction [13]. Operating the fuel cell in the temperature range up to around 150 °C would improve the reaction kinetics and reduce the catalyst poisoning by the CO but this causes dehydration of the membrane, which leads to a drastic reduction of the DMFC performance. Researchers around the world have made serious efforts to develop high-performance catalysts that will enhance the CH_3OH electro-oxidation and reduce the poisoning effects of the organic intermediates [14-33]. Three approaches are being pursued: finding better support material, determining suitable combination of active species and devising a more prudent preparation technique. CH_3OH electro-oxidation occurs according to the following reaction [34]:

$$CH_3OH + H_2O \rightarrow CO_2 + 6H^+ + 6e^- \qquad E^o = 0.02V \qquad (1)$$

The reaction is a combination of adsorption and electrochemical reaction on a catalyst surface. Pt has shown the highest activity for the electro-oxidation of CH_3OH in an acid environment compared to any other single-metal catalyst. However, Pt is very expensive and CH_3OH electro-oxidation on Pt is a self-poisoning reaction that produces intermediate CO and other organic intermediates that strongly adsorb on the Pt surface thereby poisoning the catalyst. Many binary and ternary catalysts for

CH_3OH electro-oxidation have been investigated and reported in the literature, most of them based on modification of Pt with some other metal (s) [13-24]. The role of the other metal is mainly to provide O-containing surface species at low potentials, which helps to remove the CO_{ads} in order to free the Pt surface thereby enhancing the catalysts' performance. Among various catalyst formulations, there is a general consensus that PtRu alloy offers the most promising results for the CH_3OH electro-oxidation. Extensive research has been conducted on CH_3OH electro-oxidation using supported PtRu binary catalysts [25-33].

The first part of this work involves finding the best support material for the PtRu binary catalyst. In order to achieve high catalysts utilization, the PtRu metals are usually dispersed on a support material. Compared to bulk metal catalysts, supported catalysts normally exhibit higher performance. Carbon materials are mostly used as support for the CH_3OH electro-oxidation catalysts because of their relative stability in both acidic and alkaline media, good electrical conductivity and high surface area. However, the type of carbon material used in preparing a catalyst has a strong influence on its properties (such as metal particle-size, dispersion, morphology, alloyed degree, etc) and performance (activity and stability). Therefore, the choice of an appropriate carbon support is very important in preparing the CH_3OH electro-oxidation catalysts for DMFC application. The properties of a support material needed to prepare an excellent electro-catalyst include: sufficiently high surface area, reasonable porosity, suitable surface functional groups, right morphology, good electronic conductivity, high corrosion resistance, and low-cost. Among these factors,

specific surface area has a significant effect on the preparation and performance of supported catalysts [34, 35].

Previously, carbon blacks such as Vulcan XC-72 and Ketjen Black were the only support materials used for fuel cell electro-catalysts. However, Ketjen Black supported catalysts showed high ohmic resistance and mass transport limitations during fuel cell operation [34]. Thus, Vulcan XC-72 has been the dominant carbon black support material employed in CH_3OH electro-oxidation catalysts preparation. With the advent of nanotechnology, nano-structured carbon materials such as carbon nanotubes, graphitic carbon nanofibers, nanocoils etc have been investigated as support materials for CH_3OH electro-oxidation catalysts [36-45]. Results of the various studies revealed that nano-structured materials particularly carbon nanotubes showed improved CH_3OH electro-oxidation catalysts performance compared to when Vulcan XC-72 is used as the support material.

Recently, mesoporous carbons (a new family of carbon materials, in which ordered mesoporous silicas or nano-sized silica spheres are used as templates) are beginning to attract attention for use as support material for the CH_3OH electro-oxidation catalysts. Although research is still in its infancy regarding their use as the support material for CH_3OH electro-oxidation catalysts, they have great potentials due to their high surface area, large pore volume, tunable pore size and highly interconnected uniform pore structure. Several researchers have successfully synthesized mesoporous carbon materials with an ordered pore structure using different methods [46-51]. Thus, in the first part of this work, mesoporous carbon nitride (MCN) was

synthesized using SBA-15 as a template with different aging temperatures of 100, 130, and 150 °C. For the first time, the synthesized MCN was used as support materials to prepare Pt-Ru catalysts and to compare their catalytic performance for the CH_3OH electro-oxidation with Pt-Ru catalyst prepared using commercial multi-walled carbon nanotubes (MWCNTs) and Vulcan XC-72 supports.

In the second part of this work, a novel approach was used to prepare ternary CH_3OH electro-oxidation catalysts. From the literature review carried out, diverse methods have been reported that are used to prepare the PtRu-based catalysts for CH_3OH electro-oxidation. Catalyst composition and method of preparation are known to immensely affect the physical properties and electrochemical performance of a catalyst. Thus, there is the need to use a carefully selected approach in order to prepare a catalyst with the highest attainable performance. Incorporation of transition metals into the Pt-Ru catalysts to form ternary catalysts in order to improve the performance of the Pt-Ru catalysts is one of the techniques attracting a lot of interest. Based on theoretical screening results, it has been reported that alloying Pt-Ru with Fe, Co, Rh, Ir and Ni could provide higher activity than the Pt-Ru catalyst [22].

Previous study has also shown that alloying Pt with Fe could weaken the Pt-CO_{ads} bonding, which will result in easy electro-oxidation of the CO_{ads} [52]. Ternary catalysts such as Pt-Ru-Ir, Pt-Ru-Ni, Pt-Ru-Fe and Pt-Ru-Co have all been investigated and reported in the literature [53-55]. To the best of my knowledge, in all the published literature, the Pt, Ru and third metal are dispersed simultaneously into the support material. In this work, a novel approach was used by first synthesizing

nano-oxides of Fe, Co, and Ni in mesoporous carbon, that is, Fe_2O_3-MC, CoO-MC and NiO-MC. Then the obtained high surface area of Fe_2O_3-MC, CoO-MC and NiO-MC were impregnated with the Pt-Ru nanoparticles respectively. The aim was to incorporate the transition metals while preparing the high surface area mesoporous carbon support, which allows excellent dispersion of the Pt-Ru nanoparticles.

The third part of this work deals with the development of active CH_3OH electro-oxidation catalysts without using the expensive Ru. The use of noble metals (Pt & Ru) contributes to the high cost of the CH_3OH electro-oxidation catalysts, which affects the overall cost of the DMFC. New CH_3OH electro-oxidation catalysts such as Pt-CeO_2/C, PtNi/C, PtOs/C, and PtFe/C have been investigated and reported in the literature [56-59]. Based on the promising results for the CH_3OH electro-oxidation using Pt-CeO_2/C previously reported, for the first time the prospect of using Pr, Nd, and Sm in combination with Pt to prepare catalyst for CH_3OH electro-oxidation was investigated in this work. In addition, the traditional Vulcan XC-72 support was not used instead a novel method was used to synthesis mesoporous carbon (MC)-based high surface area nanooxides of CeO_2-MC, PrO_2-MC, NdO_2-MC, and SmO_2-MC.

The support materials, the synthesized nano-oxides and the prepared catalysts samples: Pt-Ru/MCN100, Pt-Ru/MCN130, Pt-Ru/MCN150, Pt-Ru/F-MWCNTs, Pt-Ru/Vulcan XC-72, Pt-Ru/FeO-MC, Pt-Ru/CoO-MC, Pt-Ru/NiO-MC, Pt/CeO_2-MC, Pt/PrO_2-MC, Pt/NdO_2-MC and Pt/SmO_2-MC were characterized using FESEM, BET surface area, EDX, FT-IR, UV-Vis and XRD. The catalysts performance was studied using cyclic voltammetry and compared with the commercial Pt-Ru/C (E-TEK).

1.1 Objectives

The overall objective of this dissertation work is to develop new catalysts for electro-oxidation of CH_3OH for direct methanol fuel cell (DMFC) application. Specific objectives are:

1. To functionalize multi-wall carbon nanotubes and synthesis mesoporous carbon nitrides (MCN) support materials.
2. To characterize the prepared support materials using FESEM, FTIR, UV-Vis, XRD and BET surface area.
3. To develop CH_3OH electro-oxidation catalysts using active metal species such as Pt, Ru, Fe, Co, Ni and CeO_2 together with the prepared support materials.
4. To characterize the prepared catalysts using EDS and XRD.
5. To study the effects of the different support materials and preparation technique.
6. To study the CH_3OH electro-oxidation activity of the prepared catalysts using cyclic voltammetry (CV).
7. To use the catalyst systems that exhibit promising results from the CV test to fabricate membrane electrode assemblies (MEAs).
8. To determine the performance of the MEAs in a practical DMFC.

CHAPTER 2

2. LITERATURE REVIEW

2.1 Fuel Cells

The concept of fuel cell has been in existence since 1839 when Sir William Robert Grove showed that the electrolysis of water is a reversible process [60 61]. He demonstrated the first working prototype, which represents the foundation stone for today's fuel cell technology. It was first named as "gas battery". The prototype consisted of two platinum electrodes which were separately surrounded by a glass cylinder. One of the cylinders was filled with hydrogen the other with oxygen. Both electrodes were immersed in diluted sulphuric acid, which was the electrolyte and created the electric connection. The term "*fuel cell*" was coined later in 1889 by Ludwig Mond and Charles Langer, who attempted to build the first practical device using air and industrial coal gas [62].

Friedrich Wilhelm Ostwald (1853 -1932), who was a Professor of Physical Chemistry and an expert in energy, provided much of the theoretical understanding of how a fuel cell operates [63]. In 1893, he experimentally determined the interconnected roles of the various components of the fuel cell: electrodes, electrolyte, oxidizing and reducing agents, anions, and cations. In addition, he provided the basic

thermodynamic equations showing the definite advantages of "Low Temperature Electrochemical Oxidation" over "High Temperature Combustions" of fuels. He built his home into a large laboratory and library and called it "*The House of Energy*". Keeping the name, it is, nowadays, a centre of studies and conferences and expectedly, an exhibition of Ostwald's work in science and philosophy [5]. Further early attempts carried on into the early 1900's but the development of the internal combustion engine made further research into the technology unnecessary.

Francis Thomas Bacon developed the first successful fuel cell in 1932, running on pure O_2 and H_2 and using an alkaline catalyst and nickel electrodes [62]. In 1954, at an exhibition in London, Bacon demonstrated a six-cell battery that produced 150 W, operating at 15 bars and 200 °C, having electrodes 5 inches in diameter. In 1956, Bacon and his staff of 14 began development of a larger battery with 40 cells to show that a particular size of battery could be built. They received support from the National Research Development Corporation in the UK and after three years a 6-kW fuel cell stack was completed [64]. It was used to power a fork-lift truck, welding equipment and a circular saw. Recent years have seen an upsurge in interest in fuel cells for a range of applications, particularly for stationary power generation and automobiles. Depending on the load, fuel cell type and conditions of operation a single cell has a potential of 0.5V to 1.0 V. To yield a sufficiently high voltage, a number of single cells are usually connected electrically in series in form of a stack.

2.2 Types of Fuel Cells

Fuel cell systems can be classified according to the working temperature: High, medium and low (ambient) temperature systems or referring to the pressure of operation: high, medium and low (atmospheric) pressure systems. They may be further distinguished by the fuels and/or the oxidants they use. For practical reasons fuel cell systems are simply distinguished by the type of electrolyte used. The following names and abbreviations are now frequently used in publications: Alkaline fuel cells (AFC), proton exchange membrane fuel cells (PEMFC), direct methanol fuel cells (DMFC), phosphoric acid fuel cells (PAFC), molten carbonate fuel cells (MCFC), and solid oxide fuel cells (SOFC) [5]. Table 2-1 shows the classification.

Table 2-1: Types of Fuel Cells

Fuel Cell System	Fuel	Electrolyte	Ion Conduc-tion	Operating Temperature (°C)	Efficiency (%)	Application Area
AFC	H_2	KOH	OH^-	60-90	50-60	Space Application
PEMFC	H_2, Reformate	Polymer Membranes	H^+	50-80	50-60	Automobile
DMFC	CH_3OH	Polymer Membranes	H^+	50-150	50-55	Automobile/Por-table Power Generation
PACF	H_2, Reformate	Phosphoric Acid	H^+	160-220	55-60	Stationary Power Generation
MCFC	H_2, CO	Li_2CO_3/Na_2CO_3	H^+	620-660	60-65	Stationary Power Generation
SOFC	H_2, CH_4,	ZrO_2/Y_2O_3	H^+	800-1000	55-65	Stationary Power Generation

2.3 Direct Methanol Fuel Cell (DMFC)

Although the power efficiencies of PEMFC (which uses H_2) continue to show steady improvements, there remain problems with the use of hydrogen as the active fuel: either this hydrogen must be obtained by in situ reformation of solid or liquid C-H fuels, such as petroleum, coal or methanol, or it must be pre-purified and stored as the gas under pressure, or in the form of an admixture with a metal alloy, carbon or some other absorbents [65]. In all of these cases, either there is a considerable weight penalty or there is increased engineering complexity, adding to costs. It remains highly desirable to design a fuel cell that would directly oxidize a liquid fuel at the anode, but retain the high power/weight ratio of the solid-polymer electrolyte fuel cells. One such fuel cell now under active development in many countries around the world is the DMFC. It has many advantages as mentioned earlier. The use of CH_3OH directly as an electrochemically active fuel simplifies the design complexity and lowers the cost. Figure 2-1 shows a schematic of a DMFC [66].

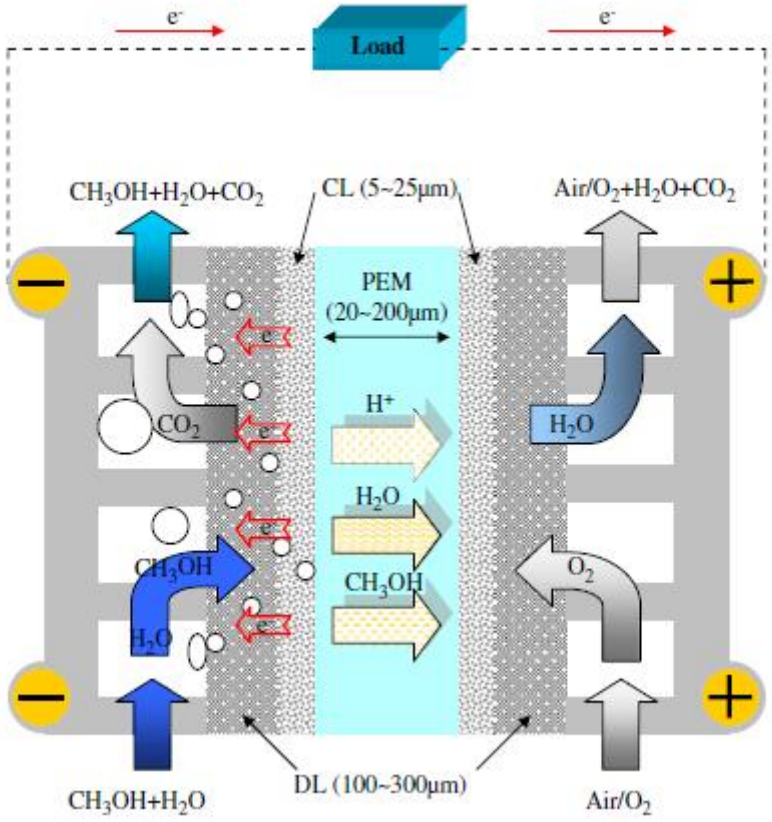

Figure 2-1: Schematic of Direct Methanol Fuel Cell

$$Anode: CH_3OH + H_2O \rightarrow CO_2 + 6H^+ + 6e^- \quad \text{.....(2.1)}$$

$$Cathode: 1.5O_2 + 6H^+ + 6e^- \rightarrow 3H_2O \quad \text{.....(2.2)}$$

$$Overall: CH_3OH + 1.5O_2 \rightarrow CO_2 + 2H_2O \quad \text{.....(2.3)}$$

The basic problems being faced by the direct methanol fuel cell are [65]:

- The anode reaction has poor electrode kinetics, particularly at lower temperatures, making it highly desirable to identify improved catalysts and to work at as high a temperature as possible.
- The cathode reaction, the reduction of oxygen, is also slow: the problems are particularly serious with aqueous mineral acids, but perhaps not so serious with acidic polymer membranes. Nevertheless, the overall power density of the direct methanol fuel cells is much lower than the 600+ mW cm^{-2} envisaged for the hydrogen fuelled solid polymer electrolyte fuel cell (SPEFC).
- The stability and permeability of the current perfluorosulfonic acid membranes to CH_3OH, allowing considerable fuel crossover, and, at the higher temperatures needed to overcome limitations in the anode kinetics, degradation of the membrane both thermally and through attack by CH_3OH itself.
- The fact that CH_3OH can permeate to the cathode leads to poor fuel utilization, the appearance of a mixed potential at the cathode, since conventional cathode catalysts are based on platinum, which is highly active for CH_3OH electro-oxidation at the higher potentials encountered at the cathode. Experimentally, this problem has been tackled both by seeking alternative oxygen reduction catalysts and by increasing the Pt loading substantially; the latter clearly increases costs significantly.

In spite of the above difficulties, the DMFCs have the capability of being very cheap and potentially very competitive with the internal combustion engine, particularly in niche city driving applications, where the low pollution and relatively high efficiency

at low load are attractive features. Performances from recent single cells are highly encouraging especially with the tremendous efforts being made by researchers worldwide.

2.4 Methanol Electro-oxidation Kinetics

2.4.1 Methanol Electro-oxidation Reaction Mechanism

The kinetic of CH_3OH electro-oxidation is complex because the reaction mechanism involves adsorption of CH_3OH and several reaction steps including the oxidation of adsorbed carbon monoxide ($CO_{ads)}$. Figure 2-2 shows a possible network of reaction pathways by which the electrochemical oxidation of CH_3OH occurs [67]. From the Figure, it can be observed that a number of intermediate compounds such as formaldehyde (CH_2O), formic acid (HCOOH) and carbon monoxide (CO) are produced from the intermediates CH_2OH and CHOH. The *x* represents the Pt site. The yields of oxidation products depend on the CH_3OH concentration, temperature, electrode roughness and reaction time [68]. Several studies have been conducted to analyze possible reaction pathways in order to find the main pathway of CH_3OH electro-oxidation [69–72]. However, most studies conclude that the reaction can proceed via multiple mechanisms. Nevertheless, it is widely accepted that the most significant reactions are the adsorption of CH_3OH and the oxidation of CO_{ads}.

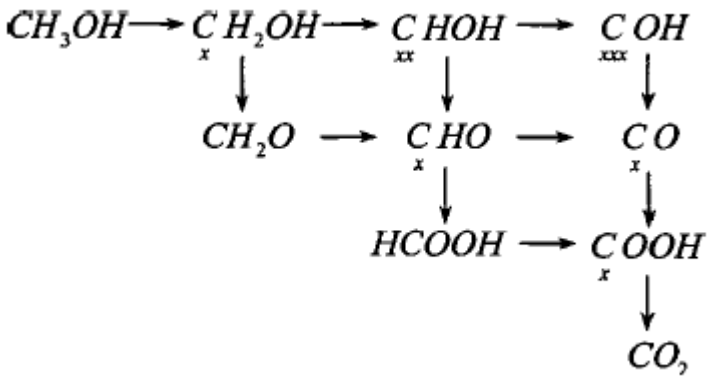

Figure 2-2: Reaction Pathways of Methanol Electro-Oxidation

Therefore, in order to prepare excellent methanol electro oxidation catalysts, it is important that the basics of CH_3OH adsorption and CO_{ads} oxidation are properly understood. The CH_3OH adsorption & its electrochemical reaction on a catalyst surface and CO_{ads} oxidation can be represented as follows [72]:

$$CH_3OH_{sol} + Site(Pt) \rightarrow (CH_3OH)_{ads} - Pt \rightarrow (CO)_{ad} - Pt + 4H^+ + 4e^- \quad (2.4)$$

$$(CO)_{ads} - Pt + Pt + H_2O \rightarrow (CO)_{ads} - Pt + (OH)_{ads} - Pt + H^+ + e^- \rightarrow 2Pt + CO_2 + 2H^+ + 2e^- \quad (2.5)$$

From Figure 2-2, it is postulated that the CH_3OH adsorption takes place in several steps, forming different species due to the dissociation of the CH_3OH molecule. However, establishing the nature of the adsorbed species formed during the adsorption of small organic molecules is a difficult task. In the 1980s, the use of analytical techniques for the in situ, ex situ and online analysis of the electrode surface began [73]. For the CH_3OH adsorption and subsequent dissociation, different

adsorbed species were suggested on the basis of data from infrared spectroscopy and thermal-desorption mass spectroscopy [69-71].

Infrared spectra obtained during CH_3OH adsorption at 0.35V on polycrystalline Pt show well characterized bands for linearly adsorbed CO at approximately 2040 cm-1 together with other bands in the 1200-1300 cm-1 region, which have been interpreted in terms of the C-OH stretching of hydrogenated species such as COH or HCOH [34]. These bands were also observed in spectra obtained on single crystal Pt (100) and Pt (111). Another approach to establish the nature of the adsorbate was made by thermal-desorption mass spectroscopy, performed on electrodes transferred into UHV [70]. The results also confirmed the presence of hydrogenated species after adsorption of methanol. The data further showed that the ration between the amount of CO and hydrogenated species depends on methanol concentration. The discrepancy of results among different research groups is attributed in part to the variation in experimental approaches.

In general, it's believed that there are parallel reaction paths with different oxidation products yields depending on the potential, time, and surface structure and composition of the electrode. As mentioned earlier, among all the processes, the adsorption of CH_3OH and CO_{ads} oxidation are the most distinguishable and thus considered the most important. Different research groups have made effort to determine whether adsorption of CH_3OH or oxidation of CO_{ads} is the rate determining step. It was observed that at all potentials between 0.40 and 0.70V, there is enough adsorbed CH_3OH on the surfaces of both Pt (111) and Pt (110) as to reach maximum

rate of oxidation at the respective potential [34]. Several other studies support this finding [74-75]. Thus, there seems to be consensus that the CO_{ads} oxidation process and not the CH_3OH adsorption is the rate-determining step. Analysis of IR results showed that it is possible to follow the pathway leading to CO_2 via formation of CO_{ads} [34]. However, it has been reported that interaction of H_2O with the Pt surface increases as the potential is made more positive and competition of CH_3OH with H_2O for adsorption sites becomes important [76]. Therefore, at high potentials (above 0.70V) CH_3OH adsorption becomes the rate determining step and for this reason the reaction rate passes through a maximum and then decays [77]. In the case of Pt-Ru, CH_3OH oxidation is summarized as follows:

$$CH_3OH + PtRu \rightarrow CO_{ads} - PtRu + 4H^+ + 4e^- \quad (2.6)$$

$$CO_{ads} - PtRu + H_2O \rightarrow CO_{ads} - PtRu - OH_{ads} + H^+ + e^- \\ \rightarrow PtRu + CO_2 + 2H^+ + 2e^- \quad (2.7)$$

The presence of Ru is believed to enhance the electro-oxidation kinetics of the CH_3OH. Electrochemical impedance spectroscopy study carried out for the CH_3OH electro-oxidation using Pt/C and a well-alloyed PtRu/C has confirmed that Ru does enhance the CH_3OH electro-oxidation [72]. A thin film electrode method in a half-cell configuration was employed to study the intrinsic behavior of the anodic process. The impedance data were correlated with voltammetry studies of the oxidation of pre-adsorbed CO_{ads}.

The voltammograms of CO_{ads} oxidation on Pt/C and PtRu/C are shown in Figure 2-3 [72]. The onset of CO_{ads} oxidation was observed at ~ 600 mV vs. RHE on Pt/C and at ~ 350 mV vs. RHE on PtRu/C, which indicates the promotional effect of the Ru on the CO_{ads} oxidation. The enhancement of the CH_3OH oxidation rate on Pt-Ru catalysts in comparison to Pt catalysts is attributed to the ability of Ru to adsorb OH radicals at less positive potentials than Pt. Since Pt is more active for the CH_3OH adsorption than Ru, overall reaction on Pt-Ru electro catalysts was reported to obey a bifunctional mechanism [78].

The term was suggested to give emphasis on the joint activities of both the metals, Pt being the one adsorbing and dissociating CH_3OH and Ru, the one oxidizing the CO_{ads} at low potentials. This description of the mechanism is based on the observation that at potentials below 0.4V, Pt is a good catalyst for CH_3OH adsorption, but not for H_2O dissociation while Ru is able to dissociate H_2O but cannot adsorb CH_3OH (except at high temperature). Thus, according to this mechanism, CH_3OH is dissociatively adsorbed on Pt sites giving CO_{ads} and/or formyl-like species –CHO while H_2O dissociates on Ru sites giving OH_{ads}. Finally, following a Langmuir-Hinshelwood mechanism CO_{ads} reacts with OH_{ads} to form CO_2 [34]:

$$Pt + CH_3OH_{solution} \rightarrow Pt - CH_3OH_{ads} \rightarrow Pt - COH_{ads} + 3H^+ + 3e^- \rightarrow Pt - CO_{ads} + 4H^+ + 4e^- \quad (2.8)$$

$$Ru + H_2O \rightarrow Ru - OH_{ads} + H^+ + e^- \quad (2.9)$$

$$Pt - COH_{ads} + Ru - OH_{ads} \rightarrow Pt + Ru + CO_2 + 2H^+ + 2e^- \quad (2.10)$$

$$Pt - CO_{ads} + Ru - OH_{ads} \rightarrow Pt + Ru + CO_2 + H^+ + e^- \quad (2.11)$$

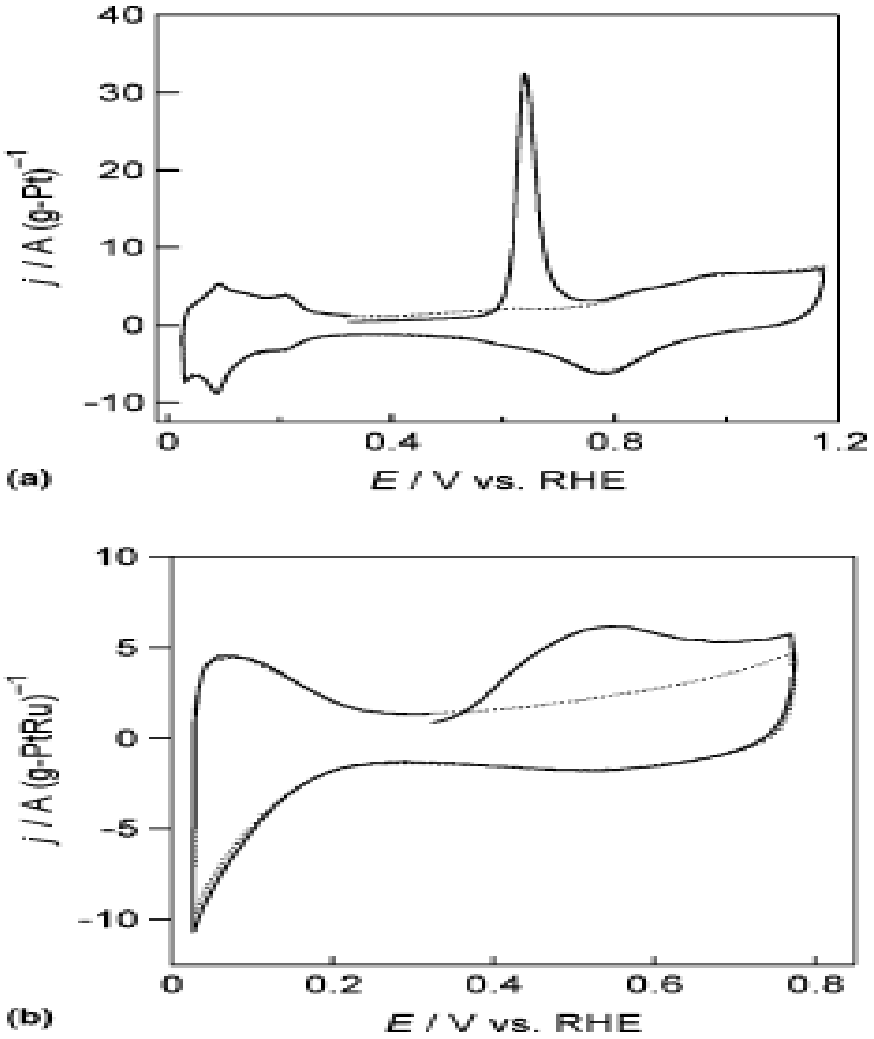

Figure 2-3: Pre-adsorbed CO Stripping Voltammograms on: (a) Pt/C and (b) PtRu/C in 0.5M H_2SO_4 at 60 ^oC

As a necessary condition for the Langmuir-Hinshelwood mechanism, CO must diffuse on the surface to the places where the OH_{ads} partner is formed. Furthermore, the relative rate of CO diffusion on the surface must be high.

2.4.2 Methanol Electro-oxidation Reaction Rate

Electrochemical reactions are mostly heterogeneous in nature. They involve the transfer of electrons released by the oxidation of a chemical species at the interface between an electrode and an electrolyte. The rate at which the electrons are released determines the speed at which an electrochemical reaction is taking place. The electrons released result in the generation of an electric current. Thus, the current generated by an electrochemical reaction is a direct measure of the rate of the electrochemical reaction. From the Faraday's law, the current indicates the rate of charge transfer as shown below [1]:

$$I = \frac{dQ}{dt} \tag{2.12}$$

where I is the current (*Ampere*), Q is the charge (*Coulombs*) and t is the time.

Equation (2.12) can be written in terms of the number of electrons (n) transferred:

$$I = nF\,\frac{dN}{dt} \tag{2.13}$$

where dN/dt is the rate of the electrochemical reaction (*mol/s*) and F is the Faraday's constant (96487 *C/mol*).

Integrating equation (2.13) gives the amount of charge produced:

$$\int_0^t I \, dt = nFN = Q \tag{2.14}$$

Therefore, the total amount of electricity generated is proportional to the number of moles of the reactant consumed in the electrochemical reaction. Similar to the conventional chemical reaction, the consumption of the reactant species is proportional to their surface concentration. For an oxidation reaction, the consumption rate (*mol/s*) is expressed as:

$$\frac{dN}{dt} = kC \tag{2.15}$$

where k is the oxidation rate coefficient and C is the surface concentration of the reacting species.

Combining equations (2.13) and (2.15) gives the current generated as:

$$I = nFkC \tag{2.16}$$

As mentioned earlier, the current I generated by an electrochemical reaction indicates the rate of the electrochemical reaction. However, most often current density (current per unit area) is used to show the extent of the reaction. The current density allows the reactivity of different surfaces to be compared on a per-unit basis. Here it's represented as i in units of amperes per square centimeter (A/cm^2):

$$i = \frac{I}{A} \tag{2.17}$$

where A is the interface area

It has been reported that for the CH_3OH electro-oxidation using Pt-Ru/C tested in a three-compartment electrochemical cell , the reaction order with respect to the CH_3OH is 0.5 while the reaction order with respect to the H^+ ions (from the $HClO_4$ electrolyte) is - 0.5 [79]. Thus, using equations (2.16) and (2.17) the CH_3OH electro-oxidation reaction rate can be represented as:

$$i = \frac{nF}{A} k C_{CH_3OH}^{1/2} C_{H^+}^{-1/2} \tag{2.18}$$

For an electrochemical reaction, the reaction rate constant (k) is given in terms of Gibbs free energy as follows [1]:

$$k = \frac{k_B T}{h} \exp\left(\frac{-\Delta G}{RT}\right) \tag{2.19}$$

where k_B and h are Boltzmann's constant and Planck's constant respectively

However, the Gibbs free energy that appeared in equation (2.19) consists of both chemical and electrical terms. For the oxidation reaction, the Gibbs free energy is given as:

$$\Delta G = \Delta G_{chemical} - \alpha F E \tag{2.20}$$

where α is the transfer coefficient and E is the potential.

The transfer coefficient expresses how the change in the electrical potential across the reaction interface changes the sizes of the forward versus reverse activation barrier.

Its value depends on the symmetry of the activation barrier. In electrochemical reactions such as the reactions taking place in fuel cells, the size of the activation barrier can be manipulated by varying the cell potential. Charged species are involved as either reactants or products in all electrochemical reactions. The free energy of a charged species is sensitive to voltage. Thus, changing the cell voltage changes the free energy of the charged species taking part in a reaction thereby affecting the size of the activation barrier [80].

The reaction order with respect to CH_3OH indicates that its adsorption obeys Temkin isotherm [79]. The same value for the reaction order and the coverage independent of the potential in the double-layer region of Pt has been reported for the single Pt catalyst [81, 82]. The similar behavior of Pt-Ru and Pt catalysts is to be expected because in Pt-Ru catalyst only Pt is active for the adsorption of CH_3OH at the temperatures below 60 $^{\circ}$C. A negative reaction order with respect to H^+ ions suggests that Ru- OH_{ads} is involved in the rate-determining step. If oxidative dissociation of H_2O on Ru sites given by Equation (2.9) is in equilibrium, the increase in the concentration of H^+ ions will cause a decrease in the Ru- OH_{ads} coverage.

In addition, the adsorption of OH particles on Ru sites seems to also follow the Temkin isotherm, because of the one-half reaction order with respect to H^+ [79]. The supporting electrolyte has an effect on the CH_3OH oxidation. $HClO_4$ and H_2SO_4 are the commonly used supporting electrolytes for the CH_3OH oxidation studies. The CH_3OH oxidation is affected by the anion of the supporting electrolyte. This is clearly the case for Pt (111) and Pt (100) electrodes, where cyclic voltammograms of CH_3OH

exhibits much larger currents in $HClO_4$ than in H_2SO_4 [83, 84]. The difference was justified by the specific adsorption of sulfate species at Pt electrodes, which partially hinder CH_3OH oxidation. No difference between $HClO_4$ and H_2SO_4 was observed at Pt (110).

Activation energy of about 70 $kJ\ mol^{-1}$ is considered as a reasonable value for a reaction like dissociative adsorption [74, 85]. However, the correlation between the CH_3OH oxidation rate and the pseudocapacitive current of OH adsorption on Ru that has been reported is rather conclusive that Ru- OH_{ads} is involved in the rate-determining step [79].

Rates expressions have also been developed considering the dissociative chemisorption of CH_3OH as the rate-limiting step in the CH_3OH electro-oxidation, in a direct methanol fuel cell [86]. The considered mechanism is:

$$(1) \quad 3Pt + CH_3OH \rightleftarrows Pt_3 - COH + 3H^+ + 3e^-$$

$$(2) \quad 3Ru + 3H_2O \rightleftarrows 3Ru - OH + 3H^+ + 3e^-$$

$$(3) \quad Pt_3 - COH + 2Ru - OH \rightleftarrows Pt - COOH + H_2O + 2Pt + 2Ru$$

$$(4) \quad Pt - COOH + Ru - OH \rightleftarrows CO_2 + H_2O + Pt + Ru$$

$$(5) \quad \tfrac{3}{2} O_2 + 6H^+ + 6e^- \rightleftarrows 3H_2O$$

The corresponding rate expressions are [86]:

$$r_1 = k_1 \exp\left(\frac{\alpha_1 F}{RT}\eta_a\right)\left\{\Theta_{Pt^3}\, C^{CL}_{CH_3OH} - \frac{1}{K_1}\exp\left(-\frac{F}{RT}\eta_a\right)\Theta_{Pt_3-COH}\right\} \quad (2.22)$$

$$r_2 = k_2 \exp\left(\frac{\alpha_2 F}{RT}\eta_a\right)\left\{\Theta_{Ru} - \frac{1}{K_2}\exp\left(-\frac{F}{RT}\eta_a\right)\Theta_{Ru-OH}\right\} \quad (2.23)$$

$$r_3 = k_3\left\{\Theta_{Pt_3-COH}\,\Theta^2_{Ru-OH} - \frac{1}{K_3}\,\Theta_{Pt-COOH}\,\Theta^2_{Pt}\,\Theta^2_{Ru}\right\} \quad (2.24)$$

$$r_4 = k_4\left\{\Theta_{Pt-COOH}\,\Theta_{Ru-OH} - \frac{1}{K_4}\,C^{CL}_{CO_2}\,\Theta_{Pt}\,\Theta_{Ru}\right\} \quad (2.25)$$

$$r_5 = k_5 \exp\left(\frac{\alpha_5 F}{RT}\eta_c\right)\left\{1 - \exp\left(-\frac{F}{RT}\eta_c\right)\left(\frac{p_{O_2}}{p^\theta}\right)^{3/2}\right\} \quad (2.26)$$

where k is the reaction rate constant, α is the charge transfer coefficient (0.5), F is the Faraday constant (96 487 C/mol), R is the universal gas constant (8.314 J/mol K), T is the temperature in K, η is the over potential, Θ is fractional surface coverage, C_i is the concentration of component i (mol/m^3), K is the equilibrium constant and p is the total pressure in Pa (θ is at standard condition).

The 1st step (2.22), which is the dissociative chemisorption of CH_3OH is considered to be the rate-determining step while the other steps (2.23 - 2.25) are assumed to be close to equilibrium. The fraction of platinum sites covered by the adsorb COH is related to the equilibrium constants and the unoccupied active platinum sites as follows [86]:

$$\Theta_{Pt_3-COH} = \frac{C^{CL}_{CO_2}}{\tilde{K}_2^3\, K_3\, K_4}\Theta^3_{Pt} \quad (2.27)$$

where

$$\tilde{K}_2 = K_2 \exp\left(\frac{F}{RT}\eta_a\right) \quad (2.28)$$

The fraction of unoccupied active platinum sites is given by:

$$\Theta_{Pt} = \sqrt[3]{-q + D^{0.5}} + \sqrt[3]{-q - D^{0.5}} \tag{2.29}$$

where

$$q = -\frac{\tilde{K}_2^3 K_3 K_4}{2C_{CO_2}^{CL}} \tag{2.30}$$

$$D = \left(\frac{\left(\tilde{K}_2 K_4 + C_{CO_2}^{CL}\right)\tilde{K}_2^2 K_3}{3C_{CO_2}^{CL}} \right)^3 + q^2 \tag{2.31}$$

The unsteady-state mass and charge balance for the species for the anode compartment, anode catalyst layer and cathode catalyst layer are [86]:

Anode compartment:

$$\frac{dC_{CH_3OH}}{dt} = \frac{1}{\tau}\left(C_{CH_3OH}^F - C_{CH_3OH}\right) - \frac{k^{LS} A^S}{V_a}\left(C_{CH_3OH} - C_{CH_3OH}^{CL}\right) \tag{2.32}$$

$$\frac{dC_{CO_2}}{dt} = \frac{1}{\tau}\left(C_{CO_2}^F - C_{CO_2}\right) - \frac{k^{LS} A^S}{V_a}\left(C_{CO_2} - C_{CO_2}^{CL}\right) \tag{2.33}$$

Anode catalyst layer:

$$\frac{dC_{CH_3OH}^{CL}}{dt} = \frac{k^{LS} A^S}{V_a^{CL}}\left(C_{CH_3OH} - C_{CH_3OH}^{CL}\right) - \frac{A^S}{V_a^{CL}} n_{CH_3OH}^M - \frac{A^S}{V_a^{CL}} r_1 \tag{2.34}$$

$$\frac{dC_{CO_2}^{CL}}{dt} = \frac{k^{LS} A^S}{V_a^{CL}}\left(C_{CO_2} - C_{CO_2}^{CL}\right) + \frac{A^S}{V_a^{CL}} r_1 \tag{2.35}$$

$$\frac{d\eta_a}{dt} = \frac{1}{C_a}\left(i_{cell} - 6Fr_1\right) \tag{2.36}$$

Cathode catalyst layer:

$$\frac{d\eta_c}{dt} = \frac{1}{C_c}\left(-i_{cell} - 6F\left(r_5 + n^M_{CH_3OH}\right)\right) \tag{2.37}$$

where τ is the mean residence time (s), C_f is the feed concentration (mol/m^3), k^{LS} is the mass transfer coefficient from liquid bulk to surface (m/s), A^S is the electrode cross sectional area (m^2), V_a is the anode compartment volume (m^3), V^F is the feed flow rate (ml/min), C_a & C_c anode and cathode double layer capacitance (F/m^2) respectively.

Considering steady-state conditions in the anode catalyst layer and the fact that at limiting current density the CH_3OH concentration in the anode catalyst layer is zero, the effective mass transfer coefficient is expressed as [86]:

$$k^{LS} = \frac{V^F i_{\lim}}{6F V^F C^F_{CH_3OH} - A^S i_{\lim}} \tag{2.38}$$

2.5 Mass Transfer in Porous Catalyst Media

Mass transfer is important in heterogeneous catalytic reactions because of the role diffusion plays during the process. There are seven (7) steps in a heterogeneous catalytic reaction [87]:

1. Diffusion of the reactants from the bulk fluid to the external surface of the catalyst pellet
2. Diffusion of the reactant from the pore mouth through the catalyst pores to the immediate vicinity of the internal catalytic surface
3. Adsorption of the reactant onto the catalyst surface

4. Reaction on the surface of the catalyst
5. Desorption of the products from the surface
6. Diffusion of the products from the interior of the pellet to the pore mouth at the external surface
7. Diffusion of the products from the external pellet surface to the bulk fluid

It is clear from the above steps that reactant needs to diffuse from the bulk fluid to the catalyst surface (active sites) while the product diffuses away from the catalyst surface to the external bulk fluid. However, in most cases there are some resistances to free-flow of the reactant and product. There are two kinds of diffusion resistance, that is, external and internal resistance. External diffusion resistance occurs due to the diffusion of the reactants or products between the bulk fluid and the external surface of the catalyst. On the other hand, the internal diffusion resistance is due to the diffusion of the reactants or products from the external pellet surface (pore mouth) to the interior of the pellet. Figure 2-4 shows a schematic representation of this two-step diffusion process [87]. However, for catalysts screening test using a small beaker-type electrochemical cell, it's assumed that both the external and internal diffusion resistances are negligible because the working electrode (catalyst surface) is directly immersed in the reactant solution (negligible external resistance) and the catalyst is in powder form with particle sizes in nanometer scale (negligible internal resistance).

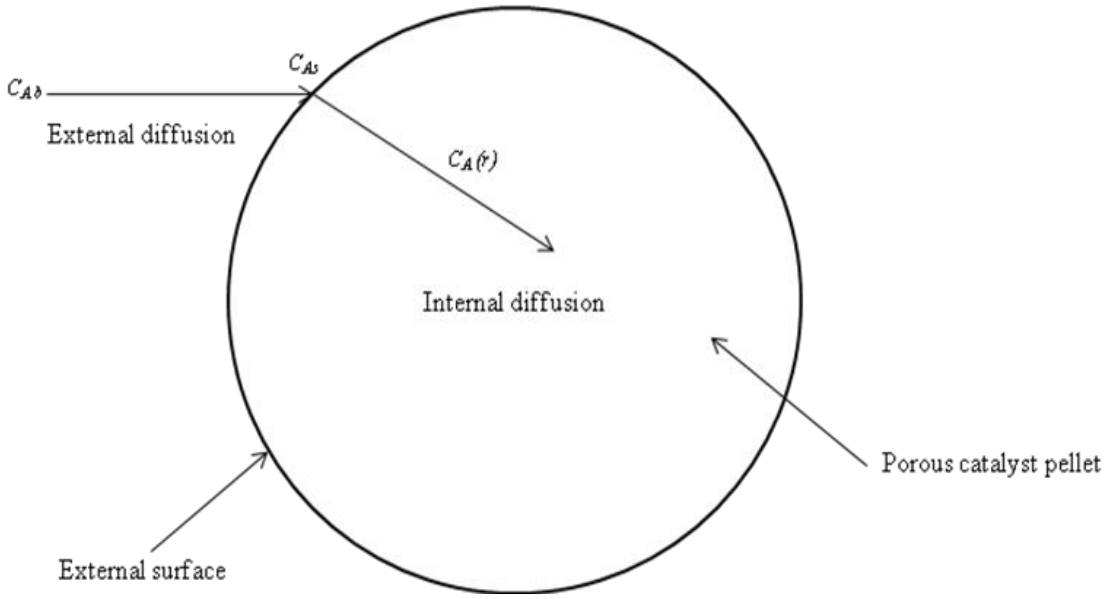

Figure 2-4: Mass Transfer and Reaction Steps for a Catalyst Pellet

In addition, in a practical DMFC, mass transport resistances within the catalyst layers (internal resistances) are normally considered negligible due to the fact that the catalyst layers are thin (5-25 μm) in comparison to the gas diffusion layers (100-300 μm) and the membrane (~200 μm). However, the external mass transport resistance (from the bulk to the surface) may be important. A one dimensional, steady-state, isothermal model of a DMFC that allows rapid prediction of polarization data and gives insight into mass transport phenomena occurring in the cell has been reported in the literature [67]. Concentration variations of CH_3OH across the membrane electrode assembly (MEA) region that is, anode backing layer (ABL), anode catalyst layer (ACL), and membrane were considered in the model. Figures 2-5 and 2-6 show a schematic diagram of the layers considered in the model and a typical polarization curve, respectively. Several assumptions were also made.

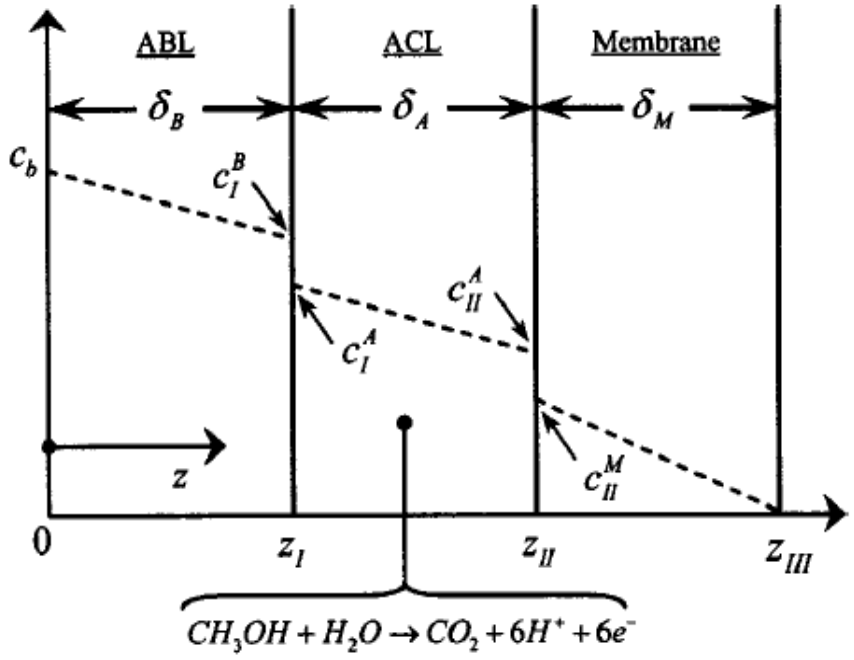

Figure 2-5: Schematic of Mass Transfer Layers in MEA

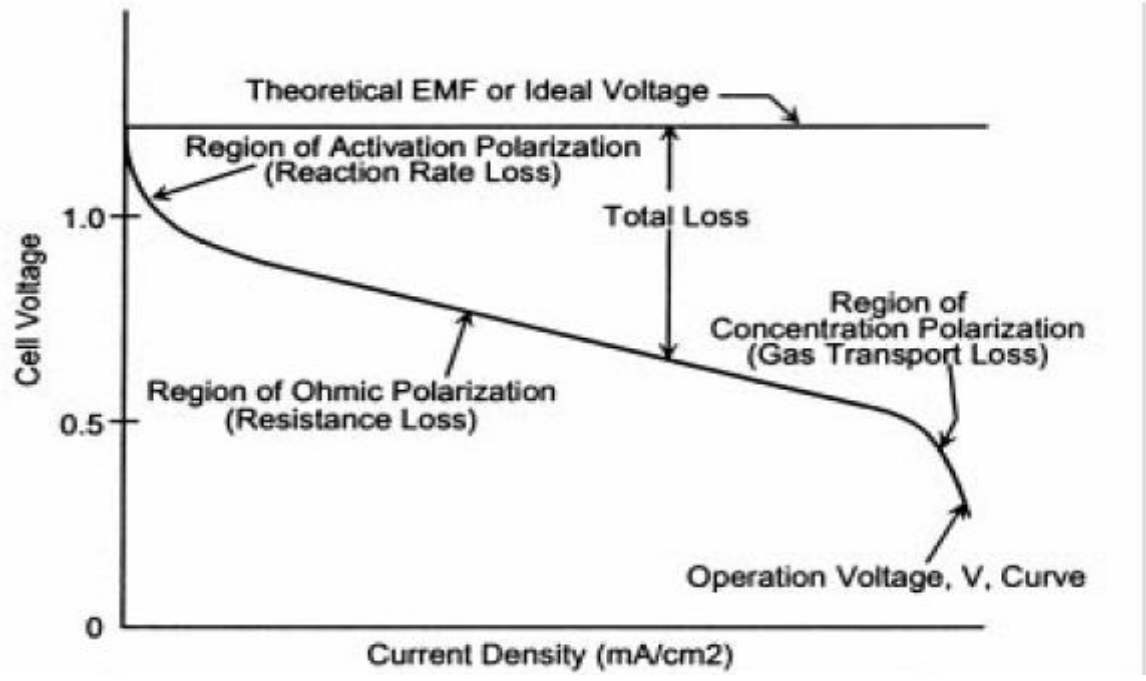

Figure 2-6: Typical Polarization Curve

The mass transport equations for the concentration profiles representing each of the three layers shown in Figure 5 are given below [67]:

- ABL

The governing equation for CH_3OH in the ABL:

$$\frac{d^2 c^B_{CH_3OH}}{dz^2} = 0 \tag{2.39}$$

The boundary conditions are given as:

$$At\ z = 0: \qquad c^B_{CH_3OH} = c_b \tag{2.40}$$

$$At\ z = z_I: \qquad c^B_{CH_3OH} = c^B_I = \frac{c^A_I}{K_I} \tag{2.41}$$

It is assumed that concentration at the flow-channel/ABL interface is given by the bulk concentration in the flow channel. The concentration at the ABL/ACL interface is given by assuming local equilibrium with a partition coefficient K_I.

- ACL

The governing equation for CH_3OH in the ACL:

$$D_A \frac{d^2 c^A_{CH_3OH}}{dz^2} = \frac{j}{6F} \tag{2.42}$$

where j is the volumetric current density (A/cm^3) given as [67]:

$$j = a I_{0,ref}^{CH_3OH} \frac{k C_{CH_3OH}^{CL}}{C_{CH_3OH}^{CL} + \lambda \exp\left(\frac{\alpha_a \eta_a F}{RT}\right)} \exp\left(\frac{\alpha_a \eta_a F}{RT}\right) \quad (2.43)$$

where a is the specific surface area of the anode (cm^{-1}), k & λ are constants, and $I_{0,ref}^{CH_3OH}$ is the exchange current density of methanol (A/cm^2).

The boundary conditions are:

$$At\ z = z_{\mathrm{I}}: \quad c_{CH_3OH}^{A} = c_{\mathrm{I}}^{A} \quad (2.44)$$

$$At\ z = z_{\mathrm{II}}: \quad c_{CH_3OH}^{A} = c_{\mathrm{II}}^{A} \quad (2.45)$$

- Membrane

The governing equation for the CH_3OH in the membrane is given as:

$$\frac{d^2 c_{CH_3OH}^{M}}{dz^2} = 0 \quad (2.46)$$

It is assumed that all the CH_3OH crossing the membrane reacts at the cathode creating a very low concentration at the membrane/cathode-layer interface. The concentration at the ACL/membrane interface is given by assuming local equilibrium with a partition coefficient K_{II}.

$$At\ z = z_{\mathrm{II}}: \quad c_{CH_3OH}^{M} = c_{\mathrm{II}}^{M} = \frac{c_{\mathrm{II}}^{A}}{K_{\mathrm{II}}} \quad (2.47)$$

$$At\ z = z_{\mathrm{III}}: \quad c_{CH_3OH}^{M} \approx 0 \quad (2.48)$$

The CH_3OH concentration at the interfaces (c_I & c_{II}) is expressed as [67]:

$$c_{\mathrm{I}}^{CL} = \frac{\delta_A D_M K_{II}\left(D_B c_b - \frac{I_{Cell}\,\delta_B}{12F}\right) + \delta_M D_A\left(D_B c_b - \left(1+6\xi_{CH_3OH}\right)\frac{I_{Cell}\,\delta_B}{6F}\right)}{D_B K_I\left(\delta_A D_M K_{II} + \delta_M D_A\right) + \delta_B D_A D_M K_{II}} \quad (2.49)$$

$$c_{\mathrm{II}}^{CL} = \frac{\delta_M\left(D_A D_B c_b - \delta_A D_B K_I\left(1+12\xi_{CH_3OH}\right)\frac{I_{Cell}}{2nF}\right) - \delta_B D_A\left(1+6\xi_{CH_3OH}\right)\frac{I_{Cell}}{6F}}{D_B K_I\left(\delta_A D_M K_{II} + \delta_M D_A\right) + \delta_B D_A D_M K_{II}} \quad (2.50)$$

where

δ_B, δ_A & δ_M are the anode backing layer, anode catalyst layer & membrane thickness (*cm*), D_B, D_A & D_M are the CH_3OH effective diffusivities in the anode backing layer, anode catalyst layer & the membrane (cm^2/s), K_I & K_{II} are the partition coefficients, c_b is the CH_3OH bulk concentration in the flow channel (mol/cm^3), I_{Cell} is the cell current density (A/cm^2) and ξ_{CH3OH} is the mole fraction of CH_3OH (mol/mol).

Equations (2.39) to (2.50) are solved and used together with the kinetic equations to determine the cell voltage [67].

2.6 Methanol Electro-oxidation Catalysts

Among the elements, Pt shows the highest activity for the electro-oxidation of CH_3OH in an acid environment. However, one of the limiting factors of this catalyst in contact with CH_3OH is CO generation, which adsorbs and blocks the Pt active sites. This has resulted in many studies on the CH_3OH electro oxidation in both acid and alkaline medium using different catalysts. Some of the catalysts developed for the CH_3OH electro-oxidation are described in the next sections.

2.6.1 Single Metal Catalysts

The element Pt is the most active catalyst for CH_3OH electro-oxidation. Many Pt catalysts either supported on Vulcan XC-72 or Carbon nanotubes have been studied for the CH_3OH electro-oxidation. However, it is well known that a carbon supported Pt catalyst is poisoned by the adsorbed CO-like intermediates, which limits the catalytic activity for the CH_3OH electro-oxidation [88]. It is generally accepted that the catalytic activity is strongly dependent on the shape, size and distribution of the Pt particles. Many methods, such as microemulsions, microwave irradiation, solid reaction method, organic colloid method, inorganic colloid method, chemical reduction, and impregnation method have been used to prepare carbon supported Pt catalysts. All of these preparation techniques are aimed at generating Pt particles on the nanoscale and with uniformity.

Pt/C catalysts were prepared using different preparation techniques, denoted as Pt/C (a) & Pt/C (b) and their performance compared [89 90]. The Pt/C (b) catalyst was prepared by chemical reduction (one of the simplest methods) of hexachloroplatinic acid (H_2PtCl_6) in glycol solution using formic acid as the reducing agent. It exhibited a high activity for CH_3OH and CO_{ads} electro-oxidation. Table 2-2 shows the description of the catalysts in terms of their specific electrochemical surface area and BET specific surface area [89]. The data in the Table show that the Pt/C(b) catalyst has the largest BET surface area and ESA, which are 192.34 $m^2\ g^{-1}$ and 84.16 $m^2\ g^{-1}$, respectively. The large ESA value of Pt/C (b) indicated that the Pt in the Pt/C (b) catalyst was well dispersed, which contribute to the high specific activity.

Table 2-2: The ESA and BET Specific Surface Area for Two Different Pt/C Catalysts

Samples	ESA ($m^2 g^{-1}$)	BET Surface Area ($m^2 g^{-1}$)
Pt/C (a)	32.93	184.37
Pt/C (b)	84.16	192.34

The SEM image shown in Figure 2-7 indicates that well dispersed Pt particles were obtained on the carbon support. The XRD patterns shown in Figure 2-8 show a small Pt particle size of 2.6 nm for the Pt/C (b) catalysts, which is in agreement with the results from the TEM image shown in Figure 2-9.

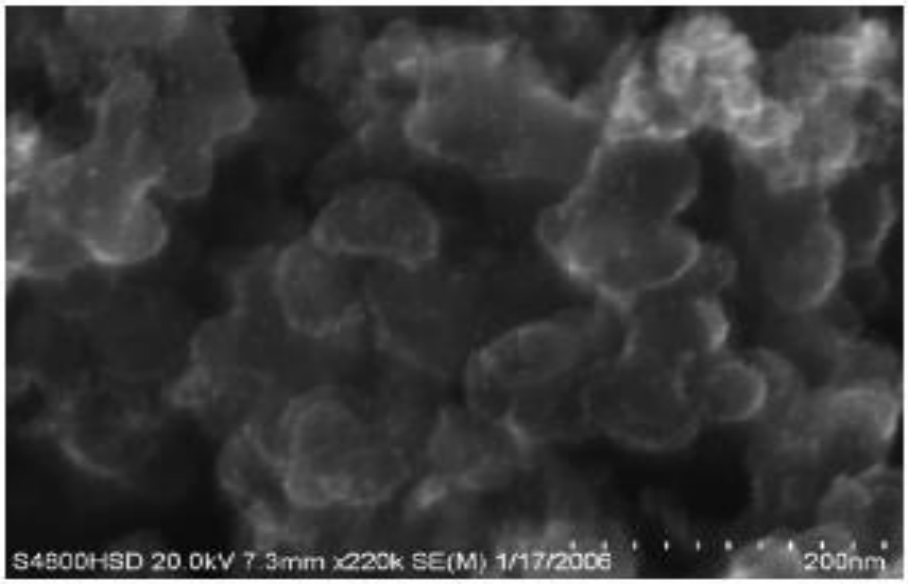

Figure 2-7: SEM Image of the Pt/C (b) Catalyst

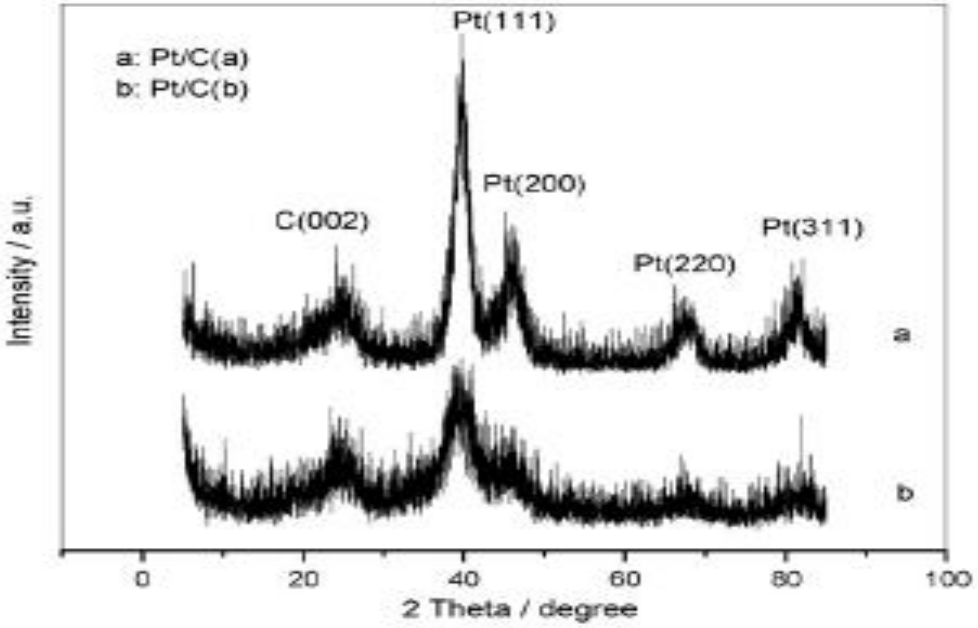

Figure 2-8: XRD Patterns of the Catalysts

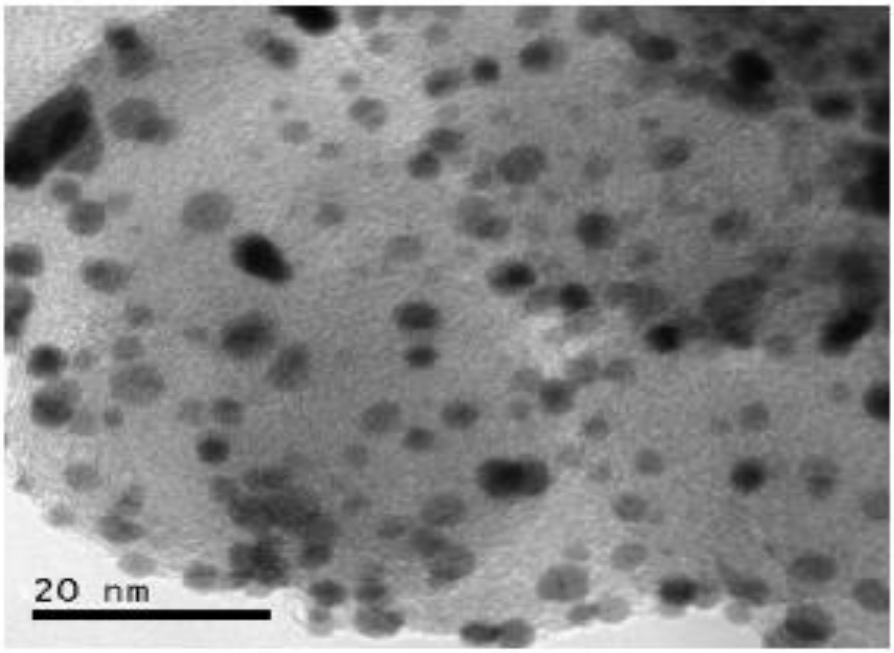

Figure 2-9: TEM Image of the Pt/C (b) Catalyst

Figure 2-10 shows the linear sweep curves of CO_{ads} for Pt/C (a) and Pt/C (b) electrodes in the 0.5M H_2SO_4 solution at 25 $^{\circ}$C. From the Figure, it can be observed that the peak current density of CO_{ads} oxidation for Pt/C (b) electrode is much greater than that of Pt/C (a) and the onset potential of CO_{ads} oxidation for Pt/C (b) occurs at about 0.5V—a slightly negative shift compared to that of the Pt/C (a). The peak potential of CO_{ads} oxidation on Pt/C (b) is 0.63V, about 40 mV—more positive than that on the Pt/C (a).

Figure 2-11 shows the chronoamperometry curves for the CH_3OH electro-oxidation on Pt/C (a), Pt/C (b) and commercial Pt/C (E-TEK) catalysts at 0.6V (versus Ag-AgCl) in the solution of 1.0 mol L^{-1} CH_3OH + 0.5 mol L^{-1} H_2SO_4 at 25 $^{\circ}$C for 12 h. An initial rapid decrease in the current density with time was observed for both catalysts, which was suggested to be due to the formation of CO_{ads} and other intermediate species during CH_3OH oxidation. After that, the current decreased slowly and achieved a pseudo-steady state; the decay can be attributed to the adsorbed anion SO_4^{2-} on the surface of the catalyst, which can restrict the CH_3OH oxidation reaction. The current density stabilized within 2 min for Pt/C (b) catalyst and about 80 min for Pt/C (a) after application of the set potential. In addition, the current density for the Pt/C (b) catalyst was over 23 $mAcm^{-2}$ higher than that for the Pt/C (a).

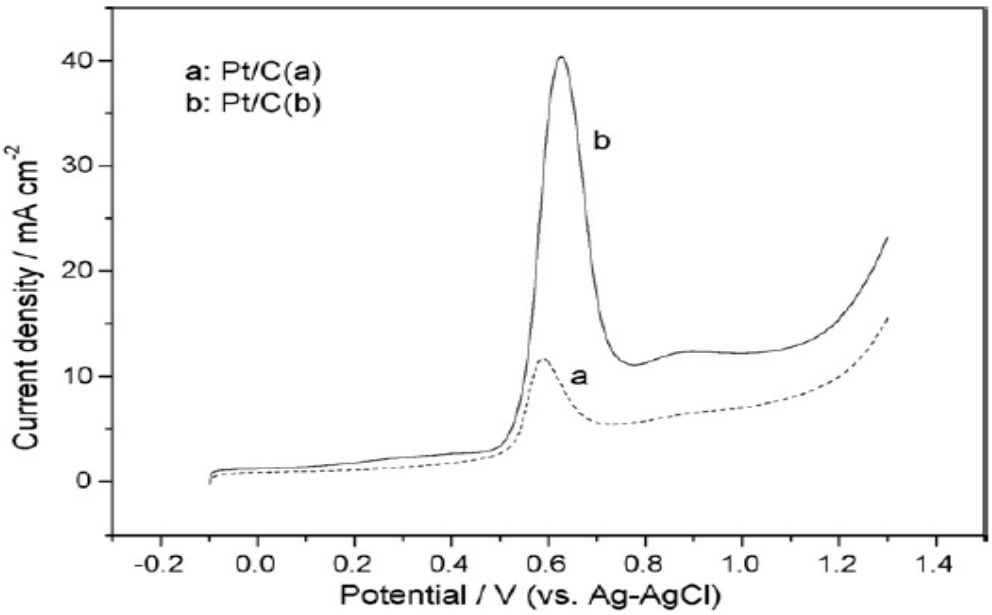

Figure 2-10: Linear Sweep Voltammograms of Different Pt/C Electrodes in 1M CH_3OH + 0.5M H_2SO_4 at 25 ^oC and 10 mV/s

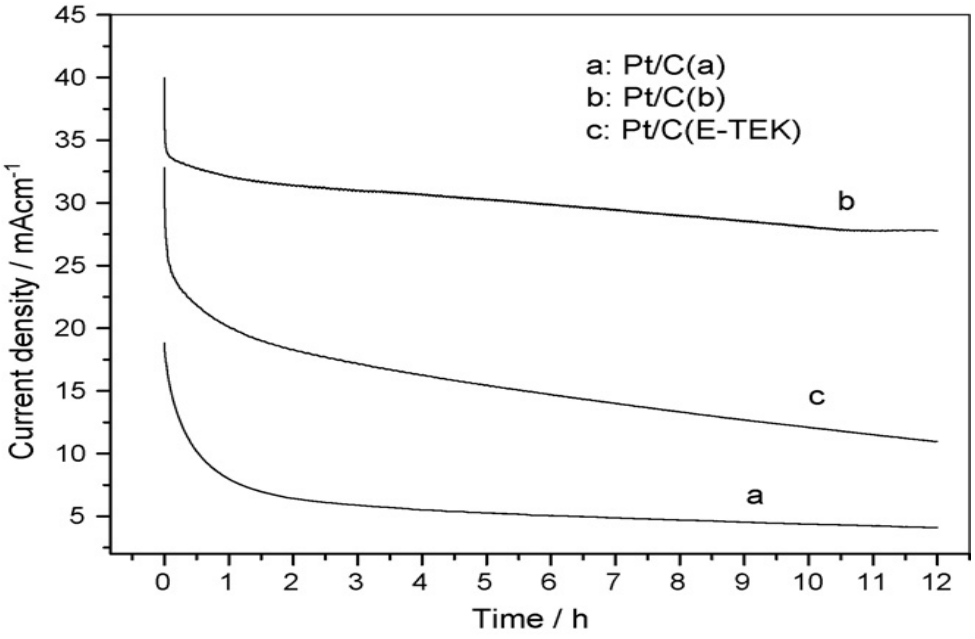

Figure 2-11: Chronoamperometric Curves for the Catalysts in 1M CH_3OH + 0.5M H_2SO_4 at 25 ^oC, 0.6V vs. Ag-AgCl

The electrochemical properties of Pt-based electrode catalyst are also significantly affected by the carbon support material. That is, the nature of carbon support materials is crucial in determining the electrochemical performance of a catalyst. The key properties of being a suitable support material for electro catalyst include good electron conductivity, high surface area, suitable morphology & microstructure, and low cost. Carbon black (Vulcan XC-72) has been the most widely used support material because of its reasonable balance among electron conductivity, surface area, and cost. Thus, improvement and optimization of an electro catalyst should include improvements both in the active metal (Pt) component and in the carbon support materials.

Due to their unique structure, high surface area, low electrical resistance and high stability in an acid environment , carbon nanotubes (CNTs) have been the main focus of many recent research efforts aimed at finding alternative carbon support materials [91 92]. The CNT materials are usually classified as single-walled (SWNTs) or multi-walled (MWNTs), which consist of a single and several graphite-layers in the wall of a tube, respectively. The lengths of the CNTs are normally in the micrometer range with diameters varying from 0.4 to 3 nm for SWNT and from 1.4 to 100 nm for MWNTs. A number of earlier investigations have demonstrated that Pt-based electro catalysts supported by properly pretreated MWNTs showed enhanced electro catalytic activity for both the CH_3OH and CO_{ads} oxidation [93 94]. Attempts of using SWNTs as the supporting carbon materials also generated encouraging results. Figure 2-12 shows the XRD patterns, pore size distribution and SEM images for SWNTs and MWNTs [92].

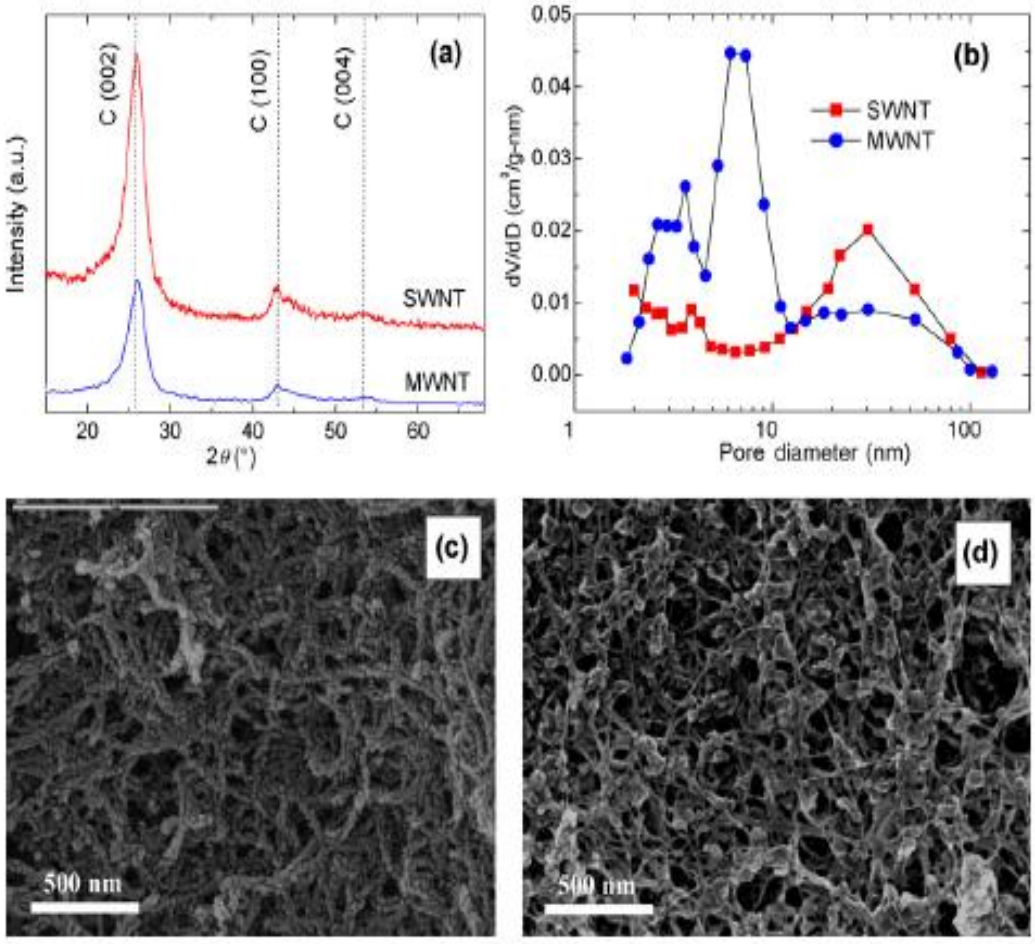

Figure 2-12: XRD Patterns (a) and Pore Size Distribution (b) for MWNT and SWNT: SEM Images of MWNT/Nafion (c) and SWNT/Nafion (d) Electrodes

It has been reported that Pt nanoparticles deposited on SWNTs showed a remarkably enhanced activity for the electro-oxidation of CH_3OH than those deposited on conventional Vulcan XC-72 carbon black [95]. In comparison with membrane-electrode-assembly (MEA) using Pt catalyst supported on commercial carbon black, MEA fabricated using SWNT supported Pt catalyst displayed significantly improved fuel cell performances for both H_2 and CH_3OH fuels.

TEM images for Pt-MWNT/Nafion and Pt-SWNT/Nafion having an identical loading of 100 μg-Pt cm^{-2} are shown in Figure 2-13(a) and (b), respectively [92]. Compared with the Pt-MWNT/Nafion, Pt particles in Pt-SWNT/Nafion seem to have closer contact with the network of entangled and branched bundles of SWNTs, and assumed shapes that are more close to highly exposed spheres. It is noteworthy that the Pt particles were anchored mainly at the boundaries of the SWNT bundles and Nafion binders, which would be highly favorable in the transport of electrons and protons during electrocatalysis. The beneficial morphology of Pt particles demonstrates again that the electrodeposition technique gives higher utilization and more uniform dispersion of Pt particles. Figure 2-14 shows the CV curves for CH_3OH electro oxidation on the Pt-MWNT/Nafion and Pt-SWNT/Nafion catalyst with a loading of 100 μg-Pt cm^{-2} [92].

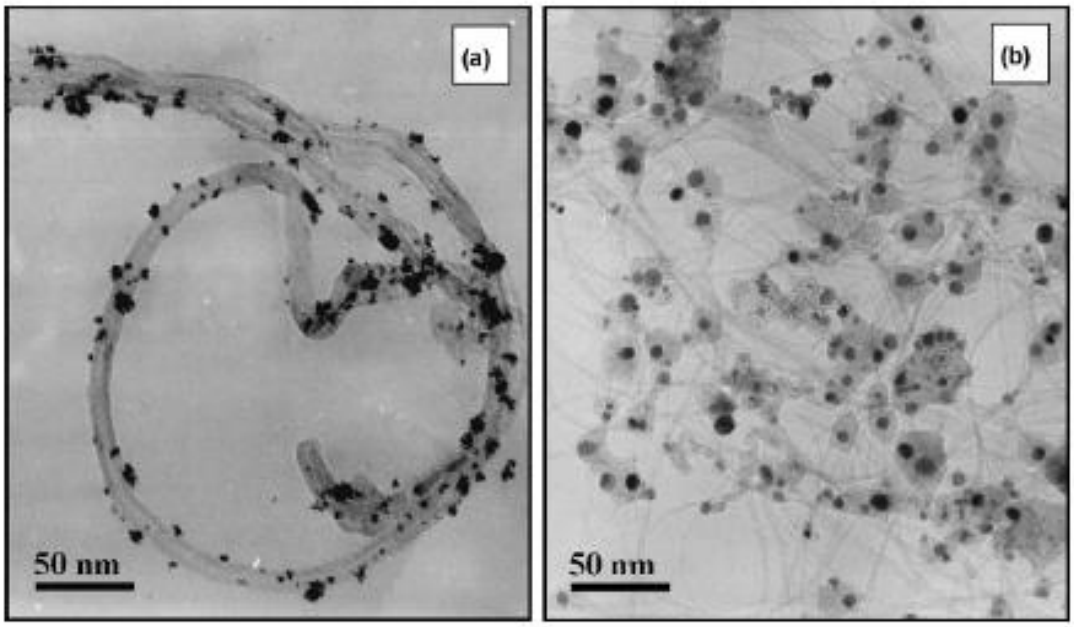

Figure 2-13: TEM Images of Pt-MWNT/Nafion (a) and Pt-SWNT/Nafion (b)

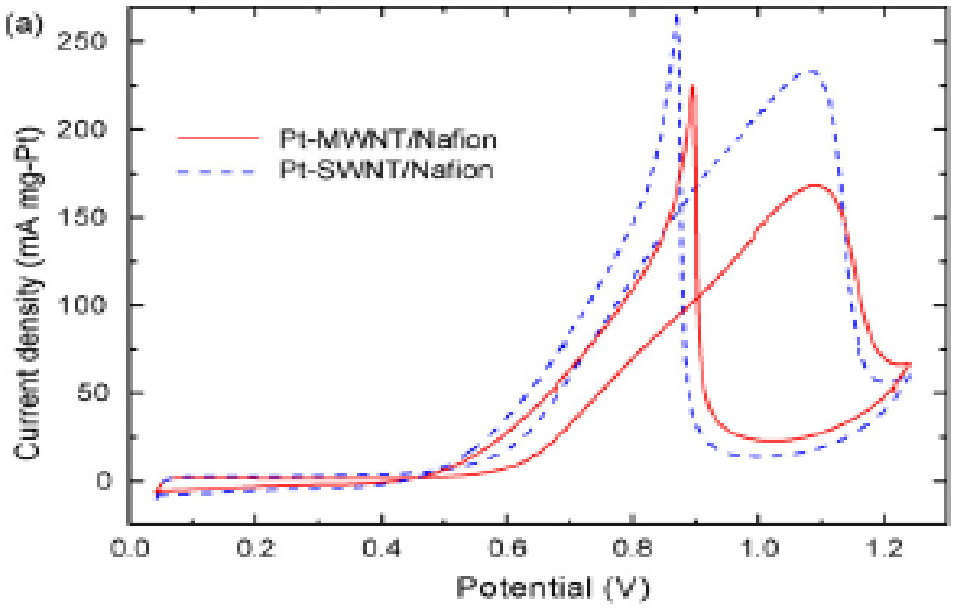

Figure 2-14: CVs for Methanol Electro-Oxidation Using Pt-MWNT/Nafion and Pt-SWNT/Nafion Catalysts in 0.5M CH_3OH + 0.5M H_2SO_4 at a Scan Rate of 10 mV/s

The enhanced activity of Pt catalyst supported by SWNT/Nafion electrode is evidenced by a slightly lower onset potential and significantly higher current density. The onset potential for Pt-SWNT/Nafion was 0.45V while that for the Pt-MWNT/Nafion was 0.50V [92]. Theoretically, the onset potential is related to the breaking of C–H bonds and subsequent removal of CO_{ads} intermediates by oxidation with OH_{ads} supplied by Pt–OH sites or other sources during the process CH_3OH adsorption and dissociation on Pt sites.

In addition, the Pt-SWNT/Nafion electrode exhibited an enhanced activity in oxidizing CO_{ads} in comparison with Pt-MWNT/Nafion for the CO stripping measurements. In a similar way, the oxidative removal of C1 intermediates easily occurs on Pt-SWNT/Nafion catalyst. Furthermore, stronger Pt-support interactions in the Pt-SWNT/Nafion catalyst would contribute to the promotion of C–H breaking and CO_{ads} tolerance. In addition, the significantly higher CH_3OH oxidation currents in both forward and subsequently reversed scans for Pt-SWNT/Nafion catalyst clearly demonstrate a higher mass specific activity of Pt metal in Pt-SWNT/Nafion catalyst, due to the higher utilization of Pt.

2.6.2 Bimetallic Catalysts

It is generally agreed that the poisoning of Pt surface by CO like species produced during CH_3OH electro-oxidation is the major reason for the low kinetics. To solve this problem, advanced electro-catalyst design relying on the bi-functional mechanism has been proposed. That is, a second component such as Ru or $RuO_2{\cdot}xH_2O$ is incorporated during the catalyst formulation to assist in the oxidation

of CO like species to CO_2 by dissociating water to create and absorb oxygen-containing species nearby the poisoned Pt sites. Among all the binary catalysts studied and reported in the open literature, Pt-Ru alloy is regarded as the most suitable for the CH_3OH and CO_{ads} electro-oxidation [34]. It has been reported that Ru easily removes CO_{ads} from Pt atoms and enhances the catalytic activity of CH_3OH electro-oxidation by a bifunctional mechanism or a ligand effect [96].

There are several methods to synthesize Pt-Ru nano-particles for fuel cell application, which include impregnation method, colloidal method, micro-emulsion method, chemical reduction method and microwave irradiation method. Among these methods, impregnation method is the most widely used because the process is simple. The method includes many variables, such as the use of different reducing agent and metal precursors, as well as different means of mixing the reducing agent and changing the pH, which affects the particle size, dispersion, morphology, surface composition, and degree of alloying.

However, performance of the Pt-Ru catalysts depends on maximized catalyst surface area, suitable Pt-Ru crystallite size and Pt-Ru alloy of atomic ratio close to 1:1. Three unsupported, highly dispersed Pt-Ru catalysts (having similar overall atomic ratios near 50 atom% Ru) designated as A-1, A-2, and B-1 have been studied and reported in the literature [97]. Table 2-3 shows the Physical properties and CH_3OH anodic oxidation activity for the three different samples of the unsupported Pt-Ru catalyst using similar amounts of loading of the catalyst (5 ± 0.3 mg cm^{-2} of geometric surface area). It can be observed that although the samples' bulk compositions are similar,

their CH_3OH oxidation activity at DMFC anode potential of 0.35 V and 80°C with 1 M CH_3OH feed at the anode differs greatly. That is, 450 mA cm^{-2}, 225 mA cm^{-2} and 30 mA cm^{-2} for catalysts A-1, B-1 and A-2 respectively. The difference in their performance is attributed to the variation in the surface area and metals crystallite size, which affect the dispersion.

Table 2-3: Physical Properties and Methanol Anodic Oxidation Activity for Three Samples of Unsupported Pt-Ru Catalysts

Catalyst	Pt-Ru atomic %	Crystallite size (nm)	BET area (m^2g^{-1})	i ($mAcm^{-2}$)
A-1	45/55	2	70	450
A-2	46/54	7	29	30
B-1	49/51	3	93	225

Figure 2-15 shows the results for both CO stripping (top) and anodic oxidation of CH_3OH (bottom) at 60 °C. The results show the influence of the population of metal alloy active sites on the catalyst CH_3OH electro-oxidation activity. The currents were normalized to the CO stripping charge (*q*CO). The top part shows that CO stripping activity is identical for catalysts A-1 and B-1 when normalized to *q*CO. Most importantly, the bottom part shows that CH_3OH oxidation current (in the relevant potential region) is also exactly the same for catalysts A-1 and B-1 once normalized to *q*CO. Catalyst A-2 is the odd sample out, showing lower anodic activity per *q*CO in both anodic processes, indicating the significance of the composition of the active surface sites [97].

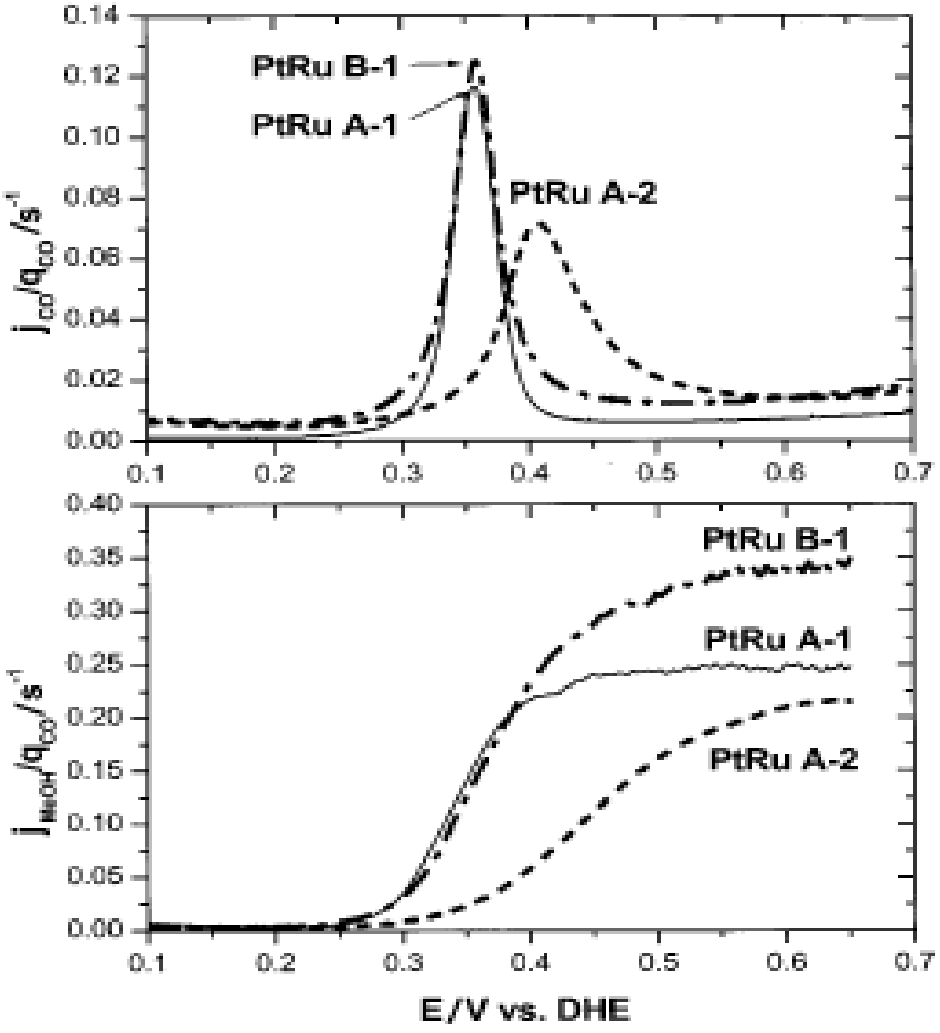

Figure 2-15: CO Stripping Voltammetry at 5 mV/s and Anodic Methanol Oxidation for the Three Unsupported Catalysts at 2 mV/s with 0.5M CH_3OH feed flowing at 1 ml/min

.

Pt-Ru/C catalysts have also been prepared using the impregnation method under different $NaBH_4$ (reducing agent) concentrations [98]. Carbon black, Vulcan-P (about 150 m^2 g^{-1} BET surface area) from the Cabot Corporation was suspended in deionized water and sonicated. The metal precursors, that is, H_2PtCl_6 and $RuCl_3$ were dissolved in deionized water and stirred. The two solutions were mixed together and stirred sufficiently. The amounts of metal precursors were adjusted that Pt and Ru had a molar ratio of 1:1 and the total metal content in the catalysts was 60 wt%. $NaBH_4$ solutions of different concentrations were prepared in which the molar ratio of $NaBH_4$ to Pt and Ru metals was 1, 2, 5, 15, 50 and 250. The mixed solutions of the carbon black and metal ions were poured into each of the $NaBH_4$ solutions rapidly. After 20 min the prepared catalysts were filtered and washed with boiling water. The catalysts were then dried in vacuum oven at 80 °C for 12 hrs.

The catalysts prepared using 1, 2, 5, 15, 50 and 250 times of the $NaBH_4$ molar content to the metal precursors were designated as ‘x1’, ‘x2’, ‘x5’, ‘x15’, ‘x50’ and ‘x250’, respectively. Table 2-4 shows the crystal and surface properties of the prepared catalysts. Unit cell performances for the direct methanol fuel cell were tested using the prepared catalysts as the anode catalyst. The prepared catalysts in various $NaHB_4$ concentrations showed not only different surface compositions but also differences in terms of the particle size and level of dispersion. Figure 2-16 shows the cyclic voltammograms of the prepared catalysts [98]. At the initial cycle of the cyclic voltammetry, x1 and x2 showed a large base current, a small hydrogen desorption charge and a low oxide reduction peak compared to other catalysts.

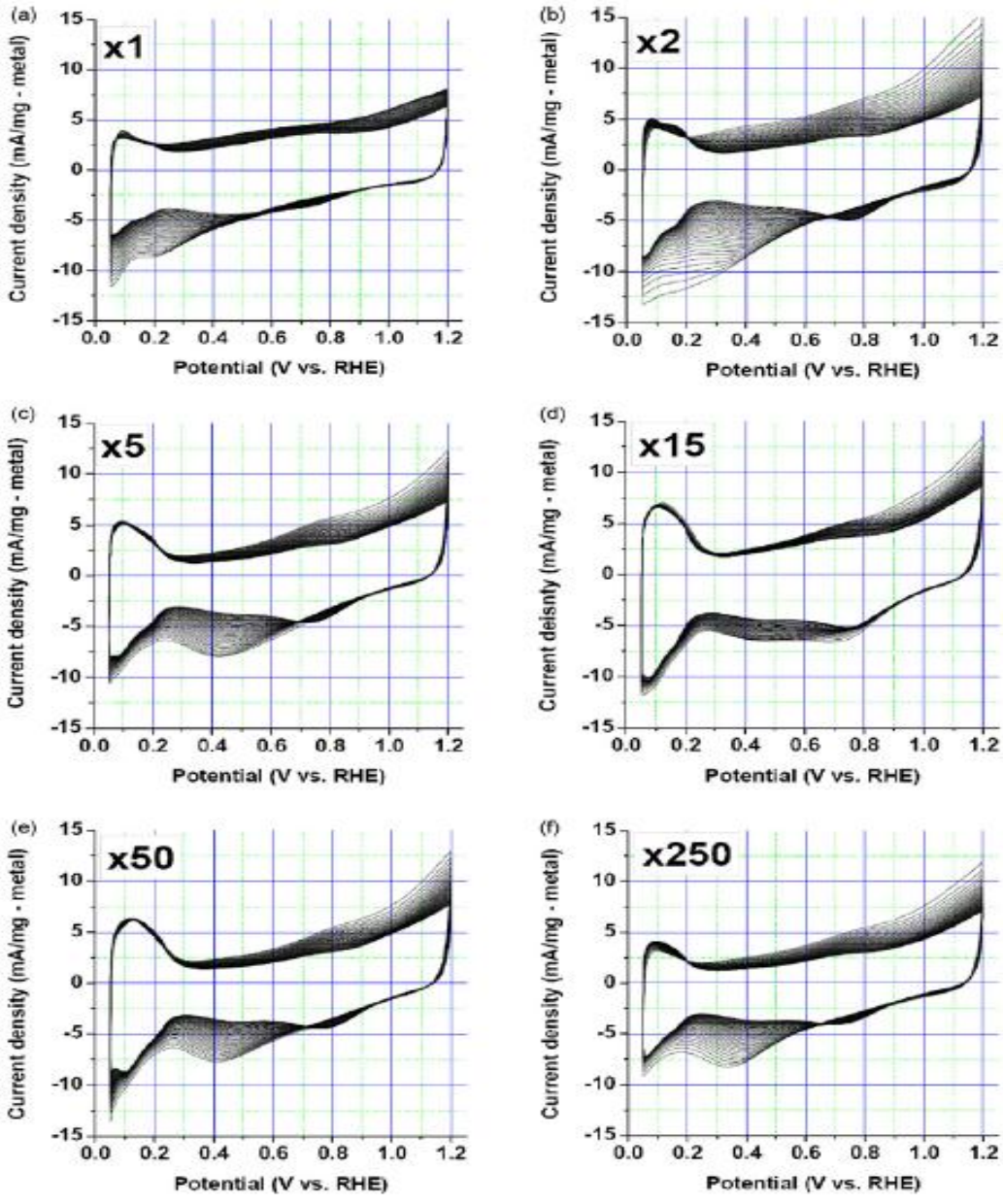

Figure 2-16: CVs of the Prepared PtRu/C Catalysts at a Scan Rate of 20 mV/s: (a) x1, (b) x2, (c) x5, (d) x15, (e) x50, (f) x250

From the results, x1 and x2 are presumed to have large Ru surface coverage. This Ru-rich surface originated from isolated Ru particles, which could not form a solid solution with Pt. In addition, it was predicted using the XRD results that x1 and x2 included a small amount of Ru in Pt-Ru solid solution.

Table 2-4: Crystal and Surface Properties of the Prepared Catalysts from XRD and XPS Results

Catalyst	Surface Composition Pt:Ru (%)	Lattice constant (Å)	Crystallite Size (nm
x1	12:88	3.88	3.6
x2	25:75	3.89	4.1
x5	52:48	3.863	2.4
x15	59:41	3.83	2.0
x50	59:41	3.874	2.0
x250	63:37	3.883	2.2
Commercial PtRu/C	46:54	-	-

The cyclic voltammetry curves of x5, x50 and x250 were similar to that of commercial PtRu/C. On the other hand, the shape of the curve of x15 did not change when compared with other prepared catalysts, implying that x15 formed a stable Pt-Ru solid solution. It included a large amount of Ru in the Pt-Ru solid solution in the XRD result. Therefore, it had a stable phase with a high degree of alloying. In conclusion, it was found that the ratio of $NaBH_4$ to the metals at 5 and 15 are the optimum for the CH_3OH electro-oxidation [98].

The catalytic activity of Pt-Ru is still currently below the level required for commercial acceptance. There are several common strategies to raise the performance of electro catalysts in fuel cell reactions such as the use of different preparation methods, new carbon supports and the addition of a third or even a fourth alloying metal as promoter. A more efficient carbon-supported Pt-Ru catalyst for the electro-oxidation of CH_3OH at room temperature has been reported [99]. It was prepared using a simple reversal of the order of mixing in the catalyst preparation. That is, adding the metal precursor salts to carbon slurry of $NaBH_4$ instead of adding $NaBH_4$ to carbon slurry of the metal precursor salts (PtRu-1/C), as is more commonly done.

Two Pt-Ru catalysts on Vulcan XC-72 carbon were prepared. PtRu-1/C was the "control sample" obtained by reducing $PtCl_6^{2-}$ and Ru^{3+} precursors in a XC-72 carbon suspension using the dropwise addition of $NaBH_4$ at room temperature with stirring. The starting molar ratio of Pt: Ru was kept at 1:1. Stirring was continued overnight before the solid phase was recovered by filtration, washed copiously with water, and dried in vacuum at room temperature overnight. For the second sample (PtRu-2/C), 120 ml de-ionized water containing a calculated amount of Vulcan XC-72 carbon was sonicated for 30 min in an ultrasonic bath to form carbon slurry. Under vigorous stirring at room temperature, 100 mg of $NaBH_4$ in 5ml water was immediately added, followed by a mixture of 1ml 50mM H_2PtCl_6 and 1ml 50mM $RuCl_3$ in one go. The rest of the preparative procedures were the same as those used in the preparation of PtRu-1/C. The CO stripping voltammograms of the catalysts are shown in Figure 2-17. The highest anodic potential in the scan was limited to 0.8V to prevent possible Ru dissolution.

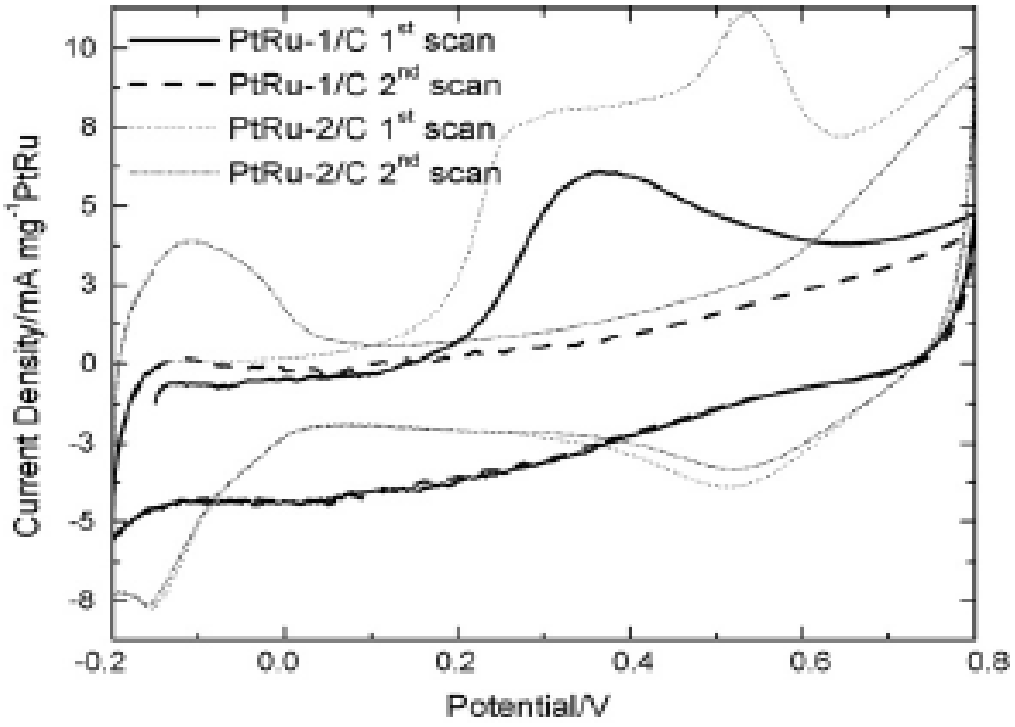

Figure 2-17: CO Stripping CVs for the Catalysts at a Scan Rate of 20 mV/s

CO oxidation went to completion in the first scan without any trace of CO in the second scan. However, the CV curves for the second scan were quite different for the two catalysts. That is, the voltammogram for the PtRu-1/C was typical of a Pt-Ru alloy catalyst with non-descript hydrogen adsorption/desorption region because the potential region overlaps with that of Ru oxidation. On the other hand, the voltammogram for the PtRu-2/C showed a well defined hydrogen adsorption/desorption region, a Pt oxide reduction peak in the reverse scan (at 0.53 V), and double layer formation characteristic of monometallic Pt [99]. The onset potentials for CO oxidation were 0.16V for the PtRu-1/C and 0.10V for the PtRu-2/C catalysts, respectively. The negative shifts in the onset of CO oxidation (0.10V versus 0.16 V) and stripping potential (0.26Vversus 0.36 V) indicate that PtRu-2/C could be a more CO tolerant catalyst in practice.

The different behaviours were mainly attributed to the variation in the preparation method. In the preparation of PtRu-2/C, when the precursors ($PtCl_6^{2-}$ and Ru^{3+}) were added to the carbon slurry containing an excess of $NaBH_4$, some Pt was selectively reduced without alloying with Ru because the Ru precursor could have been rendered less reducible via partial hydrolysis to hydrous oxides under the prevailing alkaline condition. This has led to the possibility of PtRu-2/C being a mixture of Pt, Pt-Ru, and hydrous Ru oxides in the end. On the contrary, PtRu-1/C was prepared according to standard techniques where $NaBH_4$ is the limiting reactant in the reduction of Pt and Ru precursors most of the times. There was no prevailing condition to divert Ru from being reduced synchronously with Pt and a homogenous Pt-Ru alloy was formed.

Figure 2-18 compares the chronoamperometry curves for the PtRu-1/C and PtRu-2/C catalysts at 0.3V. The potential was stepped to 0.3V from the open-circuit potential without prior electrochemical conditioning. With the potential biased at 0.3V, CH_3OH was continuously oxidized on the catalyst surface and tenacious reaction intermediates such as CO_{ads} would begin to accumulate if the kinetics of their removal could not keep pace with that of the CH_3OH oxidation. A more gradual decay of current density with time is therefore an indication of improved CO tolerance.

The Figure shows that the oxidation current density decreased to 34% of its initial value after 30 min for PtRu-2/C whereas the corresponding decline for PtRu-1/C was 50% of its initial value. The inset in the Figure also shows a sharper initial decrease of current density for PtRu-1/C, indicating faster accumulation of CO_{ads} and less facile CO_{ads} removal in this case. In conclusion, the increase in catalytic activity and CO tolerance of the PtRu-2/C catalyst was found to correlate well with the presence of multiple active phases in it although the exact composition of the phases could not be determined. This, along with similar findings on monometallic Pt catalysts shows the effectiveness of the reversal technique over the conventional method [99]. The reversal technique aim for smaller particle size and a higher state of metal dispersion on the carbon support.

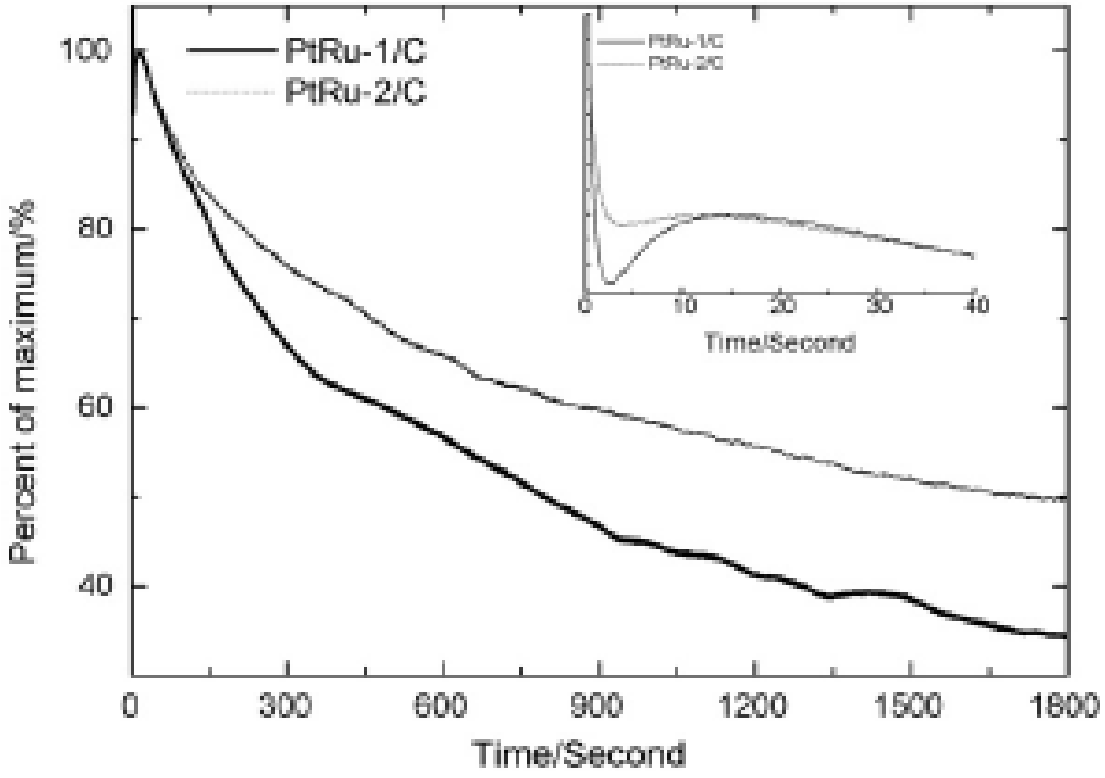

Figure 2-18: Chronoamperometry Curves of the Catalysts at 0.3V in 1M CH_3OH + 0.5M H_2SO_4 at Room Temperature

The performance of Pt-Ru catalysts is also influenced by the type of metal precursors used. Pt-Ru catalysts are usually prepared by chemical reduction with H_2PtCl_6 and $RuCl_3$ as the precursors for the Pt and Ru respectively. The Pt-Ru metal and carbon support may be eroded by the residual chloride ions from the precursors, thus its performance decays evidently. The Pt-Ru/C alloy catalysts can be prepared by using precursors without Cl^- ions, such as $Na_6Pt\ (SO_3)_4$ and $Na_6Ru\ (SO_3)_4$, which improves the performance to a great extent. $Pt\ (NH_3)_2(NO_2)_2$ compounds can also be used as a precursor for the Pt-based catalysts. However, the $Pt\ (NH_3)_2(NO_2)_2$ compounds may form two solutions—acidic and alkaline, respectively.

The acidic and alkaline solutions influence the Pt-Ru/C catalyst performance differently [100]. It was found that the performance of the Pt-Ru/C catalyst prepared from the acidic $Pt\ (NH_3)_2(NO_2)_2$ solution as the Pt precursor for CH_3OH electro-oxidation is better than that of the catalyst from the alkaline solution. This was due to the acidic environment of the precursor ink with the acidic $Pt\ (NH_3)_2(NO_2)_2$ and the acidic Ru compound as precursors, and the forming of a homogeneous dispersion of Pt-Ru metal particles with relatively small sizes on the carbon support.

The effect of Ru seems to be very consistent throughout the various preparation methods. Although Pt–Ru or $Pt–RuO_2{\cdot}xH_2O$ is among the preferred anode catalyst for CH_3OH oxidation, it is desirable to replace Ru using inexpensive metal or metal oxide in order to develop commercially affordable DMFCs. Work has been done on Pt–Sn, Pt–Mo, Pt–Ce, Pt–Ni and $Pt\text{-}TiO_2$ systems. The effects of tin as a secondary element on the oxidation of CH_3OH can be changed, depending on the preparation

method. Tin addition has resulted in both an improvement and deterioration of the catalytic activity. Catalytic activity of Pt, Pt-Ru and Pt-Sn with Ru or Sn electrodeposited on Pt surface in the oxidation of CO and CH_3OH has been investigated [101]. It was found that the Pt-Sn electrode showed higher activity only for short period of time while Pt-Ru showed relatively high and stable activity for longer period of time.

TiO_2 is known for its high catalytic activity and stability in acidic or alkaline solutions and has been widely studied for its special photoelectric properties. In addition, it has been reported that Pt or Pt-Ru catalysts supported on TiO_2 exhibited excellent catalytic activity for CH_3OH electro-oxidation because of the synergetic interaction between Pt and TiO_2 [102]. The effect of heat treatment on the performance of the TiO_2-Pt/CNT catalysts for the CH_3OH and CO electro-oxidation has also been reported [103]. TiO_2-Pt/CNT catalysts before and after heat treatment at 500 $^{\circ}$C for 2 hrs were denoted as TiO_2-Pt/CNT (B) and TiO_2-Pt/CNT (A), respectively. The prepared TiO_2-Pt/CNT catalysts have 1:2 molar ratios of TiO_2 and Pt. The result indicated that a proper amount of hydrous TiO_2 is very favorable for enhancing the catalytic activity of TiO_2-Pt/CNTs toward CH_3OH oxidation. The result is very important in understanding the mechanism of TiO_2 or other metal oxide promoting Pt for CH_3OH (or alcohol) oxidation in direct methanol (or alcohol) fuel cell. Table 2-5 shows the specific activity for CH_3OH oxidation and specific surface area of the prepared catalysts [103].

Table 2-5: Specific Activity for Methanol Electro-Oxidation and Specific Surface Area of TiO_2-Pt/CNTs (B), TiO_2-Pt/CNTs (A) and Pt/CNTs

Catalyst	*EAS* (cm^2mg^{-1} Pt)	I_s ($mAcm^{-2}$ Pt)
TiO_2-Pt/CNT (B)	511	1.11
TiO_2-Pt/CNT (A)	463	0.96
Pt/CNTs	515	0.77

Figure 2-19 shows the TEM images of the TiO_2-Pt/CNT (B), TiO_2-Pt/CNT (A) and Pt/CNT catalysts [103]. It can be observed that fine Pt nanoparticles dispersed uniformly on the CNTs in the three images. The particle size of Pt on TiO_2-Pt/CNT (B) and Pt/CNT was estimated to be 3–4 nm with narrow particle size distribution, whereas some aggregation and growth of Pt particle on TiO_2-Pt/CNT (A) catalysts were observed. In addition, the hollow structure of CNTs (as reported in numerous publications) was not clearly visible in TiO_2-Pt/CNT (B) and TiO_2-Pt/CNT (A) catalysts indicating the TiO_2 coating on Pt/CNTs. The CV curve for CH_3OH electro-oxidation on TiO_2-Pt/CNT (B), TiO_2-Pt/CNT (A) and Pt/CNT catalysts is shown in Figure 2-20 [103].

The Figure shows significant differences in peak current density and onset potential between the catalysts containing TiO_2 and those of pure Pt were observed illustrating the beneficial role of the TiO_2 for the CH_3OH electro-oxidation. Comparison of the CV curves for the TiO_2-containing catalysts reveals that the peak current density for TiO_2-Pt/CNT (B) catalysts (565 $mAmg^{-1}$ Pt) was much higher than that for TiO_2-

Pt/CNTs (A) (443 $mAmg^{-1}$ Pt) and the onset potential was found at even lower potential (0.360 V) than that for TiO_2-Pt/CNT (A) catalysts (0.449 V).

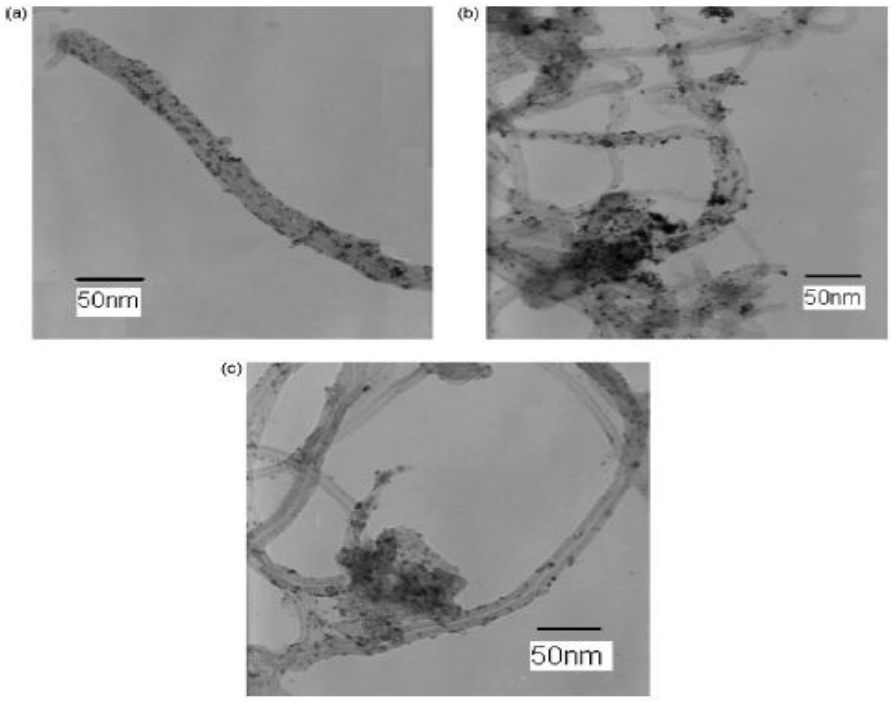

Figure 2-19: TEM Images of TiO_2-Pt/CNTs: (a) TiO_2-Pt/CNTs (B); (b) TiO_2-Pt/CNTs (A); (c) Pt/CNTs

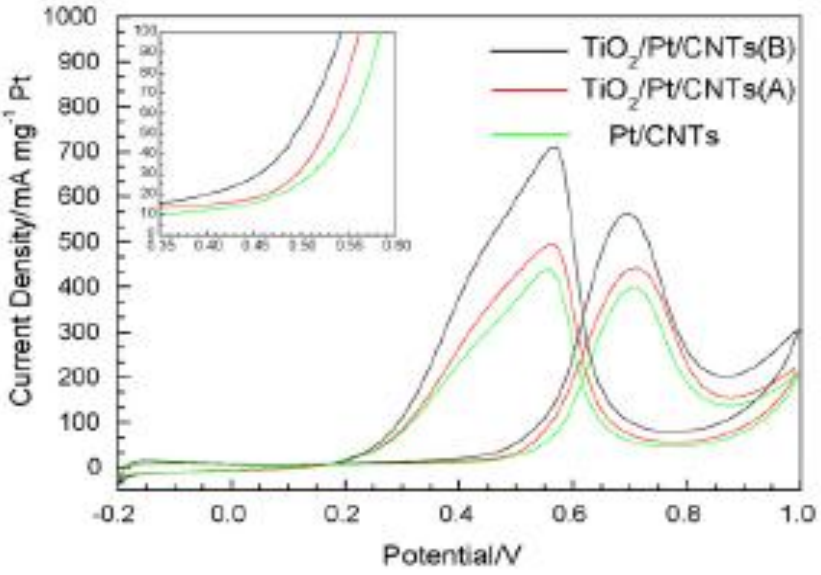

Figure 2-20: CVs for Methanol Electro-Oxidation for TiO_2-Pt/CNTs (B), TiO_2-Pt/CNTs (A) and Pt/CNTs Electrodes in 1M CH_3OH + 1M $HClO_4$ at a Scan Rate of 50 mV/s

In order to further investigate the influence of heat treatment on the activity of the catalysts, TiO_2-Pt/CNT (A) catalysts with the same TiO_2 to Pt and CNTs ratio were tested at the same conditions. In addition, experiment on CNT-supported Pt catalysts with the same Pt to CNTs ratio was also carried out for comparison. The mass activity (*Im*), which is defined as the ratio of current obtained from the forward CV scans to the mass (*mg*) of Pt in the electrode was used to evaluate the activity of the catalysts. The results showed that the catalytic activity of TiO_2-Pt/CNT catalysts for CH_3OH electro-oxidation was decreased after heat treatment though it was higher than that of Pt/CNT catalysts. This can be confirmed further from the potentiostatic polarization curves of CH_3OH electro-oxidation.

Still in an effort to replace or reduce the novel metals content so as to reduce the cost of the CH_3OH electro-oxidation catalysts, Pt– CeO_2/CB anodes which consisted of CeO_2 particles with different surface areas were synthesized and studied for the CH_3OH electro-oxidation [104 105]. In order to enhance the conversion of CO_{ads} to CO_2 on the Pt anode, the influence of particle size of CeO_2 particles in Pt–CeO_2/CB anode on the onset potential for CH_3OH electro-oxidation reaction was examined. It was found that the anode performance on Pt–CeO_2/CB is improved by an enhancement of surface area of CeO_2 particles (i.e. enhancement of surface activity of CeO_2 particles). As a consequence, the anode performance on Pt–CeO_2/CB was better than that on commercially available Pt–Ru/carbon anode or Pt–SnO_2/CB anode.

2.6.3 Ternary Catalysts

Several ternary catalyst systems have been studied for CH_3OH electro-oxidation. From theoretical screening results, it has been reported that alloying Pt-Ru with Fe, Co, Rh, Ir and Ni could provide higher activity than the Pt-Ru catalyst [22]. Pt-Ru-Ir /C catalyst was prepared using a microwave-irradiated polyol plus an annealing synthesis strategy [23]. The synthesis was carried out with the aid of a domestic microwave oven (LG WD700, 700W, 2450 MHz). Vulcan XC-72R carbon black (Cabot Corp., BET surface area of 250 m^2/g) was used as the support. The catalyst has 40 wt% metal content and the Pt: Ru: Ir atomic ratio is 1:1:1.

For the synthesis, 200 mg of Vulcan XC-72R carbon black was added in 120 ml of ethylene glycol and stirred vigorously to obtain slurry. Then solutions of 2.48 ml of 0.1517 M hexachloroplatinic acid in ethylene glycol, 10.27 ml of 0.0366 M ruthenium (III) chloride in ethylene glycol, and 1.5 ml of 0.1821 M chloroiridic acid in ethylene glycol were mixed and subsequently added to the slurry. The suspension was stirred for 30 min and ultrasonicated for another 30 min, followed by the addition of a 2.5 M ethylene glycol solution of sodium hydroxide to increase the pH to >10. The suspension was exposed to microwave irradiation in a 90 s on–10 s off–60 s on heating strategy, and then cooled to room temperature. Hydrochloric acid (3 M) was added to lower the pH to <1, to induce sedimentation of the as-synthesized Pt-Ru-Ir nanocomposite. The product was recovered using centrifuge and washing with ethanol for several times and dried in a vacuum oven at 80 °C for 8 hrs. The dry powder was then reductively annealed under flowing nitrogen (5% H_2/N_2, 500 °C, 4 hrs). The catalyst thus obtained was denoted as DICP PtRuIr/C.

For comparison, Vulcan XC-72R-supported PtRu nanocomposite with 40 wt% metal and a Pt:Ru atomic ratio of 1:1 and Vulcan XC-72R-supported Ir catalyst with 40 wt% metal were also prepared in the same way and were denoted as DICP PtRu/C and DICP Ir/C, respectively. Table 2-6 shows the metal contents in the prepared and 'control' catalysts [23].

Table 2-6: Metal Content in DICP PtRuIr/C, DICP PtRu/C and DICP Ir/C Catalysts

Catalyst	Metal Nominal Content[a] (%)			Metal Nominal Content[b] (%)		
	Pt	Ru	Ir	Pt	Ru	Ir
DICP PtRuIr/C	15.98	8.28	15.75	13.54	5.13	14.24
DICP PtRu/C	26.3	13.7	-	24.02	10.41	-
DICP Ir/C	-	-	40	-	-	37.4

[a] As calculated from metal content of 40 wt% and atomic ratio of 1:1:1 for Pt-Ru-Ir or 1:1 for Pt-Ru
[b] As determined from ICP-AES analysis

Figure 2-21a shows the CO stripping voltammograms of the DICP PtRuIr/C, DICP PtRu/C, and E-TEK PtRu/C catalysts in 1.0 M CH_3OH + 0.5 M H_2SO_4 at 25 $^{\circ}$C after full adsorption of CO and subsequent purging of the solution with high-purity N_2 [23]. The Figure also shows the second sweeping voltammograms. However, due to the different microstructures and macrostructures of various electrocatalysts related to the different compositions and the synthesis routes, the current in the cyclic voltammetry measurements is usually normalized by the metal loadings (viz., mA/mg metal) to compare the catalytic activity of the different electrocatalysts. Therefore, all

of the currents in the CO stripping voltammetry measurements were normalized per milligram of total metal [23].

It can be observed from the Figure that CO_{ads} has been oxidized completely in a single scan and no CO oxidation is monitored during the second scan for all the three catalysts. The peak potential for CO_{ads} electro-oxidation on DICP PtRuIr/C, E-TEK PtRu/C and DICP PtRu/C are 0.25, 0.31, and 0.45 V versus SCE, respectively, which indicates that addition of Ir in the Pt-Ru system leads to an enhanced activity for the electro-oxidation of the CO_{ads} (even higher than that for the commercial PtRu/C catalyst) [23]. Figure 2-21b shows the voltammetry behavior of DICP PtRuIr/C and DICP PtRu/C catalysts at low potential region, showing that the DICP PtRuIr/C catalyst exhibits a hydrogen oxidation peak in the hydride region (−0.192→−0.158 V vs. SCE) compared with DICP PtRu/C. This is the result of hydrogen electro-oxidation via transient holes in the CO_{ads} layer on metal active sites of DICP PtRuIr/C, implying the different surface structures of the two catalysts.

In conclusion, it was found that the Pt-Ru-Ir/C catalyst displayed a greatly enhanced activity for the CO_{ads} electro-oxidation higher than that observed on commercial Pt-Ru/C catalyst (E-TEK). The superior performance of the Pt-Ru-Ir/C catalyst was suggested to be as a result of the iridium additives, particularly IrO_2. An excellent electro catalytic activity of the carbon-supported Pt-Ru-Ir nanocomposite for the hydrogen oxidation reaction in the presence of CO was also observed.

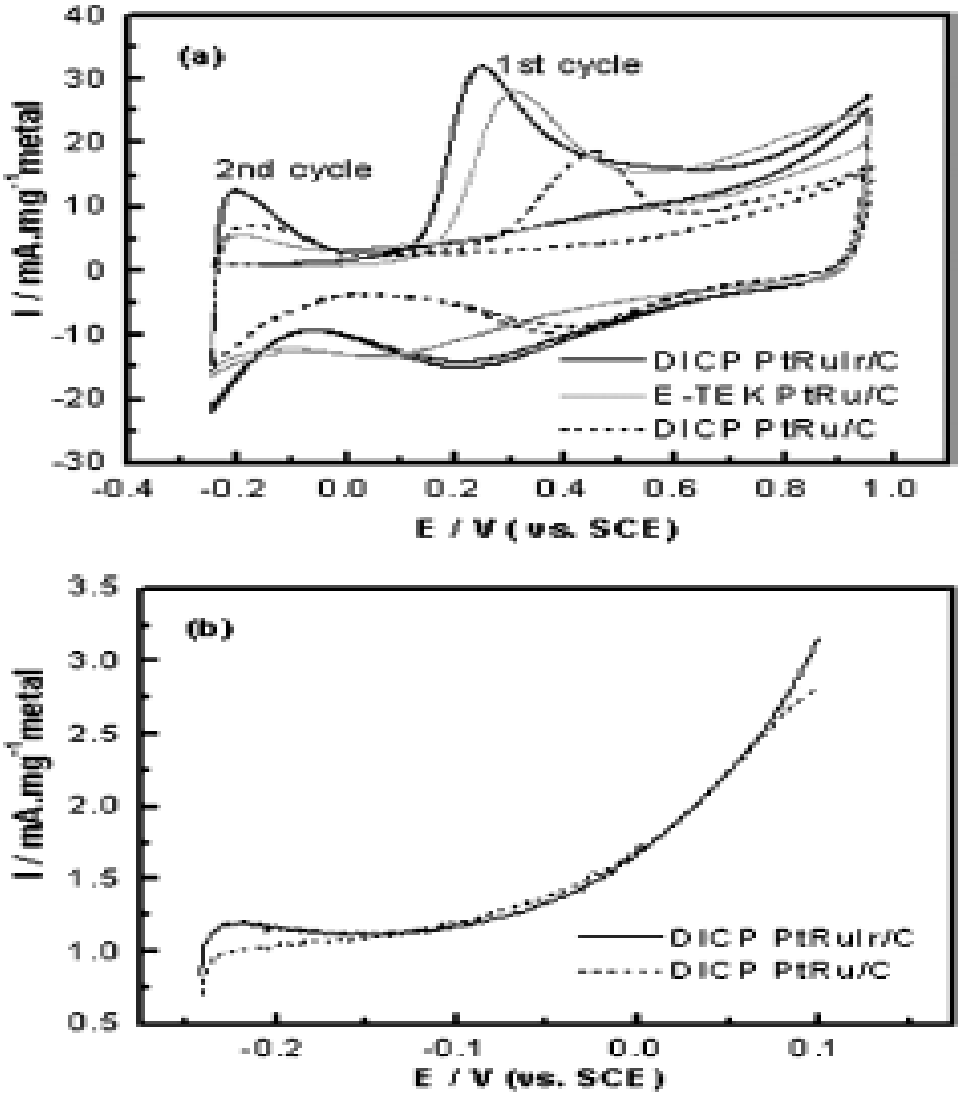

Figure 2-21: (a) CO-Stripping Voltammograms of DICP PtRuIr/C, DICP PtRu/C and E-TEK PtRu/C Catalysts in 0.5M H_2SO_4 at 25 ^oC. (b) Voltammetry Behaviour of DICP PtRuIr/C and DICP PtRu/C Catalysts at Low Potential Region at 20 mV/s

Pt–Ru–Ir nanoparticle catalysts on carbon black have also been prepared using a vapor deposition method [53]. The electro catalytic activity of the particles towards CH_3OH electro-oxidation was investigated by cyclic voltammetry, chronoamperometry and adsorbed CO-stripping voltammetry. It was found that the Pt–Ru–Ir nanoparticle catalyst has outstanding activity for the CH_3OH electro-oxidation when compared to a Pt–Ru catalyst. CO-stripping voltammetry showed that the superior activity comes partly from a larger active surface area and partly from a higher catalyst resistance to CO poisoning due, in turn, to the presence of Ir.

The addition of Ir appears to accelerate the activation of the C–H bonds during the CH_3OH electro-oxidation. The effect of composition in the Pt-Ru-Ir catalyst system (Pt_x (Ru–Ir)$_{1-x}$/C) on the CH_3OH electro-oxidation in acid media has also been studied [106]. It was found that $Pt_{0.25}$ (Ru–Ir) $_{0.75}$/C composition has the highest catalytic activity towards the CH_3OH electro-oxidation in acid media. Furthermore, the increase in the load of Ru and Ir apparently improves the catalytic performance of those composites catalysts. Thus, ternary catalysts containing large concentrations of Ru and Ir are very promising to be used in anodes of direct methanol fuel cells.

$Pt_{45}Ru_{45}Fe_{10}$/C, $Pt_{45}Ru_{45}Co_{10}$/C and $Pt_{45}Ru_{45}Ni_{10}$/C catalysts have also been prepared and investigated for CH_3OH electro-oxidation [24]. Conventional $NaBH_4$ reduction method was used for the synthesis of the catalysts. Carbon support (Vulcan XC72R) was dispersed in mixture of de-ionized water and isopropyl alcohol, and then metal precursors were dissolved. H_2PtCl_6, $RuCl_3$ were used for Pt and Ru precursors, respectively and for the Fe, Co, and Ni metals, (NH_4) Fe $(SO_4)_2$, $CoCl_3$ and $NiCl_2.6H_2O$ were used as precursors, respectively. Loading of metals was adjusted to

60 wt%. The mixture was heated to 80 °C and kept for 1 hr with stirring. $NaBH_4$ solution (0.2 M) was added to the mixture solution for reduction and the mixture was kept for 3 hrs with stirring. The catalyst and solvent mixture was filtered and washed with hot water. The final catalyst slurry was dried at 100 °C overnight. Table 2-7 shows the electrochemical properties of the prepared catalysts [24].

Table 2-7: Electrochemical Properties of $Pt_{45}Ru_{45}Fe_{10}/C$, $Pt_{45}Ru_{45}Co_{10}/C$, $Pt_{45}Ru_{45}Ni_{10}/C$ and PtRu/C Catalysts

Catalyst	EAS ($m^2/g\ cat$)	On-set voltage for CO electro-oxidation	Current density at 0.5 V (mA/cm^2)	Mass activity ($A/g\ cat.$)	Specific activity (mA/m^2)
$Pt_{45}Ru_{45}Fe_{10}/C$	23	0.46	3.0	2.6	110
$Pt_{45}Ru_{45}Co_{10}/C$	18	0.48	2.5	2.2	120
$Pt_{45}Ru_{45}Ni_{10}/C$	17	0.48	2.9	2.5	150
PtRu/C (E-TEK)	26	0.49	2.6	2.3	88

Figure 2-22 shows CH_3OH electro-oxidation activity measurement results while current densities of the catalysts at 0.5 V are listed in the Table [24]. The current densities were converted into mass and specific activities. In the case of mass activity, the PtRuFe/C and PtRuNi/C catalysts showed mass activities of 2.6 and 2.5 A/g cat., respectively, which are higher than that of the commercial PtRu/C; 2.3 A/ g cat. However, PtRuCo/C catalyst exhibited slightly lower mass activity of 2.2 A/g cat. than that of the commercial PtRu/C.

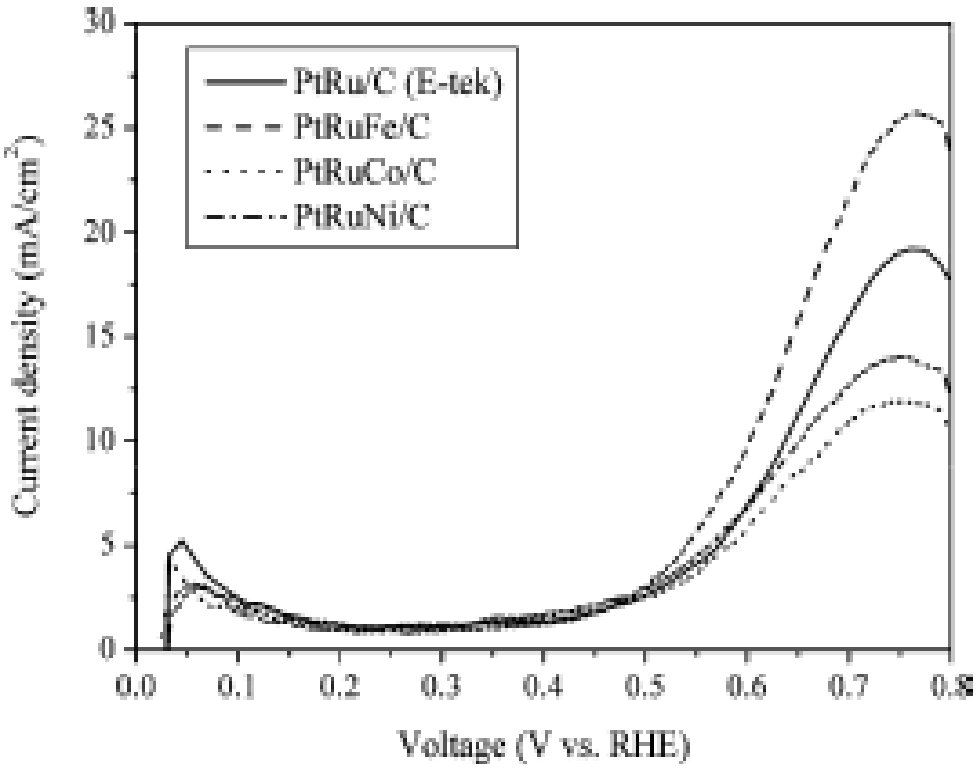

Figure 2-22: Methanol Electro-Oxidation Activity Measurement Results in 1M CH_3OH + 1M H_2SO_4 at a Scan Rate of 15 mV/s

To remove surface area dependence on the activity of the catalysts, specific activity was calculated by dividing mass activity by EAS obtained from the CO stripping. Specific activities of the catalysts were 110, 120, and 150 mA/m^2 for the PtRuFe/C, PtRuCo/C, and PtRuNi/C catalysts, respectively. When compared to the specific activity of 88 mA/m^2 for the commercial PtRu/C catalyst, increase of specific activities by addition of a third metal is clear. In particular, the specific activity of $Pt_{45}Ru_{45}Ni_{10}$/C catalyst was 70% higher than that of the commercial PtRu/C catalyst.

In conclusion, for the CH_3OH electro-oxidation activity measurement, the $Pt_{45}Ru_{45}Fe_{10}$/C catalyst exhibited the highest mass of 2.6 A/g cat. and the $Pt_{45}Ru_{45}Ni_{10}$/C catalyst showed highest specific activity of $150mA/m^2$, which was 70% higher than that of commercial Pt-Ru/C catalyst. It has also been reported in another study that addition of Ni and Pb into Pt catalysts can significantly improve the electrode performance for CH_3OH electro-oxidation [107]. It was found that the activity of Pt–Ni–Pb/C for CH_3OH electro-oxidation in acid medium is much higher than that of commercial Pt/C (E-TEK) catalyst. The performance with an atomic ratio of 5:4:1 was the best.

2.7 Membrane Electrode Assembly (MEA) Fabrication

A typical MEA consists of two gas diffusion layers (GDLs), two dispersed catalyst layers (CLs), and a membrane. Each component of an MEA performs unique roles. The GDLs have many roles to play. As the name implies, the main purpose of the GDL is to distribute the reactants from the flow channels uniformly along the active surface of the catalyst layer. In addition, the GDL ensures proper transport of product

water, electrons, and heat of reaction. The GDL assists in water management by allowing an appropriate amount of water to reach, and be held at the membrane for hydration on the anode side, especially if the anode gas stream is dry. While on the cathode side, the water that forms must be easily repelled from the catalyst surface to prevent flooding. If water collects near, or in, the catalyst layer, a large fraction of the catalyst will not be utilized. Typically, PTFE (Teflon) is applied through various methods to the GDL in order to manage the water. However, Teflon is not an electric conductor and reduces the porosity, which hinders the transport of reactant gases. Thus, appropriate amount of Teflon should be used carefully. The GDL is also the electronic conductor between the current collecting bipolar plates and the catalyst layers. Thus, a thin GDL with a high conductivity is desired for electrical efficiency. Furthermore, the GDL serves as the base substrate for the deposition of the catalyst layer or forms a protective layer over the very thin layer of the catalyst.

The GDLs are usually constructed from porous carbon paper, or carbon cloth, with a thickness in the range of 100 – 300μm. The in-plane and the through-plane resistivities of the commercial GDLs are in the range of 25-100 mΩ cm^2 and 6 -20 mΩ cm^2 respectively [108]. The in-plane and the through-plane resistances depend on the microstructure of the GDL. The in-plane resistance affects the reaction uniformity while the through-plane resistance dictates the cell resistance. To improve mass transport, GDLs can be made more porous at the cost of increased electrical resistance. Critical parameters that affect the performance of the GDLs include the PTFE content, thickness, pore size distribution, and microstructure. Carbon aerogels have also been used to form the porous substrate in the GDLs fabrication [109]. The

300μm thick layers featured micron-thin fine-structured layers on both sides of the gas diffusion layer. The fine layers are incorporated to decrease contact resistances between the electrode and the membrane, as well as the current collecting bipolar plate. The highest level of electrical conductivity of 28 S/cm has been reported in an 80% porous sample [109]. The largest pore sizes were in the range of several microns. However, when the gas diffusion layers were used in a test cell, it showed a power density of only 1/6 that of a typical PEM fuel. This was attributed to poor catalyst layer preparation and not the gas diffusion layer.

The catalyst layer (active layer) is in direct contact with the gas diffusion layer and the membrane. The half-cell reaction in a low temperature PEM-based fuel cell takes place within the catalyst layer in both the anode and cathode sides. The catalyst layer is either applied to the membrane or to the GDL. In either case, the objective is to place the catalyst particles, platinum or platinum alloys within close proximity of the membrane. Two widely employed catalyst layer preparation techniques (in terms of the binding material that is used) are the PTFE-bound and thin-film. Emerging techniques include those featuring catalyst layers formed with electrodeposition and vacuum deposition (sputtering). In general, catalyst layer preparation techniques are differentiated by the structure and fabrication of the catalyst layer. Before the development of the thin-film catalyst layer preparation technique, PTFE-bound catalyst layers were the convention [110]. The first generation of PEMFC used PTFE-bound Pt black electrocatalysts that exhibited excellent long-term performance but at an exorbitant cost. In the PTFE-bound technique, the catalyst particles are bound by a hydrophobic PTFE structure commonly cast to the GDL. This method was able to

reduce the platinum loading of earlier PEMFC by a factor of 10; from 4 - 0.4 mg/cm^2 [111]. In order to provide ionic transport to the catalyst site, the PTFE-bound catalyst layers are typically impregnated with Nafion by brushing or spraying. However, platinum utilization in PTFE-bound catalyst layers remains very low; approximately 20%. Nevertheless, researchers have continued to work on developing new strategies for Nafion impregnation. Some of the original low-platinum loading PEMFC featuring PTFE-bound catalyst layers were fabricated at the Los Alamos National Laboratory in the United States (one of the leading laboratories in the world engage in PEM-based fuel cells research and development).

The thin-film technique was used to achieve catalyst loadings of less than 0.35 mg/cm^2 for the PEMFC [112]. In this method the hydrophobic PTFE traditionally employed to bind the catalyst layer is replaced with hydrophilic perfluorosulfonate ionomer (Nafion). Thus, the binding material in the catalyst layer is composed of the same material as the membrane. Even though PTFE features effective binding qualities and imparts beneficial hydrophobicity in the gas diffusion layers, there is no particular benefit to its presence in the catalyst layer. The resilient binding of PTFE catalyst layer is traded for the enhanced protonic conductivity of a Nafion-bound thin-film catalyst layer. Thin-film catalyst layers have been found to operate at almost twice the power density of PTFE-bound catalyst layers. This correlates with an active area increase from 22 to 45.4% when a Nafion-impregnated and PTFE-bound catalyst layer is replaced with a thin-film catalyst layer [113]. Moreover, thin-film MEA manufacturing techniques are more established and applicable to stack fabrication. However, an active area of 45% indicated that there was significant potential for

improvement. Recent published research results have reported far better active area increase.

The catalyst layer thicknesses vary between 10 and 20 μm depending on catalyst loading levels. Pt is recognized to be the best catalyst for both the anode and the cathode. However, the choice of the anode catalyst and loading levels also depends on the fuel type and source. One of the most important factors to consider when choosing an anode catalyst is tolerance to carbon monoxide (CO). The CO is a known poison to many catalyst systems. When operating on pure hydrogen relatively little Pt is needed since the hydrogen electro-oxidation reaction is facile and the resulting overpotential is small. The issue of CO is of concern in the PEMFC when hydrogen if formed from methanol by steam reforming or when the fuel is a reformate (i.e., a mixture of H_2, CO_2, N_2, and impurities such as CO). For the DMFC where methanol is directly used, the CO is produced as intermediate specie during the methanol electro-oxidation reaction. There are two ways to minimize the effect of the CO poisoning: good purification during the fuel reforming or catalyst alloying such as PtRu, PtNi, PtCo, PtRuIr, PtRuFe etc.

The membrane, which serves as an electrolyte in the low temperature PEM-based fuel cells functions as a separator between the anode and cathode, which prevents the mixing of fuel flowing from the anode to the cathode. It is expected to allow only protons to pass from the anode to the cathode. Thus, it should be highly proton conductive, impermeable to fuels and oxidants, electrically resistive and chemically stable. Under long-term operation the membrane should have sufficient mechanical

and chemical stability to avoid rapid degradation. Another function is that it can serve as a substrate where the anode and cathode catalysts are applied during the MEA design. The most commonly used membrane in MEA design for the low-temperature PEM-based fuel cells is Nafion® membrane from DuPont. Other single polymer-based membranes and composite membranes have also been investigated. In general, materials that are used to make membranes include: perfluorousulfonic acid (PFSA), partially-fluorinated and non-fluorinated polymers.

Among the membrane materials, PFSA is the most commonly used. It consists of three (3) regions: a polytetrafluoroethylene-like backbone (PTFE, generally known as the Dupont's Teflon™), side chains of $–O\text{-}CF_2\text{-}O\text{-}CF\text{-}O\text{-}CF_2\text{-}CF_2\text{-}$ that connect the molecular backbone to the third region, which is the ion clusters consisting of sulfonic acid ions. When the membrane is hydrated, the hydrogen ions in the third region become mobile by bonding to the water molecules and moving between the sulfonic acid sites. There are two (2) advantages of PFSA membranes in PEMFC: they are relatively strong and stable in both oxidative and reductive environments due to their PTFE backbone (durability of 60,000 hrs has been achieved), a well-humidified PFSA membrane can achieve a high proton conductivity of up to 0.2 S/cm under PEMFC operating conditions. This gives a very low cell resistance of 0.5 $m\Omega\ cm^2$ for a 100 μm thick membrane with a voltage loss of only 50mV at $1A/cm^2$ [114].

The MEA design, particularly the component design of the cathode diffusion layer, the membrane and the anode diffusion layer, plays an important role on the water transport through the membrane. The reduction in water crossover by enhancing the

back convection of water from the cathode to the anode has been achieved by building up a hydraulic liquid pressure in the cathode with a highly hydrophobic cathode diffusion layer. Different methods to achieve highly hydrophobic cathode diffusion layers include the use of a thick and hydrophobic backing layer, adding a thin layer of highly hydrophobic microporous layer onto cathode backing layer and making the backing layer with finer and more hydrophobic pores by penetrating mixture of carbon powders and PTFE into the backing layer.

For the MEA assembly, the membrane and GDLs are normally manufactured prior to the assembly whereas the catalyst layers are usually prepared and applied during the assembly. A membrane is produced via a variety of polymerization processes. The processing steps include many chemical processes and a number of heating and drying steps. As mentioned earlier, either carbon cloth or carbon paper can be used as a GDL. Carbon cloth is fabricated in four stages: carbonaceous fiber production (made from mesophase pitch spun by melt spinning, centrifugal spinning, blow spinning, etc), fiber oxidation, cloth formation by weaving or knitting and graphitization. Carbon paper is also fabricated using four steps: pre-pregging (continuous strands are aligned with spools and a surface treatment is followed by a resin bath and formation of a layered structure), molding, carbonization and graphitization. Finally, the carbon cloth or paper is wet-proofed, typically using PTFE. A PTFE suspension is applied to both sides of the carbon cloth or paper substrate. Application of the PTFE helps to flatten any roughness of the carbon cloth or paper and improves the gas and water transport properties.

There are two modes of MEA Assembly as shown in Figure 2-23 [115]:

- Application of catalyst layers to a GDL followed by membrane addition. Five different methods can be used to prepare the catalyst/GDL assembly: spreading, spraying, powder deposition, ionomer impregnation, and electro-deposition.
- Application of catalyst layers to a membrane followed by GDL addition, also known as catalyst coated membrane (CCM) technique. Six different methods can be used to prepare the catalyst/membrane assembly: Impregnation reduction, evaporative deposition, dry spraying, catalyst decaling, and painting.

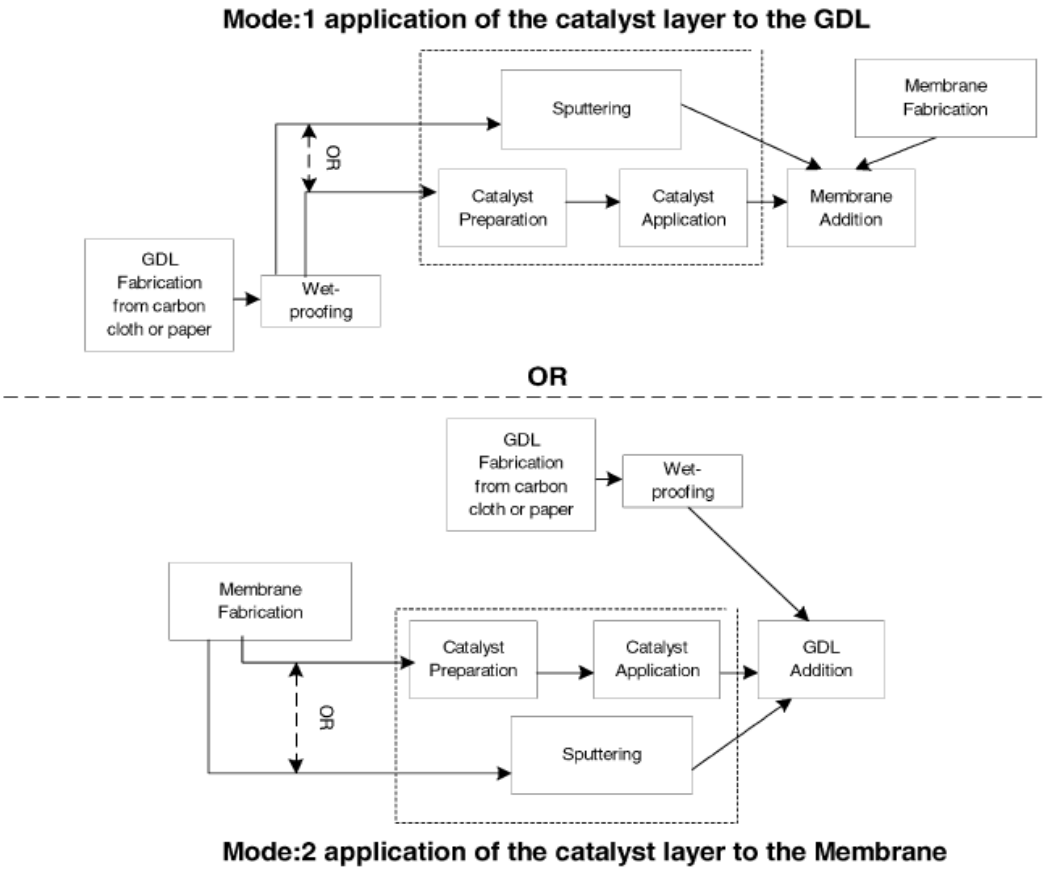

Figure 2-23: Methods of MEA Assembly

CHAPTER 3

3. METHODOLOGY

From the literature review carried out, it has been found that the chemical nature of the active components, the support materials & their surface condition, and the preparation techniques are the essential parameters in the development of CH_3OH electro-oxidation catalysts. Thus, using knowledge acquired from the relevant literature regarding achievements on the CH_3OH electro-oxidation catalysts development, experiments for this PhD Dissertation were designed and conducted in order to achieve the stated objectives. Details of the procedures followed are given in the next sections.

3.1 Functionalization of Multiwalled Carbon Nanotubes

Commercial MWCNTs were functionalized using the conventional acid treatment as shown in Figure 3-1. The raw MWCNTs were immersed in a solution of 30 % HNO_3 and 98% H_2SO_4 and refluxed at 80 °C for 10 hrs. The suspension was filtered, washed copiously with distilled water and dried at 100 °C overnight to obtain the functionalized MWCNTs powder.

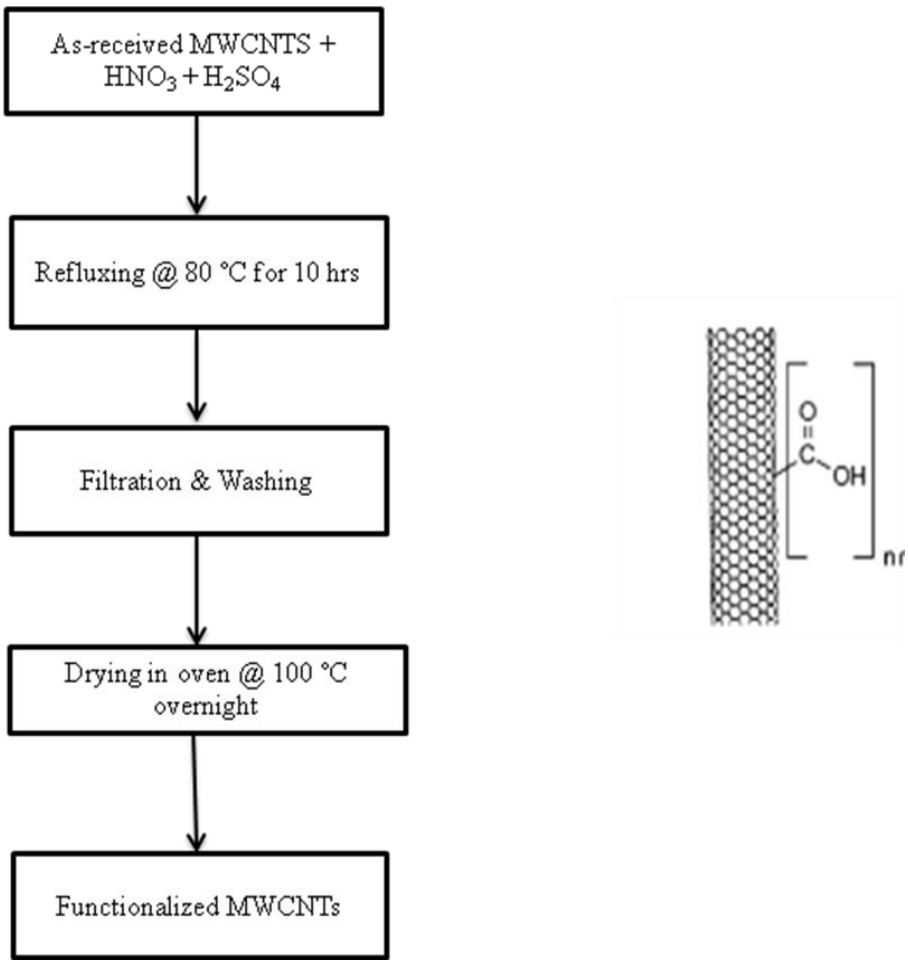

Figure 3-1: Carbon Nanotubes Functionalization Procedure

3.2 SBA15 and Mesoporous Carbon Nitride (MCN) Synthesis

SBA15 was synthesized by dispersing 4g of Pluronic P123 (a tri-block copolymer - $EO_{20}PO_{70}EO_{20}$ – (poly (ethylene glycol) - block-poly (propylene glycol) - block poly (ethylene glycol))), which serves as the structure-directing agent into 30 ml of distilled water and stirred for 4 hrs at room temperature. Then, 120 ml of 2M hydrochloric acid (HCl) solution was added and stirred at 40 °C for 2 hrs. This was followed by addition of 9 g tetraethylorthosilicate and continuous stirring for 24 hrs at 40 °C. Three batches were prepared and the resulting gels were kept for aging for 48 hrs at 100 °C, 130 °C, and 150 °C after which they were filtered, washed with high purity 18 MQμ distilled water several times and dried in an oven at 100 °C overnight. Finally, the powder was calcined in a muffle furnace in O_2 at 540 °C for 24 hrs to obtain the SBA15. The SBA15 samples were labeled SBA15-100 °C, SBA15-130 °C, and SBA15- 150 °C and were used as templates for the preparation of mesoporous carbon nitride, labeled as MCN-100, MCN-130 and MCN-150. For the preparation of the MCN materials, 1g of SBA15 sample was added to a mixture of 2.7 g ethylene diamine (EDA) and 6g carbon tetrachloride (CTC). The resulting mixture was refluxed and stirred at 90 °C for 6 hrs. Then, the obtained dark-brown solid mixture was placed in a drying oven for 12 hrs and grounded into powder. The fine powder was placed in a furnace at 600 °C for 5 hrs under nitrogen flow to obtain a black fine powder. The MCN samples were recovered after dissolution of the silica framework in 5 wt% hydrofluoric acid (HF), by filtration and washing several times with ethanol and dried at 100 °C for 6 hrs. Schematic procedures for SBA15 and mesoporous carbon nitride (MCN) syntheses are shown in Figures 3-2 and 3-3 respectively.

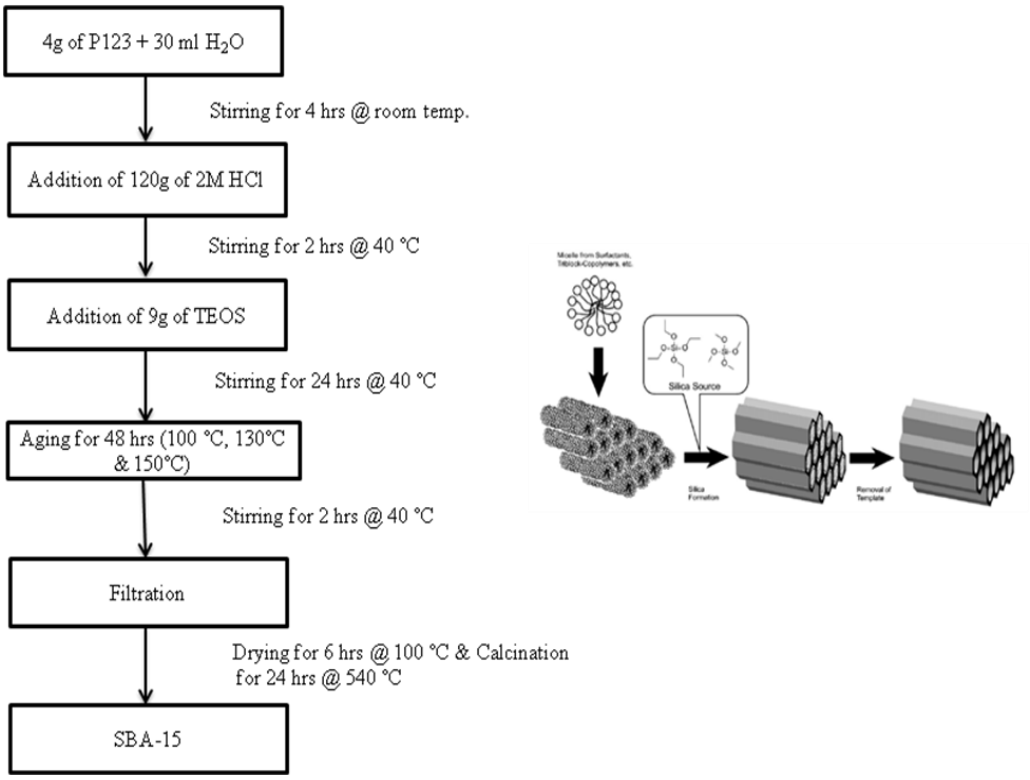

Figure 3-2: SBA15 Synthesis Procedure

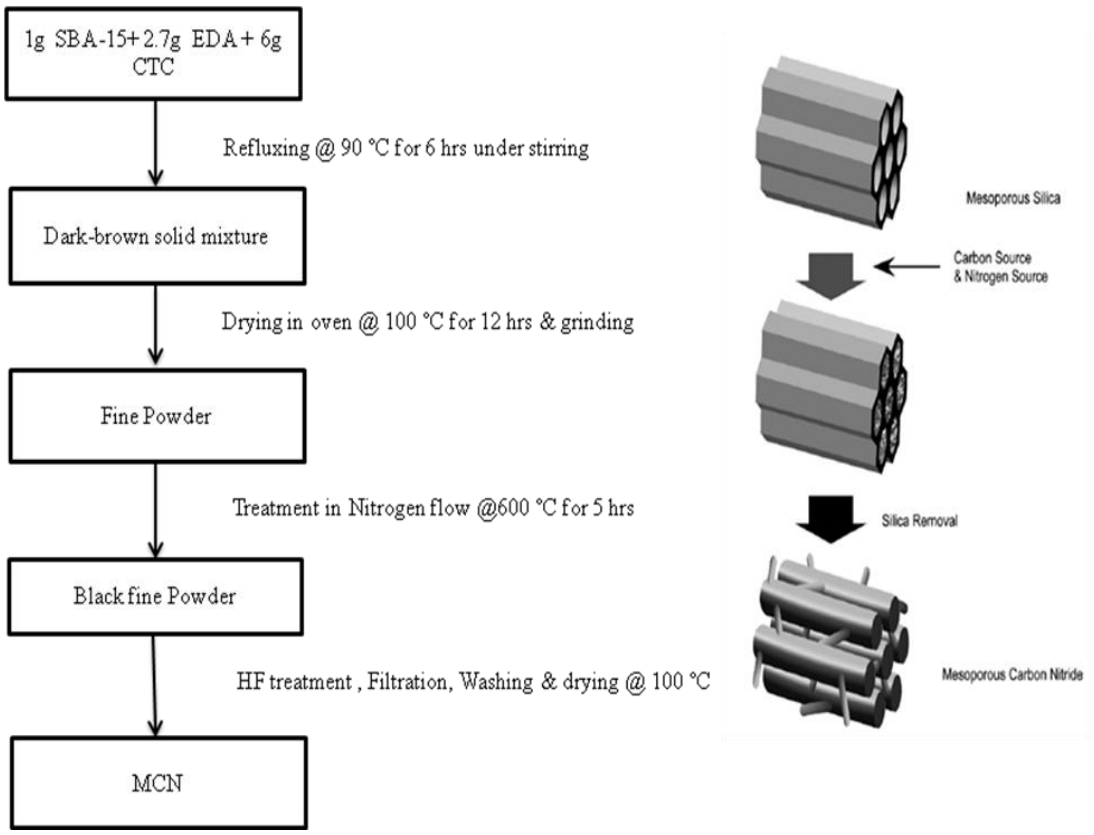

Figure 3-3: MCN Synthesis Procedure

3.3 Nano Metal-Oxides – SBA15 and Nano Metal-Oxides – Mesoporous Carbon (MC) Synthesis

For the synthesis of Fe_2O_3-SBA15, CoO-SBA15, and NiO-SBA15, required amount of SBA15 dispersed in ethanol was added to 0.5M ethanol solution of Iron (III) nitrate Enneahydrate, Cobalt (II) nitrate hexahydrate and Nickel (II) nitrate hexahydrate, respectively. The solutions were stirred for 24 hrs at room temperature and then evaporated to obtain dry powders. This was then followed by oxidation at 300 °C for 3 hrs under oxygen atmosphere to obtain the Fe_2O_3-SBA 15, CoO-SBA 15, and NiO-SBA 15. Then, 1.25 g of sucrose, 5 g of water and 0.14 g of sulphuric acid were mixed together to obtain a solution, which was added drop-wise to 1 g of Fe_2O_3-SBA 15, CoO-SBA 15, and NiO-SBA 15 each. The slurries were dried at 160 °C in an oven and then crushed to obtain fine dry powders. The obtained dried powders were dissolved in a mixture of 0.83 g of sucrose, 5 g of water and 0.093 g of sulphuric acid. The slurries were again dried at 160 °C in an oven and then crushed to obtain fine dry powders. The dried powders were then carbonized at 900 °C, treated with hydrofluoric acid solution, filtered, and washed three times with ethanol. The samples were then dried at 160 °C in an oven for 8 hrs to obtain the Fe_2O_3-MC, CoO-MC, and NiO-MC.

Similarly, for the synthesis of CeO_2-SBA15, PrO_2-SBA15, NdO_2-SBA15 and SmO_2-SBA15, required amount of SBA-15 dispersed in ethanol was added to 0.5M Cerium (III) nitrate hexahydrate solution in ethanol, 0.5M Praseodymium (III) nitrate n-hydrate solution in ethanol, 0.5M Neodymium (III) nitrate hexahydrate solution in ethanol and 0.5M Samarium (III) nitrate hexahydrate solution in ethanol respectively.

The solutions were stirred for 24 hrs at room temperature and then evaporated to obtain dry powders. This was then followed by oxidation at 300 °C for 3 hrs under oxygen atmosphere to obtain the CeO_2-SBA15, PrO_2-SBA15, NdO_2-SBA15 and SmO_2-SBA15. Then, 1.25 g of sucrose, 5 g of water and 0.14 g of sulphuric acid were mixed together to obtain a solution, which was added drop-wise to 1 g of CeO_2-SBA15, PrO_2-SBA15, NdO_2-SBA15 and SmO_2-SBA15 each. The slurries were dried at 160 °C in an oven and then crushed to obtain fine dry powders. The obtained dried powders were dissolved in a mixture of 0.83 g of sucrose, 5 g of water and 0.093g of sulphuric acid. The slurries were again dried at 160 °C in an oven and then crushed to obtain fine dry powders. The dried powders were then carbonized at 900, treated with hydrofluoric acid solution, filtered, and washed three times with ethanol. The samples were then dried at 160 °C in an oven for 8 hrs to obtain the CeO_2-MC, PrO_2-MC, NdO_2-MC and SmO_2-MC. Schematic procedure for the synthesis of nanooxides-SBA15 and nanooxides-MC is shown in Figures 3-4 and 3-5 respectively.

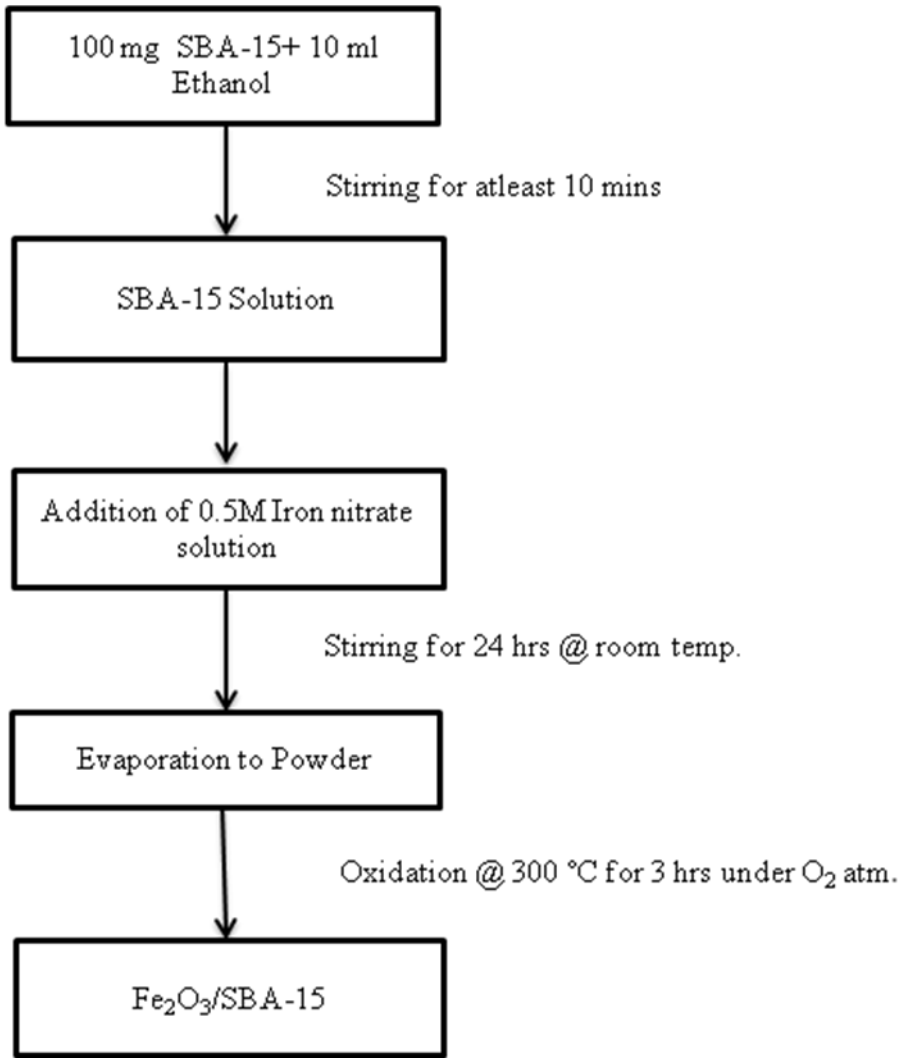

Figure 3-4: Nano Metal-Oxide-SBA15 Synthesis Procedure

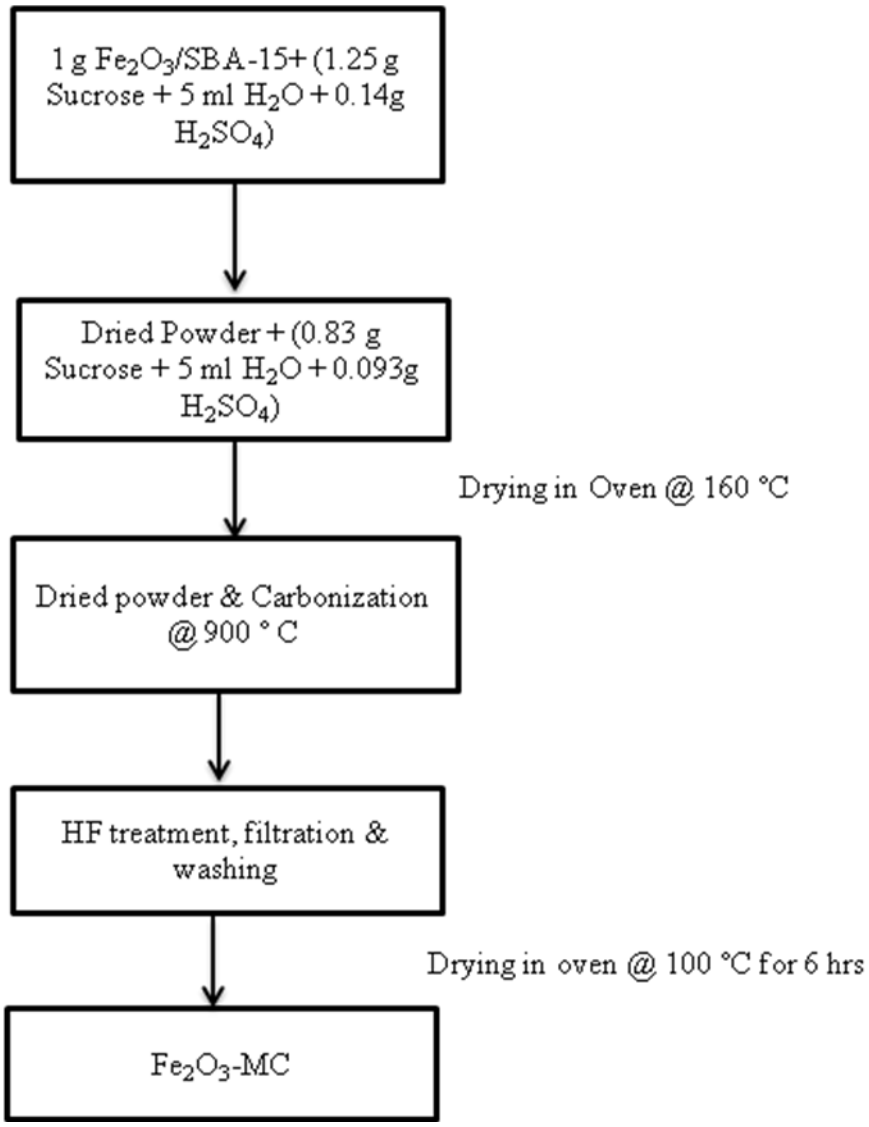

Figure 3-5: Nano Metal-Oxide-Mesoporous Carbon Synthesis Procedure

3.4 Catalysts Preparation

Hydrogen reduction method was used to prepare Pt-Ru/MCN-100, Pt-Ru/MCN-130, Pt-Ru/MCN-150, Pt-Ru/MWCNTs and Pt-Ru/Vulcan XC-72 catalyst samples. In a typical synthesis procedure, the support material, that is, MCN or MWCNTs or Vulcan XC-72 is dispersed in ethanol followed by addition of the metal precursors, that is, hydrogen hexachloroplatinate (IV) hexahydrate ($H_2PtCl_6.6H_2O$), and ruthenium (III) nitrosyl nitrate solution (Ru (NO) $(NO_3)_x$ $(OH)_y$). The mixture was then dried at room temperature in N_2 flow. The dried powder was reduced at 400 °C for 2 hrs in a mixture of H_2 (10%) and He (90%) flow. The PtRu content was 30 wt% with Pt/Ru molar ration of 1:1. Figure 3-6 shows the schematic procedure for the H_2/He reduction method.

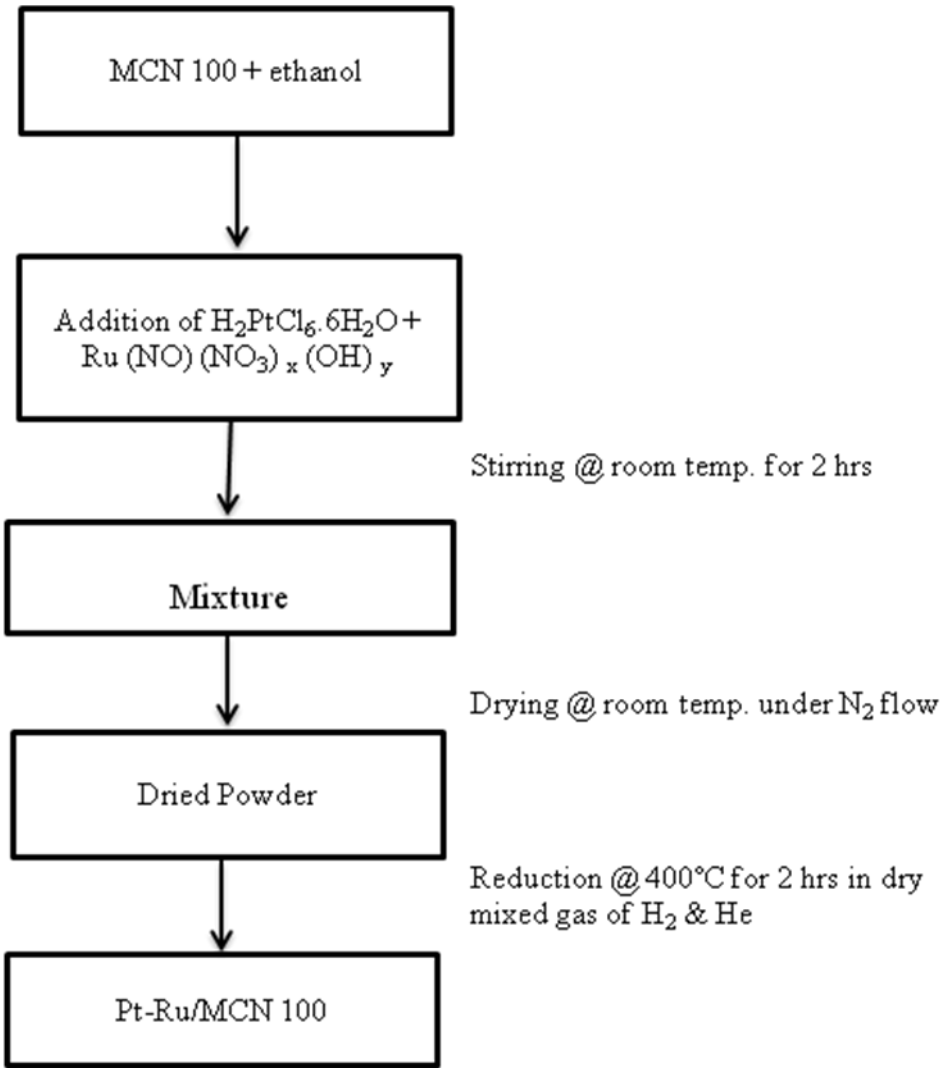

Figure 3-6: H_2/He Reduction Method for Catalyst Synthesis

Sodium borohydride ($NaBH_4$) was used as the reducing agent for the preparation of Pt-Ru/Fe_2O_3-MC, Pt-Ru/CoO-MC, Pt-Ru/NiO-MC, Pt/CeO_2-MC, Pt/PrO_2-MC, Pt/NdO_2-MC and Pt/SmO_2-MC catalyst samples. For the synthesis, Fe_2O_3-MC, CoO-MC, and NiO-MC were dispersed in deionized water, followed by ultrasonication. Then, 100mg of $NaBH_4$ in 5ml deionized water was added immediately. This was followed by rapid addition of the Platinum and Ruthenium precursors, that is, hydrogen hexachloroplatinate (IV) hexahydrate ($H_2PtCl_6.6H_2O$), and ruthenium (III) nitrosyl nitrate solution (Ru (NO) $(NO_3)_x$ $(OH)_y$). The slurries were stirred for 24 hrs at room temperature, filtered, washed with deionized water, and dried in a vacuum oven at 100 for 6 hrs to obtain the Pt-Ru/ Fe_2O_3-MC, Pt-Ru/CoO-MC, and Pt-Ru/NiO-MC catalyst samples. The catalyst composition is 15 wt% PtRu/15 wt% Fe_2O_3/70 wt% MC, 15 wt% PtRu/15 wt% CoO/70 wt% MC & 15 wt% PtRu/15 wt% NiO/70 wt% MC.

Similarly, CeO_2-MC, PrO_2-MC, NdO_2-MC and SmO_2-MC were dispersed in deionized water, followed by ultrasonication. Then, 100mg of $NaBH_4$ in 5ml deionized water was added immediately. This was followed by rapid addition of the Platinum precursor, that is, hydrogen hexachloroplatinate (IV) hexahydrate ($H_2PtCl_6.6H_2O$). The slurries were stirred for 24 hrs at room temperature, filtered, washed with deionized water, and dried in a vacuum oven at 100 °C for 6 hrs to obtain the Pt/CeO_2-MC, Pt/PrO_2-MC, Pt/NdO_2-MC and Pt/SmO_2-MC catalyst samples. The catalyst composition is 15 wt% Pt/15 wt% CeO_2/70 wt% MC, 15 wt% Pt/15 wt% PrO_2/70 wt% MC, 15wt% Pt/15 wt% NdO_2/70 wt% MC and 15 wt% Pt/15

wt% SmO_2/70 wt% MC. Figure 3-7 shows the schematic procedure for the $NaBH_4$ reduction method.

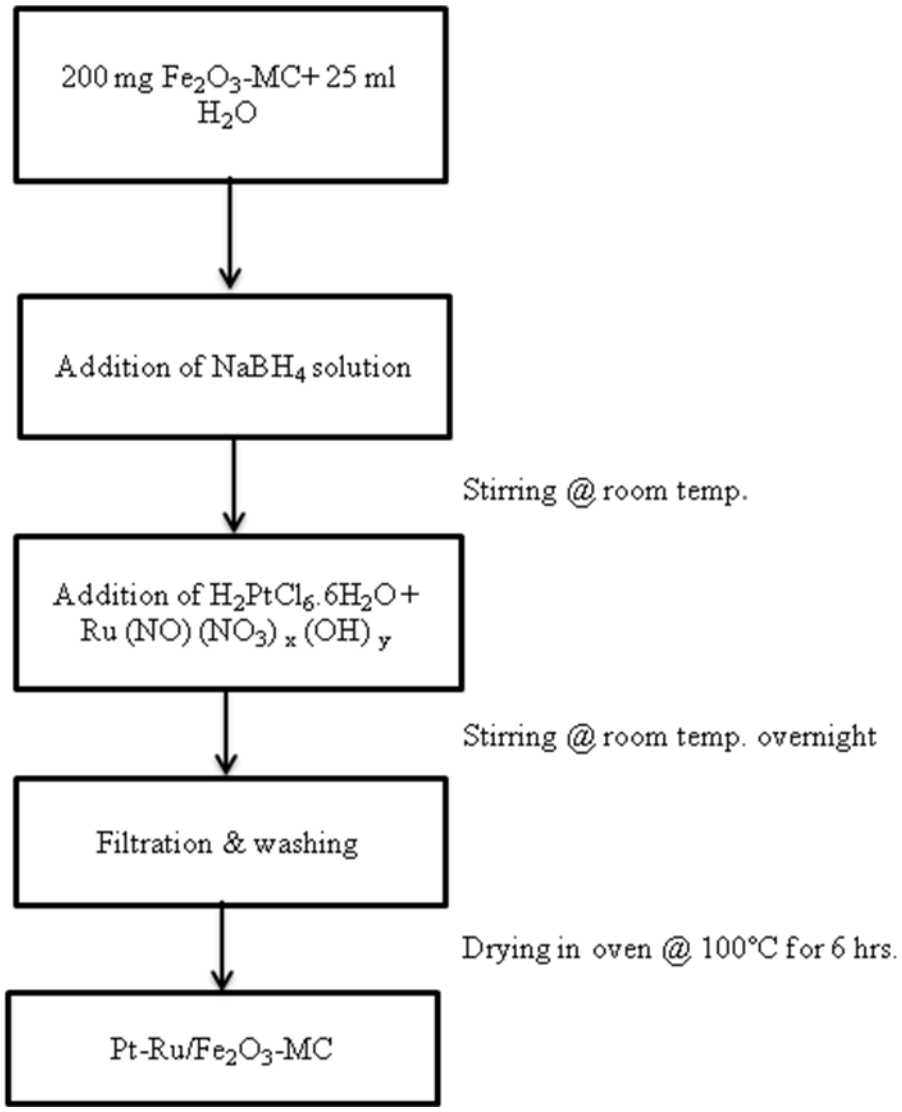

Figure 3-7: $NaBH_4$ Reduction Method for Catalyst Synthesis

3.5 Characterization of the Prepared Nano Metal-Oxides and Catalyst Samples

The surface morphology of the prepared samples was observed using a Hitachi S-4800 field emission scanning electron microscope (FESEM). Nitrogen adsorption and desorption isotherms were measured using a Quantachrome Autosorb 6B sorption analyzer. The specific surface area was calculated using the Brunauer-Emmett-Teller (BET) method. The FT-IR spectra of the prepared samples were recorded on a Perkin Elmer Spectrum 100 FT-IR Spectrometer and the powder X-ray diffraction (XRD) patterns were collected on a Rigaku diffractometer using Cu Kα (λ= 1.54056Å) radiation.

3.6 MEA Fabrication

In order to prepare MEAs, commercial Nafion ® 117 membrane was obtained and pre-treated to exchange the Na^+ cations with H^+ ions in the membrane. The pre-treatment procedure is shown in Figure 3-8. For the catalyst slurry, catalyst loading of 3 $mgcm^{-2}$ and 1 $mgcm^{-2}$ for the anode (the prepared catalyst samples to be tested) and cathode (Pt/C) were used respectively. To determine the amount of catalyst that will give the corresponding catalyst loading, the following relationship is used:

$$m_{catalyst+support} = \frac{\left(2\sigma_{catalyst} \times A_{active}\right)}{f_{catalyst}} \qquad (3.1)$$

where $\sigma_{catalyst}$ is the catalyst loading ($mgcm^{-2}$), A_{active} is the active surface area for the catalyst deposition (cm^2) and $f_{catalyst}$ is the fraction of metal species in the catalyst.

In order to determine the required amount of Nafion solution (which serves as the binder), the following expression is used:

$$m_{Nafion} = \frac{\left(f_{Nafion} \times m_{catalyst+support} \times \left(\frac{1}{0.05}\right)\right)}{1 - f_{Nafion}} \qquad (3.2)$$

The prepared catalyst slurries were then coated on both the membrane and gas diffusion layers and sandwiched together. After drying, the MEAs were hot-pressed in a Carver Press at 130 °C and 1000 psi for 5 minutes.

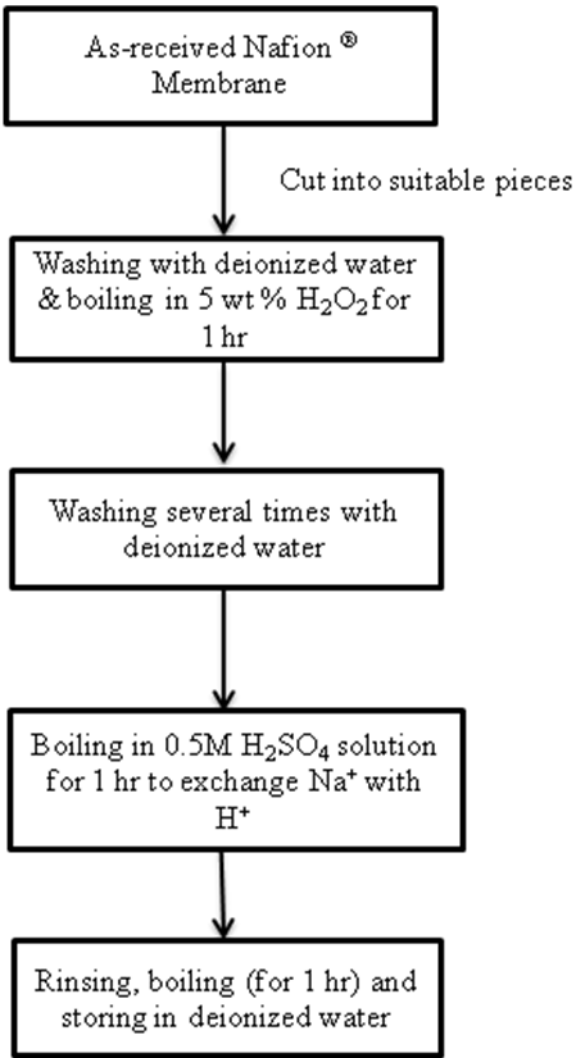

Figure 3-8: Nafion (R) Membrane Pre-treatment for MEA Fabrication

3.7 Catalyst Performance Testing

Electrochemical measurement was conducted using an AUTOLAB Potentiostat (PGSTAT-30 using GPES software). A beaker-type three-electrode cell (5 cm internal diameter x 7 cm height; 135 ml capacity) was employed for the electrochemical test as shown in Figure 3-9. A Platinum wire and saturated calomel electrode (SCE) were used as the counter and reference electrodes respectively. Aqueous catalyst suspensions were prepared by ultrasonically dispersing the catalyst powder in distilled water and 5 wt% Nafion solution. The catalyst suspension was then coated on a copper electrode (about 0.1cm radius and1cm length; 0.03 cm^2 area), which served as the working electrode. After coating onto the copper electrode, the electrode was dried for 90 min at 60 °C. The metals loadings for all the working electrodes were kept the same ~ 4.45 mg/cm^2. Cyclic voltammetry was conducted at 22 °C using a solution of 2M CH_3OH + 1M H_2SO_4. . CVs were recorded using the AUTOLAB Potentiostat. Potential limits of -0.25V to 1.2V, with step increase of 0.003mV and scan rate of 25 mV/s were used.

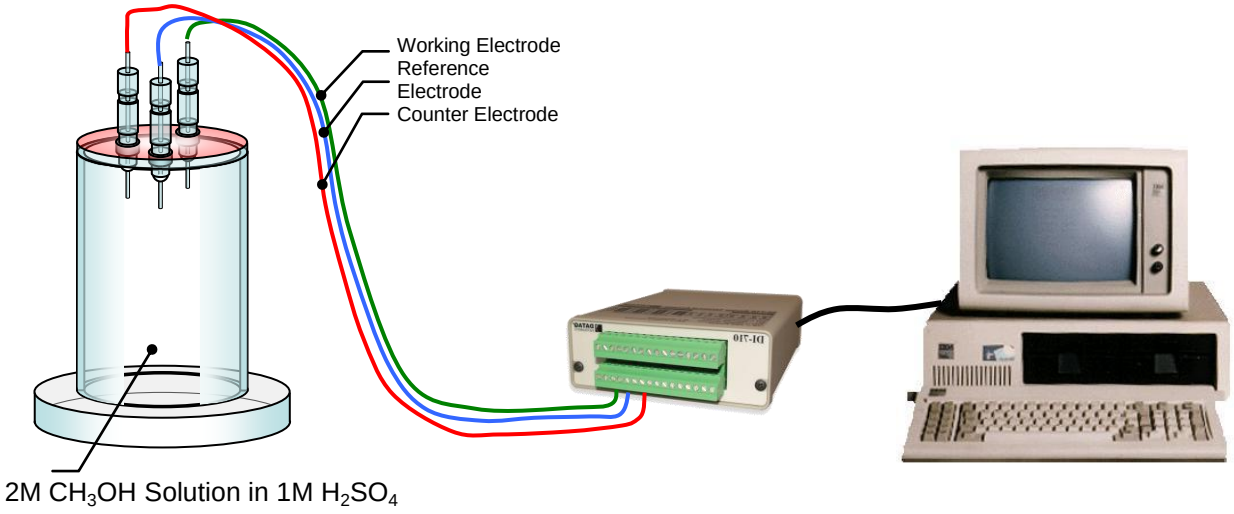

Figure 3-9: Electrochemical Measurement Set-Up for Catalyst Performance Testing

From the cyclic voltammetry results, six (6) catalyst samples were selected and used as anode catalysts for the fabrication of membrane electrode assemblies (MEAs). The catalysts samples are:

- Pt-Ru/MCN 150
- Pt-Ru/MCN 130
- Pt-Ru/MCN 100
- Pt-Ru/F-MWCNTs
- Pt-Ru/Vulcan-XC
- Pt-Ru/C (E-TEK)

CHAPTER 4

4. RESULTS AND DISCUSSION

4.1 High Performance Pt-Ru Methanol Electro-Oxidation Catalysts Supported On Mesoporous Carbon Nitride (MCN)

In this first part, characterization results for mesoporous carbon nitride (MCN) support materials are presented and discussed together with the multi-walled carbon nanotubes (MWCNTs) and traditional Vulcan XC-72, for comparison. In addition, performance evaluation results for the prepared Pt-Ru catalysts supported on MCN materials (Pt-Ru/MCN catalysts) for CH_3OH electro-oxidation is presented, discussed and compared with the performance of the Pt-Ru catalysts supported on MWCNTs and Vulcan XC-72. As mentioned in the methodology section, the MCN was synthesized using SBA15 as a template with different aging temperatures of 100, 130 and 150 °C. The obtained MCN support materials are labeled MCN-100, MCN-130 and MCN-150. The commercial MWCNTs were functionalized using the conventional acid (HNO_3/H_2SO_4) treatment method.

4.1.1 Characterization Results

Figure 4-1 shows the FESEM images obtained for the MCN support material, functionalized MWCNTs and Vulcan XC-72. The MCN material shows hexagonally-ordered honeycomb-like structure with uniform mesoporous channels. The well-ordered arrays of interconnected mesopores imply a P6mm mesostructure, which is expected to play a positive role in the catalysts performance [46]. For the MWCNTs and Vulcan XC-72, a tubular nanostructure (with pore diameter in the nano scale and length up to several micrometers) and a spherical shape are observed, respectively. Even though they are all carbon materials but a clear difference in their surface morphology can be seen, which is attributed to the difference in their preparation procedures. The difference in the surface morphology is expected to influence the synergic interaction between the support materials and the catalysts active species, which will influence the catalysts performance.

a)

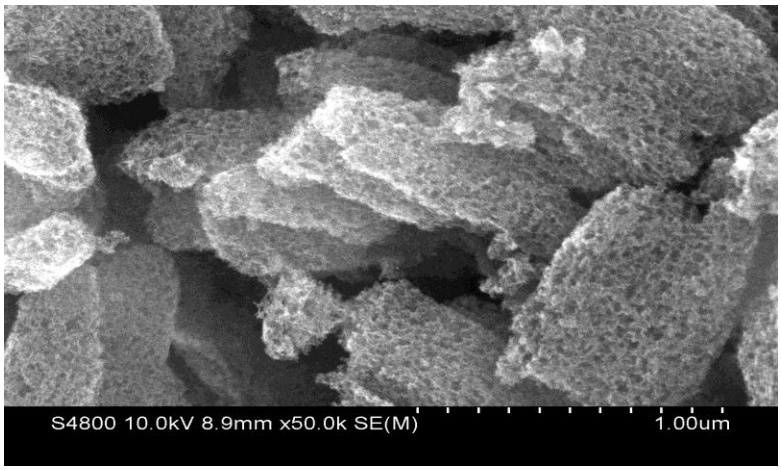

b)

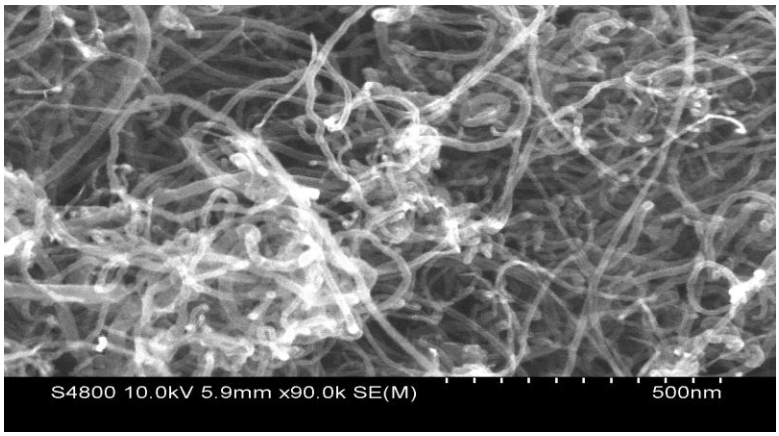

c)

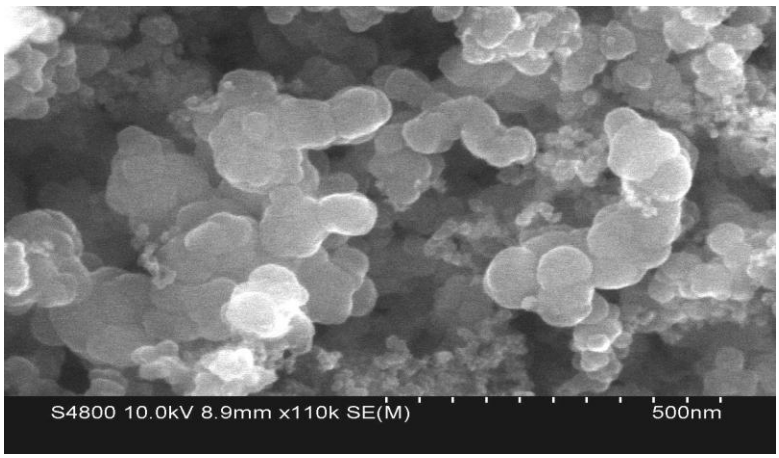

Figure 4-1: FESEM Images of (a) MCN, (b) MWCNTs, (c) Vulcan XC-72

Powder X-ray diffraction (XRD) patterns for the synthesized MCN materials, MWCNTs and Vulcan XC-72, are shown in Figure 4-2. The low angle XRD patterns obtained for the synthesized MCN materials (Figure 4-2a) show diffraction peaks at 2θ of 1.0° and 1.7° (though not sharp), which can be indexed to the (100) and (110) of the hexagonal P6mm space group respectively. The peaks are characteristics of mesoporous materials with a hexagonal arrangement and conform well to the observations previously reported in the literature [46]. In addition, the patterns are similar to those of pure siliceous SBA15 materials indicating that the framework structure of the SBA15 is well maintained.

For the higher angle XRD patterns for the MCN materials, MWCNTs and Vulcan – XC 72 (Figure 4-2b & 4-2c), two broad diffraction peaks appeared near 2θ of 25.0° and 45.0°. These peaks are generally attributed to the presence of carbon material, especially the peak at 2θ of 25.0°. However, the peaks for the MWCNTs and Vulcan XC-72 showed more intensity compared to the peaks for the MCN material. This indicates variation in the crystallinity of the different support materials with MWCNTs being more crystalline.

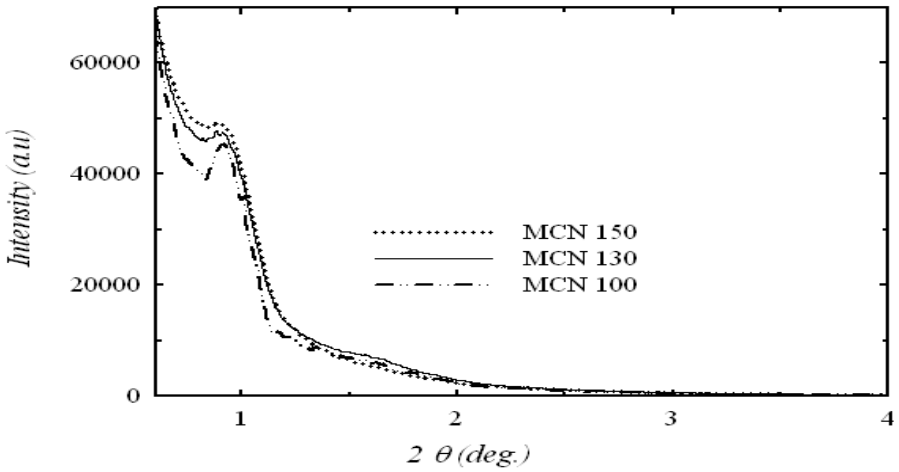

a)

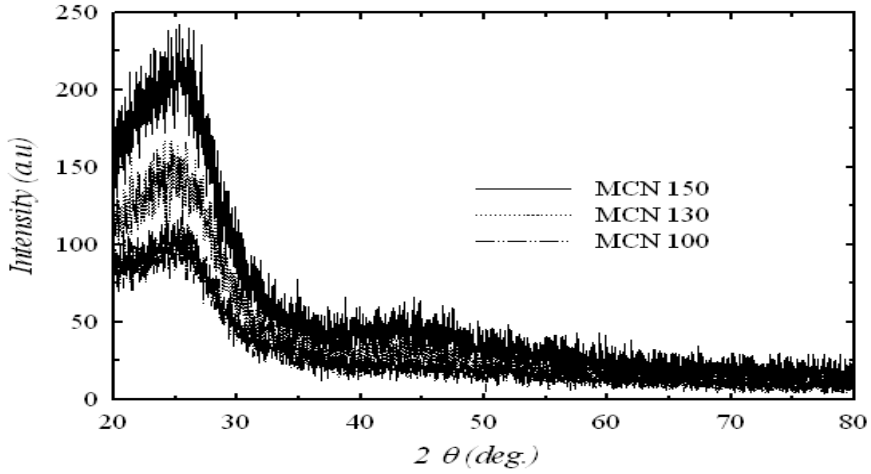

b)

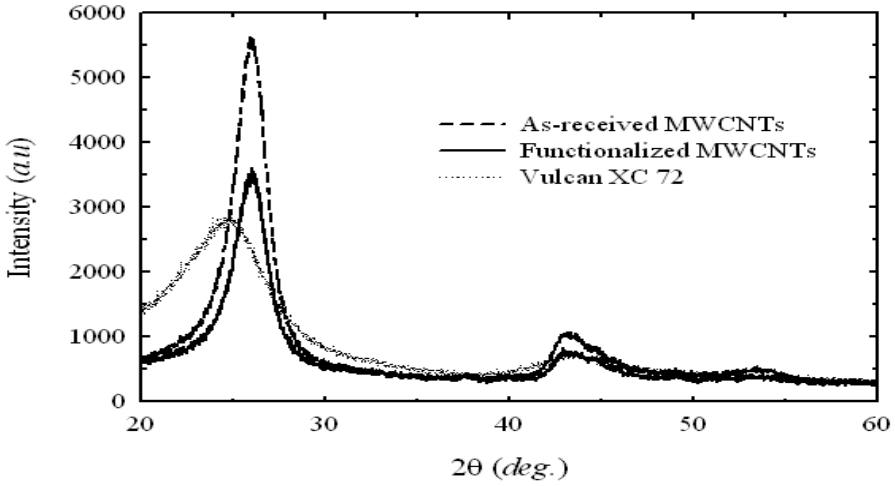

c)

Figure 4-2: Powder XRD Patterns: (a) Low Angle for MCN, (b) High Angle for MCN, (c) High Angle for Vulcan XC-72 and MWCNTs

Figure 4-3 shows the FT-IR spectra obtained for the MCN materials, F-MWCNTs and Vulcan XC-72. Several peaks can be observed that represent different functional groups. Broad peak at 1480 - 1580 cm^{-1} is clearly observed for the MCN materials, which is important in characterizing the chemical state of N and is assigned to N-H vibrations of the NH_2 group [44, 116]. This implies that the NH_2 groups exist on the MCN surface, which would be beneficial for the anchoring of the Pt-Ru particles. As shown in the methodology section (Chapter 3), ethylene diamine (EDA) was used during the MCN materials preparation, which is expected to be the source for the NH_2 groups. In comparison with other samples, much stronger absorption bands were found at 900 – 1050 cm^{-1} for the F-MWCNTs, which indicates that a high density of surface functional groups, such as C-OH and –C=O, are created on the surface of the F- MWCNTs [117]. In addition, the peak near 1700 cm^{-1} suggests that carboxylic acid groups were attached on the surface of the F-MWCNTs [118].

The type and number of functional groups attached to a support material have significant influence on the suitability of the material for use as a support for the preparation of methanol electro-oxidation catalysts. This is because the type of functional groups available on the surface of a support material affects the degree of metal active specie (s) affection to it. In addition, the availability of more functional groups implies more space where the active metal specie can be anchored.

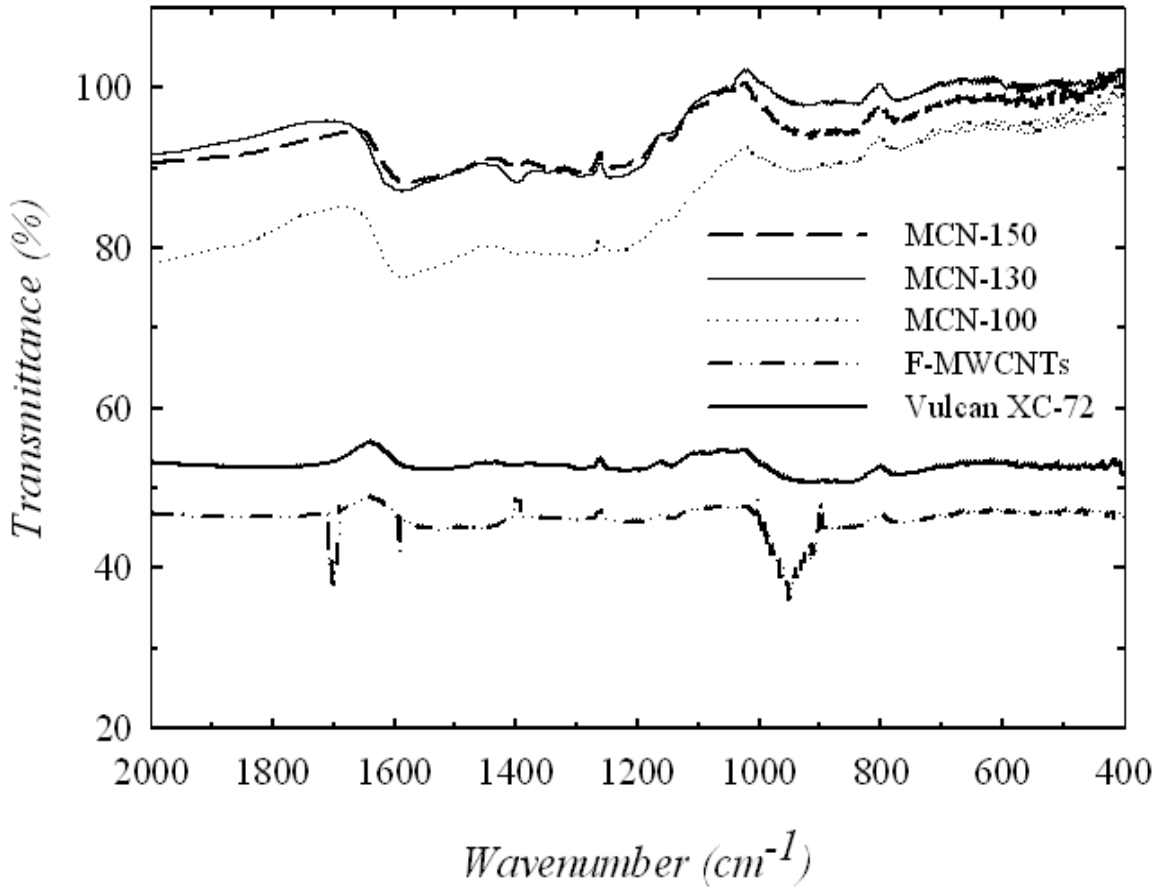

Figure 4-3: FT-IR Spectra of the Support Materials

Figure 4-4 shows N_2 adsorption-desorption isotherms and pore size distribution for the MCN materials, F-MWCNTs and Vulcan XC-72. In Figure 4-4a, all the isotherms for the MCN materials show a typical Type 1V model according to the IUPAC classification and have a H1 hysteresis loop at the high pressure side that is representative of mesopores. The type 1V adsorption isotherm characterizes the existence of mesoporosity of the MCN samples, which plays an important role in dispersing the metal active species. The shape of the N_2 adsorption-desorption isotherms further confirms that a well ordered mesoporous structure was obtained for the MCN materials. The sharp inflections between the relative pressures (P/P_0) 0.45 - 0.85 in the isotherms especially for the MCN-130 and MCN-150 samples correspond to capillary condensation within the uniform mesopores. The sharpness of the inflection step demonstrates the extent of uniform pore size distribution in the MCN samples.

The pore size distribution derived from desorption branch of the N_2 hysteresis for the MCN materials, F-MWCNTs and Vulcan XC-72 is shown in Figure 4-4b. The well-known BJH method was used to analyze the desorption branch of the isotherms at relatively high pressure to obtain the pore size distribution of the support samples. The presence of mesopores is expected to enhance deposition of the metal active species. It has been reported in the literature that molecules within microporous channels could suffer significantly hindered transport, while molecules in mesoporous channels can approach diffusion rates comparable to those in an open medium [119]. The textural parameters such as specific surface area, pore volume and pore diameter, are given in Table 4-1.

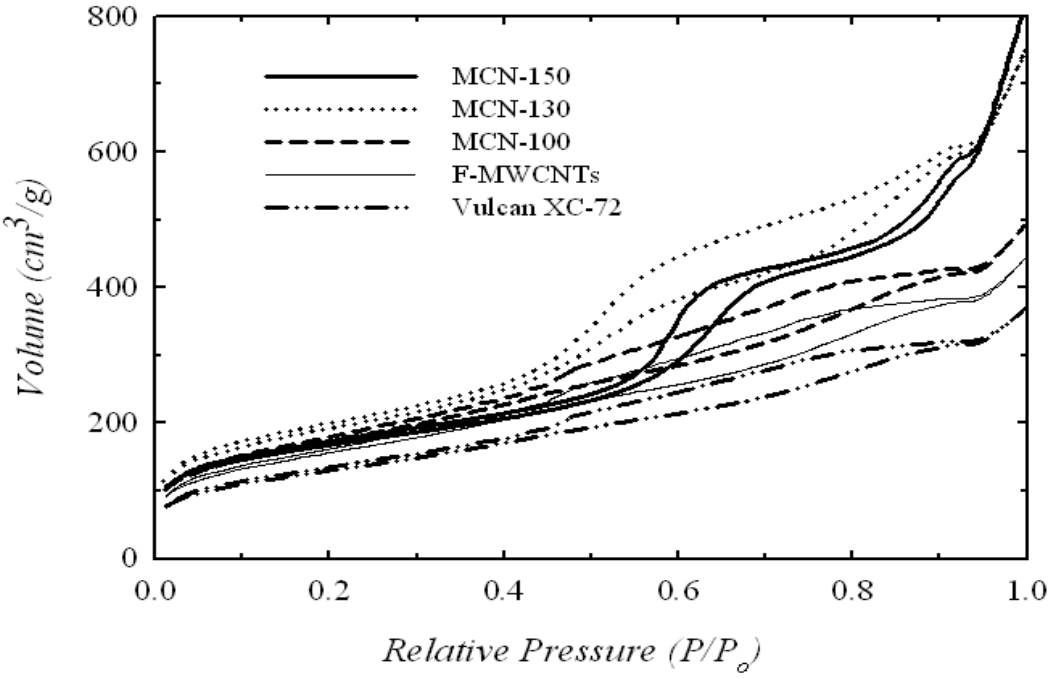

a)

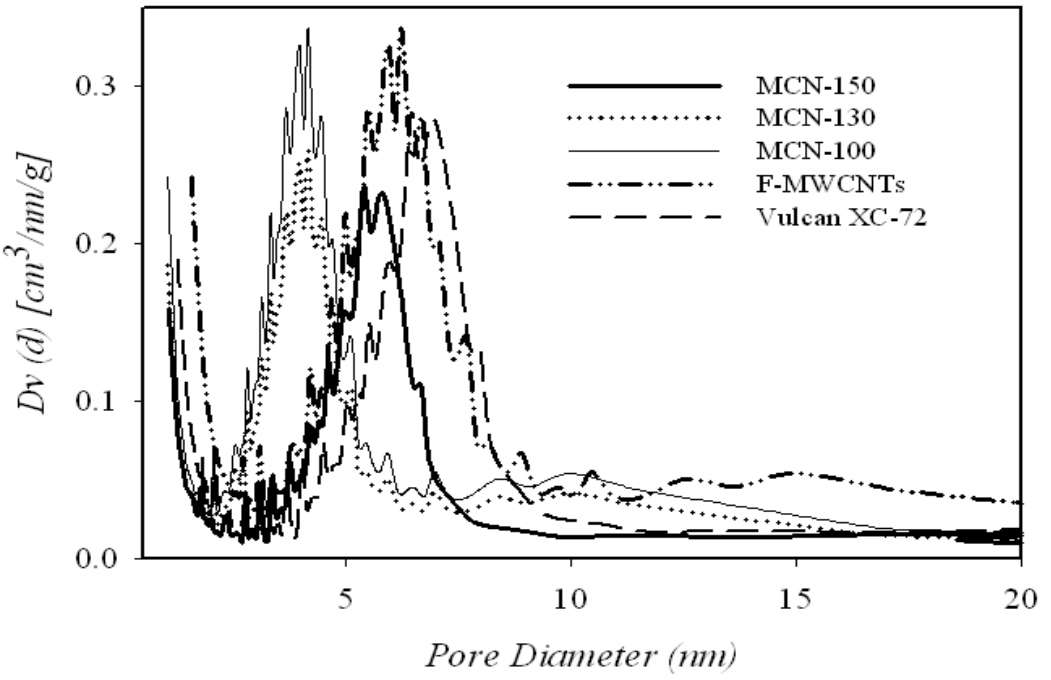

b)

Figure 4-4: (a) N_2 Sorption Isotherms for the Support Materials, (b) Pore Size Distribution

Table 4-1: Pore Structure for the Support Materials

Support Material	BET Surface Area ($m^2 g^{-1}$)	Total Pore Volume ($cm^3 g^{-1}$)	Average Pore Diameter (nm)
MCN-100	630	0.95	5.9
MCN-130	688	0.96	4.3
MCN-150	597	0.87	6.4
F - MWCNTs	255	0.63	6.7
Vulcan XC 72	230	0.57	6.8

It can be observed from the table that the MCN materials showed higher specific surface area (particularly MCN-130 with 688 m^2/g) and larger pore volume. The unique high surface area and pore volume exhibited by the MCN materials is mainly due to their preparation method. The high specific surface area will contribute significantly in achieving excellent dispersion of the metal active species during the catalysts synthesis. On the other hand, the MCN materials exhibited lower pore diameter particularly MCN-130 sample with 4.3 nm. The low pore diameter may result in restricted access of the pores by the metal active species (Pt-Ru) particles during the catalysts synthesis, which will negatively affect the performance of the catalysts. However, the specific surface area, pore volume and pore diameter of the MCN materials can be tuned depending on the preparation procedure to suit a particular application, which makes the MCN materials very versatile [46].

Figure 4-5 shows the UV-Vis spectra for the support materials. It can be observed that only one sharp peak appeared around 210-220 nm wavenumber, which indicates that all the samples are homogeneous in nature.

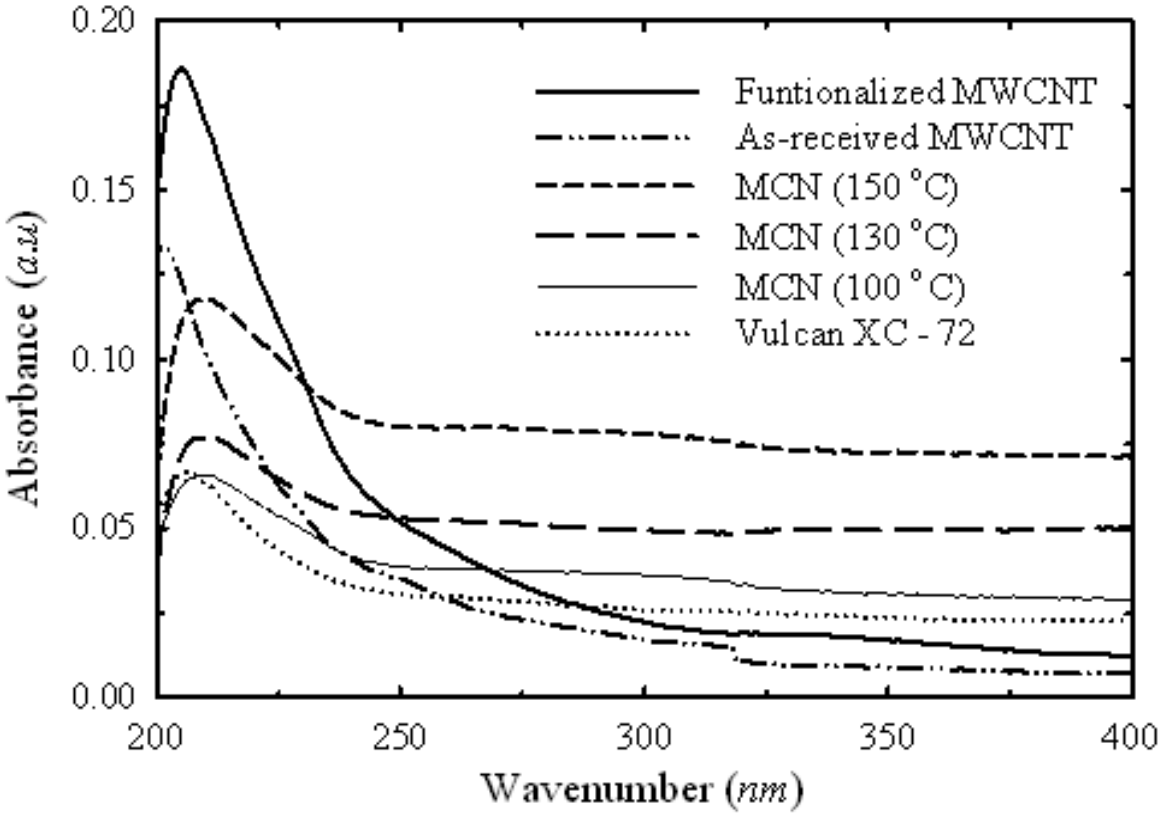

Figure 4-5: UV-Vis Spectra of the Support Materials

The MCN materials, F-MWCNTs and Vulcan XC-72 were used as support to prepare PtRu-based methanol electro-oxidation catalysts as discussed in the methodology section (Chapter 3). Figure 4-6 shows high angle powder XRD patterns obtained for the prepared catalyst samples. In all the samples, the presence of the face-centred cubic (fcc) structure typical of platinum metal could be inferred from the strong diffractions represented by the crystalline planes (111), (200), and (220), near 2θ of 40.0°, 46.0°, and 68.0° respectively.

As mentioned earlier, the peak at 2θ of 25.0° is mainly due to the carbon support. Comparison of the peaks intensity reveals that the Pt-Ru/MCN-100, Pt-Ru/MCN-130 and Pt-Ru/MCN-150 samples showed high intensity relative to the Pt-Ru/Vulcan XC-72 and Pt-Ru/F-MWCNTs samples, which suggests better crystallinity in the Pt-Ru/MCN-100, Pt-Ru/MCN-130 and Pt-Ru/MCN-150 samples. In the course of the catalysts reduction with hydrogen, three scenarios have been reported: (1) Ru segregates into a separate phase and forms monometallic nanoparticles, (2) Ru metal is segregated onto the surfaces of alloy particles, or (3) bimetallic RuM alloy particles are formed [120 121].

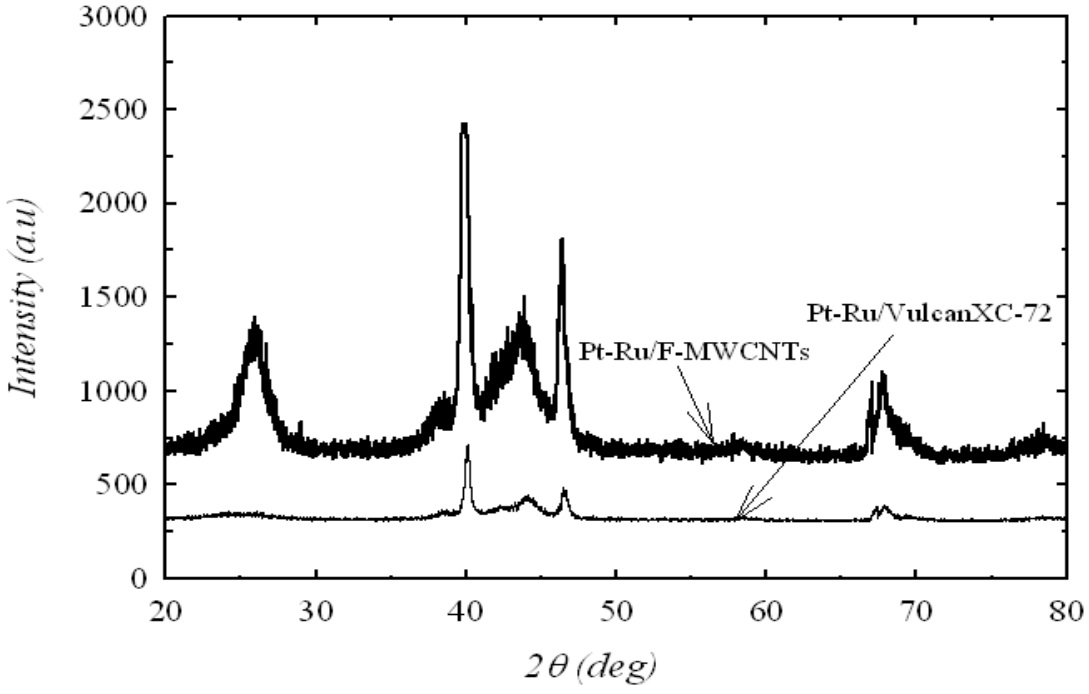

a)

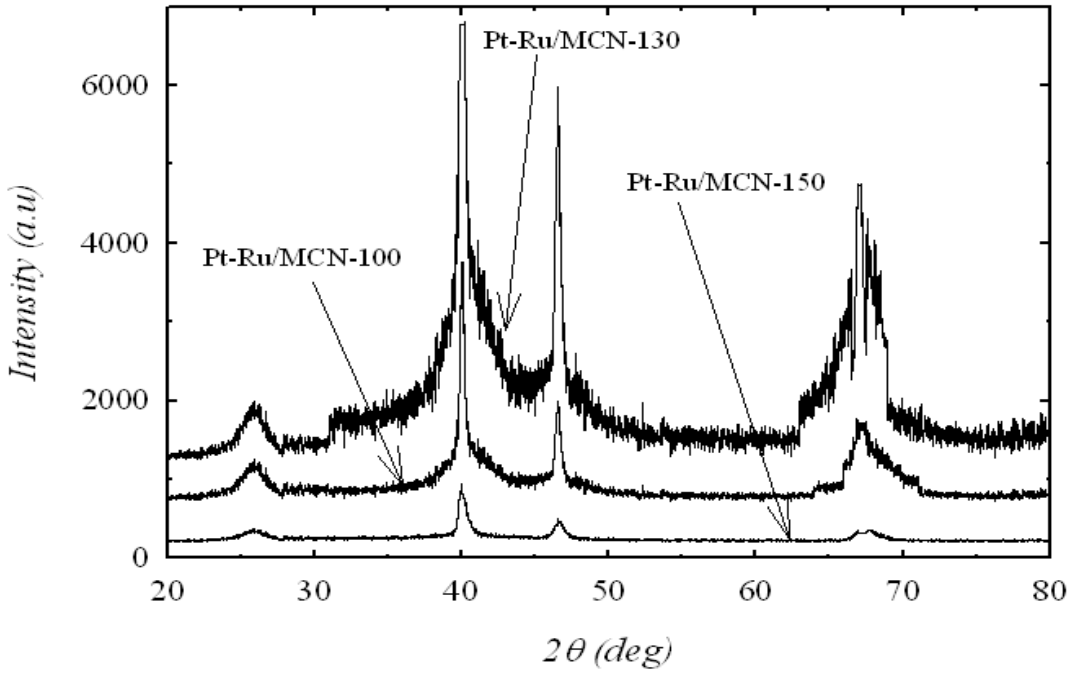

b)

Figure 4-6: High Angle Powder XRD Patterns: (a) Pt-Ru/Vulcan XC-72 and Pt-Ru/F-MWCNTs (b) Pt-Ru/MCN-100, Pt-Ru/MCN-130 and Pt-Ru/MCN-150 Catalyst Samples

In the present case, the XRD patterns for the Pt-Ru/Vulcan XC-72 and Pt-Ru/F-MWCNTs catalyst samples show the (101) and (102) Ru reflections near 44.0 º and 58.0 °; 2θ, which illustrates that Ru is segregated in a separate phase. However, it has been suggested that Ru promotes the dispersion of the electro-catalyst; the unalloyed amorphous material that may reside on or near the surface of the Pt-Ru alloy particles may help prevent sintering during the deposition or during the thermal reduction processes [122]. This is one of the reasons why smaller particle size for Pt-Ru/Vulcan XC-72 as compared with the Pt/Vulcan XC-72 catalyst is normally observed. In the Pt-Ru/MCN-100, Pt-Ru/MCN-130 and Pt-Ru/MCN-150 catalyst samples, peaks associated with metallic Ru were not observed; it is contained in bimetallic (Pt-Ru) alloy nanoparticles. The Pt-Ru crystal size was calculated using the Debye-Scherrer's equation [123]:

$$D = \frac{K \lambda_{CuK\alpha}}{B_{2\theta} \cos \theta_{\max}} \tag{4.1}$$

where D is the crystal size, K is the shape factor (0.9), $\lambda_{CuK\alpha}$ is the K radiation from Cu (1.54056 Å), $B_{2\theta}$ is the full width at half maximum (corrected value, taking into account instrument contribution), and θ_{max} is the angle at maximum peak.

The d-spacing and lattice parameter were determined using the Bragg's equation and the relationship between d-spacing and lattice parameter for cubic systems respectively:

$$d_{hkl} = \frac{\lambda}{2 \sin \theta} \tag{4.2}$$

$$\frac{1}{\left(d_{hkl}\right)^2} = \frac{h^2 + k^2 + l^2}{a^2} \tag{4.3}$$

where d_{hkl} is the d-spacing (Å), h, k, and l are the miller indices, and a is the lattice parameter

In order to determine the Pt-Ru crystal size, the (220) reflection was used because even though it is not the strongest, it is completely outside the region of the broad band produced by the carbon support, thus there is no overlap. Pt-Ru crystal size and lattice parameter for the prepared catalyst samples are given in Table 4-2. From the Table, it can be seen that Pt-Ru/MCN-130 showed the least Pt-Ru crystal size of 1.7 nm, which is desirable for good dispersion while Pt-Ru/Vulcan XC-72 showed the highest Pt-Ru crystal size of 2.5 nm. In terms of lattice parameter (a), Pt-Ru/MCN-130 showed the highest value of 3.8962 Å while Pt-Ru/Vulcan XC-72 showed the least value of 3.8662 Å.

In general, it can be observed that the MCN supported catalyst samples showed lower Pt-Ru crystal size and higher lattice parameter. This indicates that the MCN support materials allow better dispersion of the Pt-Ru particles, which prevents the coalescence of the growing nuclei. However, it should be mentioned that when the surface area of a support material is too large, it can result into a situation where the Pt-Ru crystals are scattered too much apart, which will negatively affect the catalyst performance.

Table 4-2: XRD Data Analysis Results for the Prepared Catalyst Samples

Catalyst Sample	Peak Position at fcc 220 (*deg*)	FWHM (*rad*)	Crystal Size (*nm*)	d_{hkl} (*Å*)	Lattice Parameter (*Å*) (a)
Pt-Ru/Vulcan XC-72	68.6	0.0663	2.5	1.3669	3.8662
Pt-Ru/F-MWCNTs	68.4	0.0750	2.2	1.3704	3.8761
Pt-Ru/MCN-100	68.2	0.0820	2.0	1.3739	3.8860
Pt-Ru/MCN-130	68.0	0.0960	1.7	1.3775	3.8962
Pt-Ru/MCN-150	68.3	0.0785	2.1	1.3722	3.8812

4.1.2 Performance Test Results

The catalytic activities of the prepared catalyst samples for CH_3OH electro-oxidation were measured using the cyclic voltammetry technique. Figure 4-7 shows the cyclic voltammogram curves for the commercial Pt-Ru/C (E-TEK) in the electrolyte (H_2SO_4) solution only. The CV spectrum of the Pt-Ru/C (E-TEK) shows that hydrogen desorbed in the anodic potential sweep near - 0.15V vs. SCE. A weak hydrogen adsorption peak is observed during the cathodic potential sweep between 0.4 and 0.25 V. However, it is clear that no CH_3OH electro-oxidation peak is observed (as expected) due to the absence of CH_3OH.

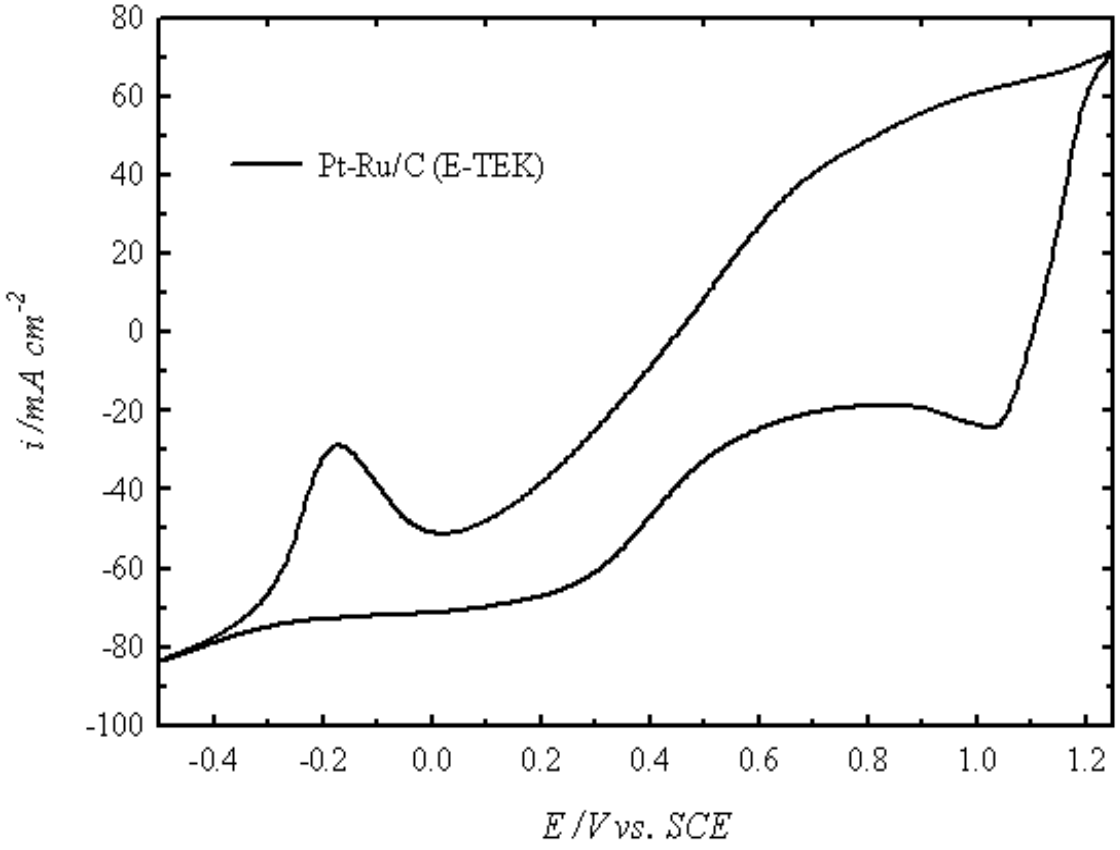

Figure 4-7: CV Curve for the Pt-Ru/C (E-TEK) in 1M H_2SO_4 at a Scan Rate of 25 mV/s

Figure 4-8 shows the cyclic voltammetry (CV) curves for the Pt-Ru/MCN-100, Pt-Ru/MCN-130, Pt-Ru/MCN-150, Pt-Ru/F-MWCNTs and Pt-Ru/Vulcan XC-72 for CH_3OH electro-oxidation activity determination. In addition, commercial Pt-Ru/C (E-TEK) catalyst is included for comparison. The CV was conducted in deaerated 1M H_2SO_4 + 2M CH_3OH solution (1 - 2.5M is the most commonly used). The anodic peaks for CH_3OH electro-oxidation are clearly observed for all the catalyst samples between 0.62 – 0.69 V. Highest CH_3OH electro-oxidation peak is observed for the Pt-Ru/MCN-150 catalyst sample. As shown in Table 4-3, Pt-Ru/MCN-150, Pt-Ru/MCN-100 and Pt-Ru/F-MWCNTs showed higher activity compared to the commercial Pt-Ru/C (E-TEK). In addition, they exhibited low onset potential for CH_3OH electro-oxidation than the commercial Pt-Ru/C (E-TEK), which further confirms their superiority for CH_3OH electro-oxidation.

However, Pt-Ru/MCN-130 showed a slightly lower activity than the commercial Pt-Ru/C (E-TEK) even though it has the lowest average Pt-Ru crystal sizes and the MCN-130 support material showed the largest surface area, which usually enhances better dispersion of the metal species. Its lower activity is believed to be partly due to the largest surface area of the MCN-130 support material, which gave the lowest pore diameter, lowest difference between the Pt-Ru crystal size and the support pore diameter of 2.6 nm and the highest inter-distance between the PtRu-PtRu particles.

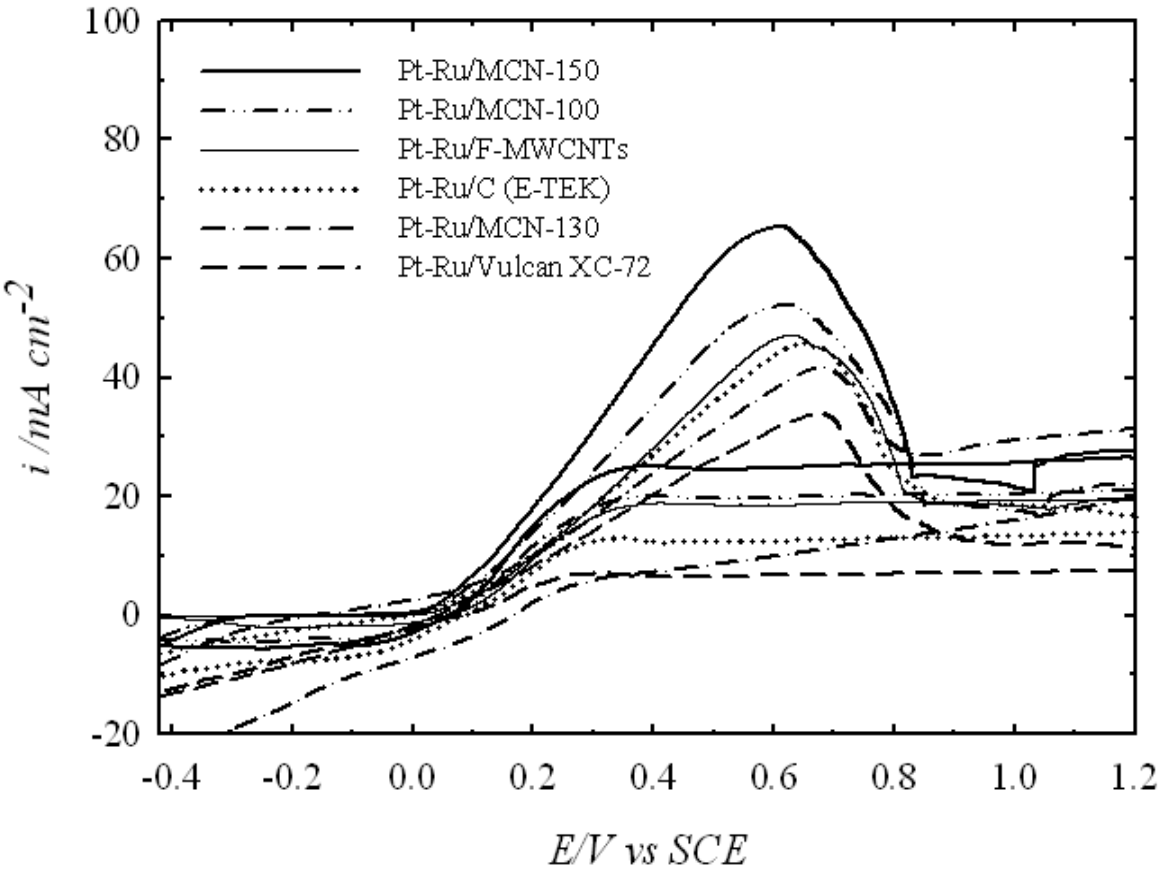

Figure 4-8: CV Curves for the Prepared Catalysts Activity in 2M CH_3OH + 1M H_2SO_4 at a Scan Rate of 25 mV/s

When the difference between the support pore diameter and the metals crystal size is low, the metal species may find it difficult to freely move into the pores of the support material. In addition, large surface area may result in the metal active species been dispersed too much apart. Thus, an optimum surface area is required for enhanced activity. Similar observations are reported in the literature [36, 124 125].

For the Pt-Ru/F-MWCNTs, as observed in this study, several other studies have also reported enhanced activity of Pt-Ru catalyst supported on carbon nanotubes compared to the commercial Pt-Ru/C (E-TEK). However, as shown in Table 4-3, the commercial Pt-Ru/C (E-TEK) showed better activity compared to the Pt-Ru/Vulcan XC 72 that was prepared in our laboratory even though the same support material was used. This implies that apart from the type of support material, method of preparation also affects a catalyst activity.

Table 4-3: CV Analysis Results for the Prepared Catalysts and Commercial E-TEK

Catalyst Sample	Peak Position *V* vs SCE	Current Density (mA/cm^{-2})	Mass Activity (mA/mg)
Pt-Ru/MCN 150	0.62	65	14.61
Pt-Ru/MCN 100	0.63	52	11.69
Pt-Ru/F-MWCNTs	0.65	47	10.56
Pt-Ru/C (E-TEK)	0.66	45	10.11
Pt-Ru/MCN 130	0.68	42	9.44
Pt-Ru/Vulcan XC -72	0.69	34	7.64

In addition to the CH_3OH electro-oxidation activity, preliminary test was also carried out to determine the catalysts tolerance (stability) to the adsorbed carbon monoxide and other organic intermediates. Figure 4-9 shows the CV curves obtained for the Pt-Ru/MCN-150 catalyst sample for 20 scans at a scan rate of $25mVs^{-1}$. It is observed that there is a speedy decrease in activity from the 1^{st} to the 10^{th} scan. This is attributed to the high activity of the Pt-Ru/MCN-150 catalyst sample, which leads to rapid production of the intermediates such as the adsorbed carbon monoxide during the methanol electro-oxidation. If the kinetics of the removal of the intermediates cannot keep pace with that of methanol electro-oxidation then a fast decay will occur.

The preliminary stability test was also conducted for all the prepared catalyst samples and the commercial Pt-Ru/C (E-TEK), for comparison. A more gradual decay was observed for the commercial Pt-Ru/C (E-TEK), Pt-Ru/Vulcan XC 72, Pt-Ru/F-MWCNTs and Pt-Ru/MCN-100. Figure 4-10 shows the 20^{th} scan of the CV curves for all the catalyst samples while Figure 4-11 shows the variation in mass activity with time for the catalyst samples. The catalysts mass activity decreased by 21.3%, 24.43%, 25.1%, 26.4%, 33.4% and 38.5% from its initial value for the Pt-Ru/F-MWCNTs, commercial Pt-Ru/C (E-TEK), Pt-Ru/MCN-100, Pt-Ru/Vulcan XC 72, Pt-Ru/MCN-130 and Pt-Ru/MCN-150 respectively. In general, a reasonable stability was achieved after about 1hr 30 mins. for all the catalyst samples during the CH_3OH electro-oxidation.

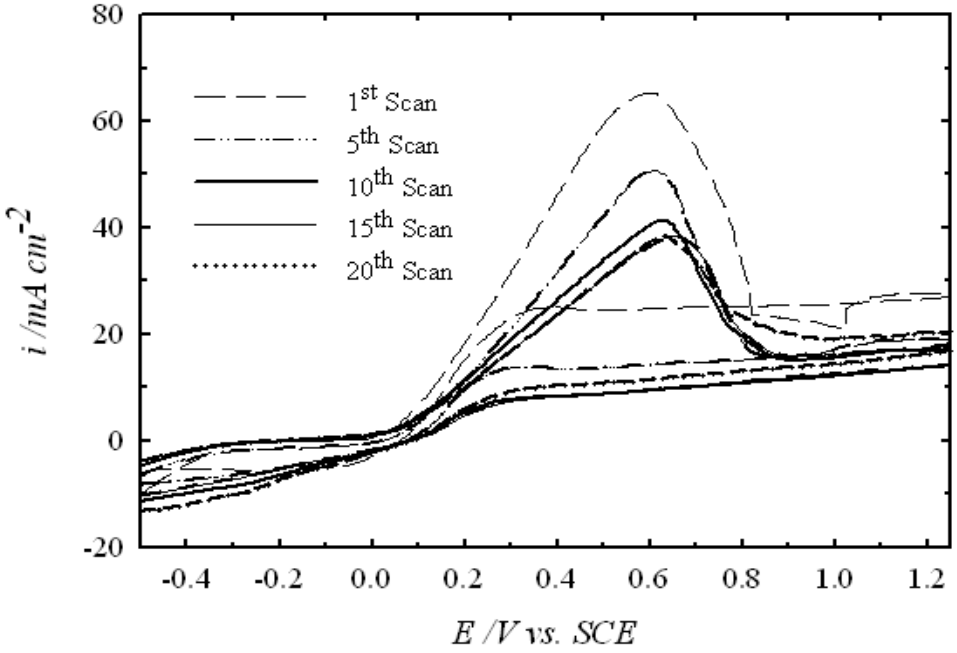

Figure 4-9: CV Curves for Stability Test of the Pt-Ru/MCN-150 Catalyst in 2M CH_3OH + 1M H_2SO_4 at a Scan Rate of 25 mV/s

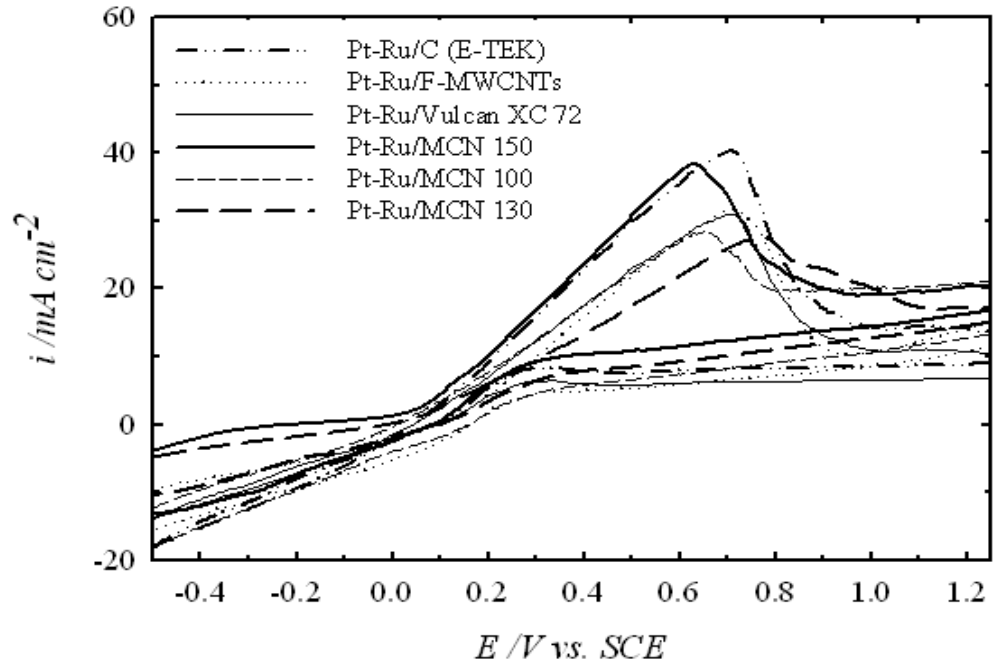

Figure 4-10: CV Curves for Stability Test for all the Prepared Catalysts in 2M CH_3OH + 1M H_2SO_4 at a Scan Rate of 25 mV/s

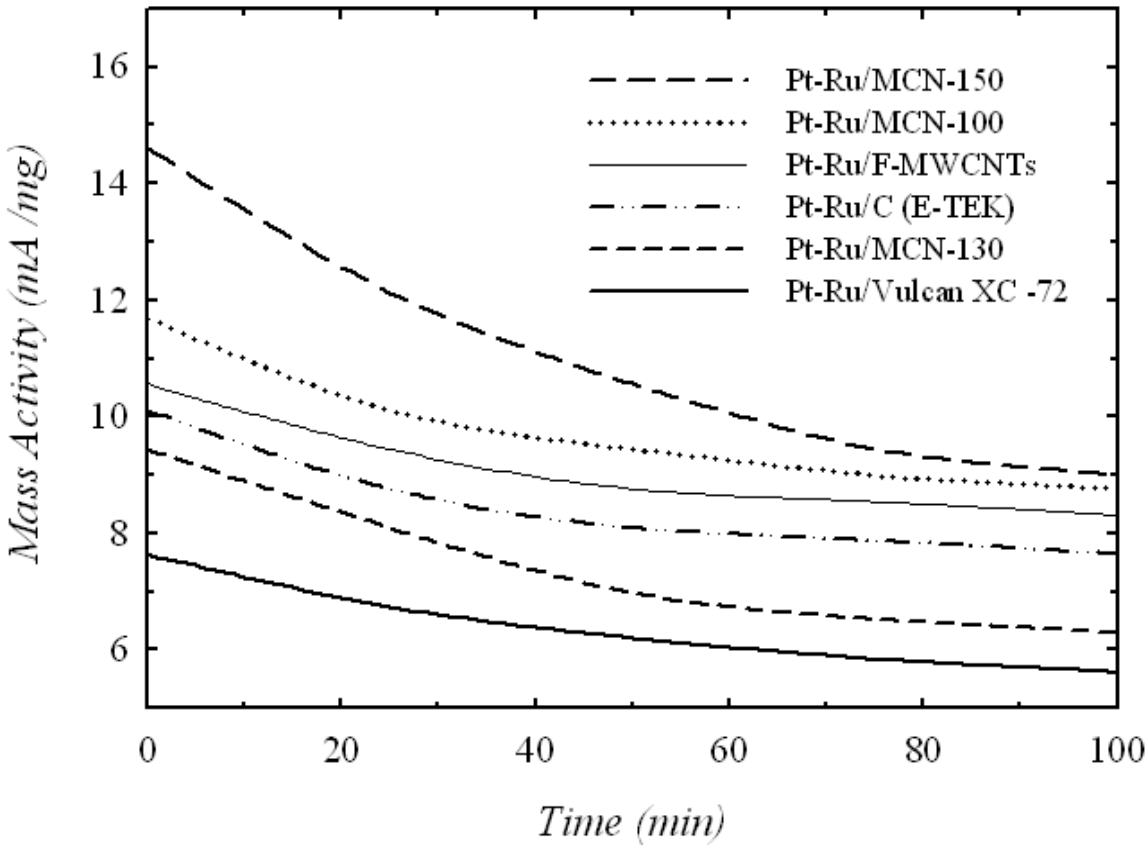

Figure 4-11: Variation in Mass Activity with Time for the Catalyst Samples

4.2 Novel Method to Prepare Ternary Catalysts for Methanol Electro-oxidation

In this second part, a novel approach was used to prepare Pt-Ru/Fe_2O_3-MC, Pt-Ru/CoO-MC and Pt-Ru/NiO-MC methanol electro-oxidation catalysts. Incorporation of transition metals into the PtRu catalysts to form ternary catalysts in order to improve the performance of the PtRu catalysts is one of the techniques attracting a lot of interest. To the best of my knowledge, in all the published literature, the Pt, Ru and third metal are dispersed simultaneously into the support material. This procedure can cause agglomeration of the metal active species, especially when the support surface area is not very large such as the traditional Vulcan XC-72 and carbon nanotubes (~ 250 m^2/g). The agglomeration of the metal active species will negatively affect the performance of the catalyst system, which reduces the overall efficiency of the direct methanol fuel cell.

Therefore, in this work, a new approach was used wherein nano-oxide of the third metal active specie is dispersed during synthesis of the support material, which is mesoporous carbon. This offers two main advantages. Firstly, mesoporous carbon generally has large surface area and more uniform interconnected pores compared to the traditional Vulcan XC-72 or carbon nanotubes. Secondly, by dispersing one of the metal species during the synthesis of the mesoporous carbon provides a large surface area mesoporous carbon containing nano metal-oxide (e.g. Fe_2O_3-MC), which allows for subsequent efficient dispersion of the nano-particles of the remaining two metal active species (Pt-Ru).

The new method involves synthesizing SBA15 initially, followed by synthesis of transition nano metal-oxide in SBA15 that is, Fe_2O_3-SBA15, CoO-SBA15 and NiO-SBA15. The obtained materials were then carbonized to form nano metal-oxide in mesoporous carbon, that is, Fe_2O_3-MC, CoO-MC and NiO-MC. Then the obtained high surface area Fe_2O_3-MC, CoO-MC and NiO-MC were impregnated with the Pt-Ru nanoparticles respectively, to form Pt-Ru/Fe_2O_3-MC, Pt-Ru/CoO-MC and Pt-Ru/NiO-MC catalyst systems for methanol electro-oxidation. The characterization and performance test results for these catalyst systems are given in the next sections.

4.2.1 Characterization Results

Figure 4-12 shows the FESEM images obtained for SBA15, Fe_2O_3/SBA15, CoO/SBA15, and NiO/SBA15 samples. It can be observed that Fe_2O_3/SBA15, CoO/SBA15, and NiO/SBA-15 samples have similar rope-like morphology like that of the host mesoporous silica template (SBA15). This indicates that the incorporation of Fe_2O_3, CoO, and NiO has not distorted the structure of the host SBA15. It is observed that many strip-like structures with relatively uniform sizes are aggregated into the rope-like macrostructures, which may enhance the overall stability of the samples.

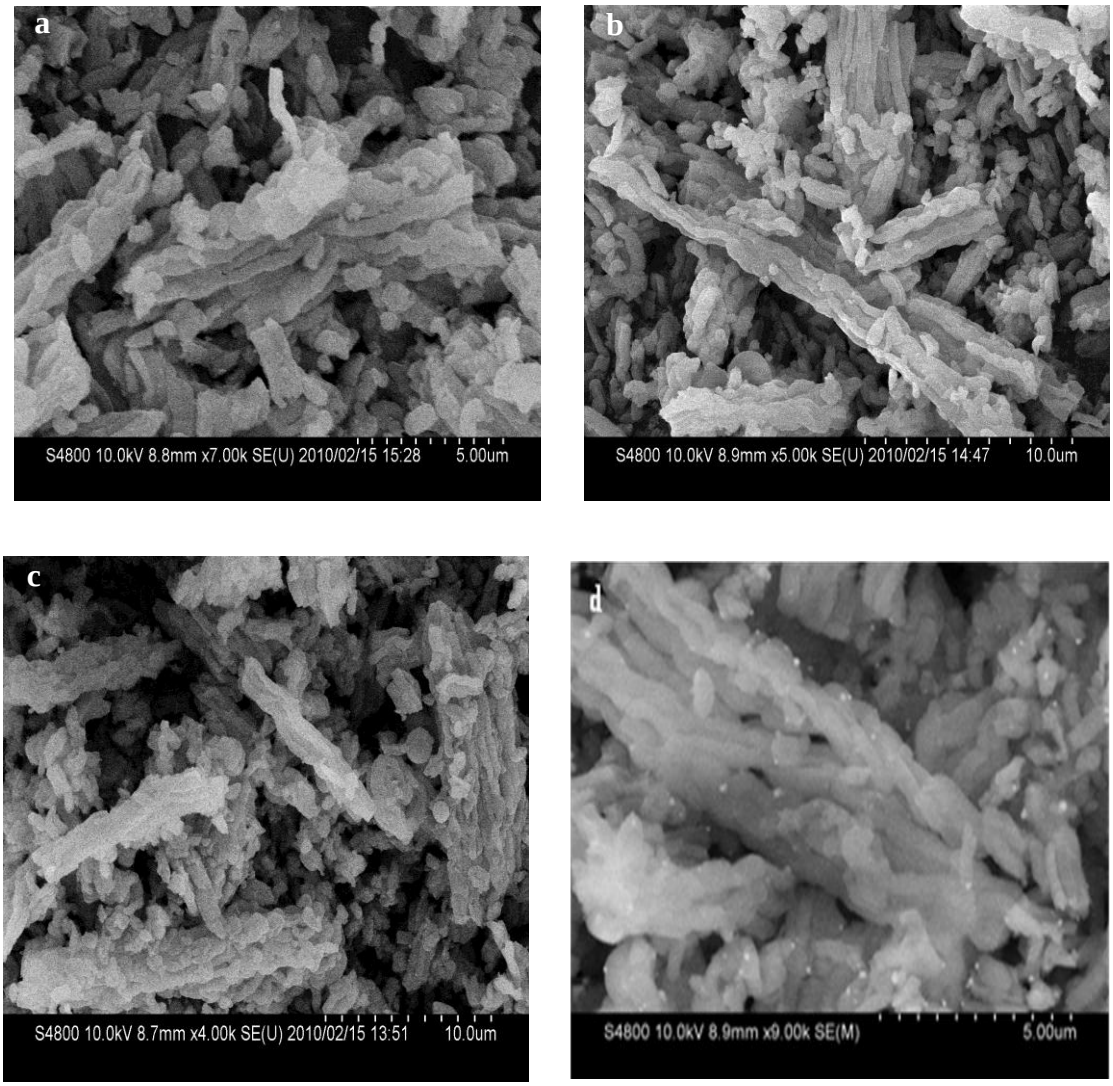

Figure 4-12: FESEM Images of (a) SBA15, (b) Fe_2O_3/SBA15, (c) CoO/SBA15, (d) NiO/SBA15

Low angle powder X-ray diffraction (XRD) patterns for SBA15, Fe_2O_3/SBA15, CoO/SBA15, and NiO/SBA15 samples are shown in Figure 4-13. The obtained XRD patterns for Fe_2O_3/SBA15, CoO/SBA15, and NiO/SBA15 samples are very much similar to that of the host SBA15 sample, which further shows that the structure of the SBA15 is successfully maintained. The XRD patterns for all the samples show three well-resolved diffraction peaks for the 2θ *deg* near 1.0, 1.6, and 1.9, which are characteristics of hexagonally-arranged mesoporous materials. However, a shift towards the lower angle is observed for CoO/SBA15 sample, which suggests less alloying than in the other samples. Similar observation is reported in the literature for calcined Co-SBA15 prepared in acidic medium [126].

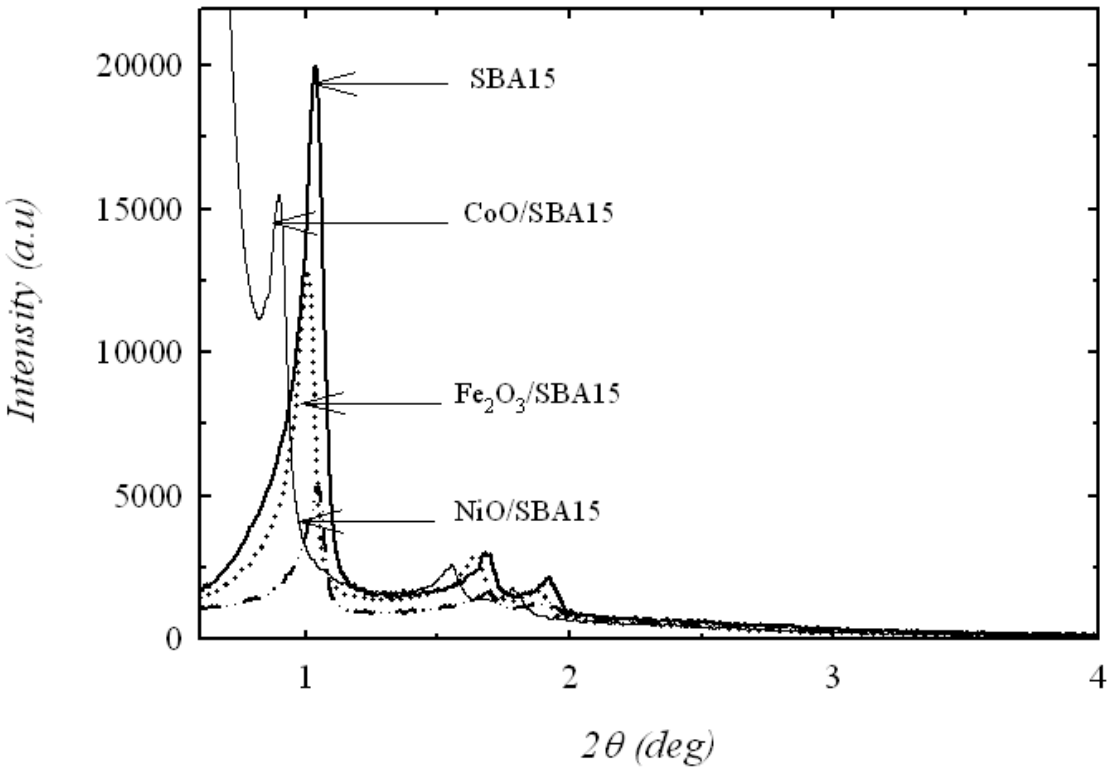

Figure 4-13: Low Angle Powder XRD Patterns for SBA15, Fe_2O_3/SBA15, CoO/SBA15, and NiO/SBA15 Samples

The FT-IR spectra for SBA-15, Fe_2O_3/SBA-15, CoO/SBA-15, and NiO/SBA-15 samples are shown in Figure 4-14. A broad absorption band observed between 1000 – 1250 cm^{-1} is attributed to the presence of silica. It can be observed that this absorption band is widest for the host SBA15 followed by NiO/SBA15 sample, which confirms better alloying in NiO/SBA 15 as also shown by the FESEM images and low angle powder XRD patterns. A sharper peak near 950 cm^{-1} is observed for all the samples compared to the host SBA 15, which suggests presence of more oxygen in the oxides samples.

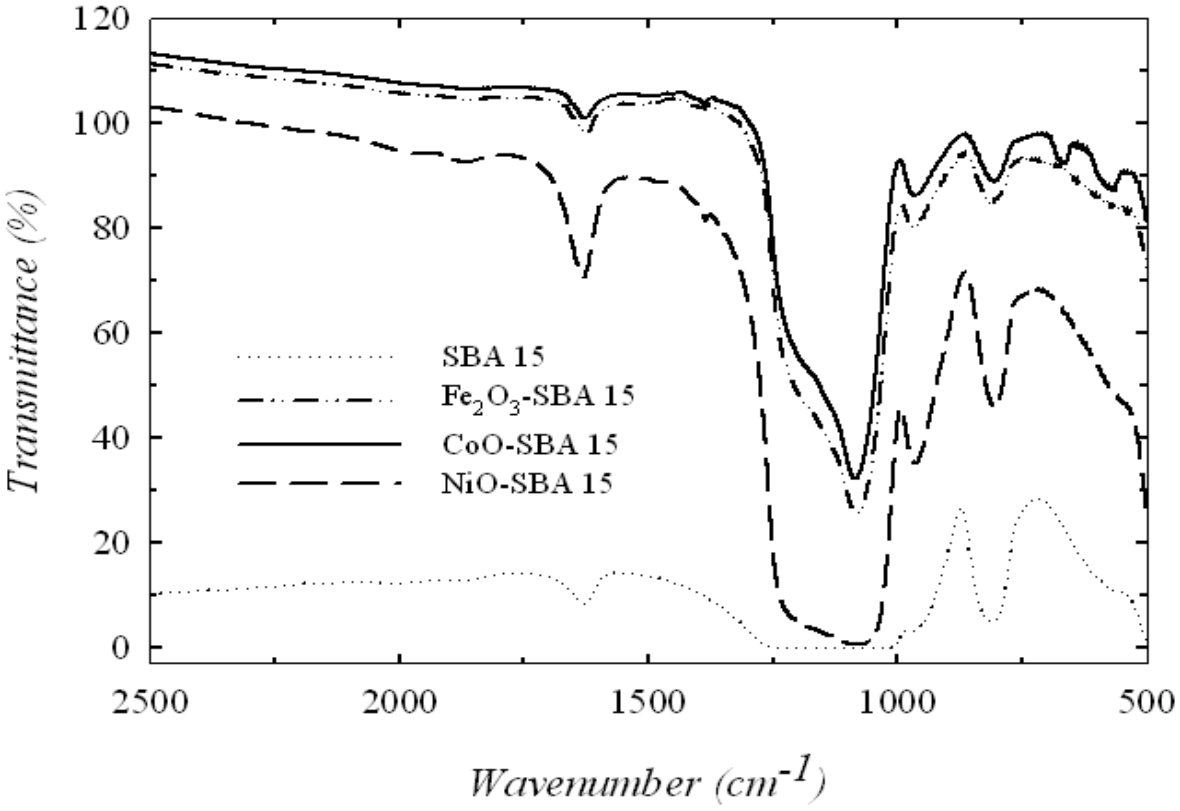

Figure 4-14: FT-IR Spectra for SBA15, Fe_2O_3/SBA15, CoO/SBA15, and NiO/SBA15 Samples

The specific surface area and porosity of Fe_2O_3/SBA-15, CoO/SBA-15, and NiO/SBA-15 samples were measured by N_2 physisorption and the results are shown in Figure 4-15 and Table 4-4. In Figure 4-15a, all the isotherms for the samples show a typical Type 1V model according to the IUPAC classification and have a H1 hysteresis loop at the high pressure side that is representative of mesopores. The shape of the N_2 adsorption-desorption isotherms further confirms that a well ordered mesoporous structure similar to that of the host SBA15 was obtained for all the samples [46]. The sharp inflections between the relative pressures (P/P_0) 0.5 - 0.8 in the isotherms correspond to capillary condensation within the uniform mesopores. The textural parameters such as the specific surface area, pore volume and pore diameters are given in Table 3-4. Pore size distribution derived from desorption branch of the N_2 hysteresis for the samples is shown in Figure 4-15b. The well-known BJH method was used to analyze the desorption branch of the isotherms at relative high pressure to obtain the pore size distribution of Fe_2O_3/SBA-15, CoO/SBA-15, and NiO/SBA-15 samples.

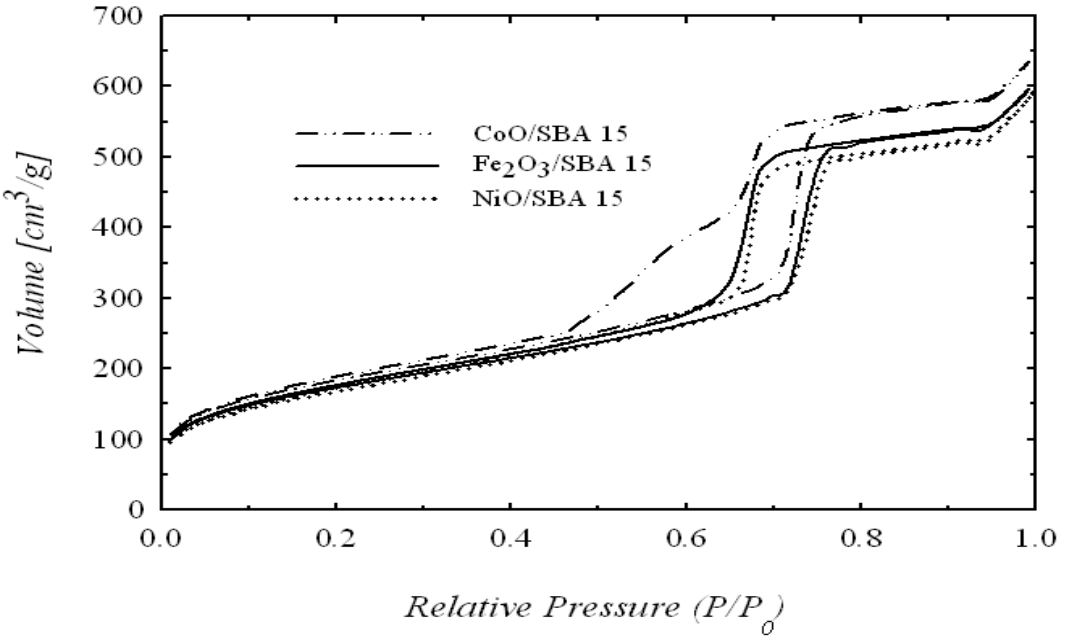

a)

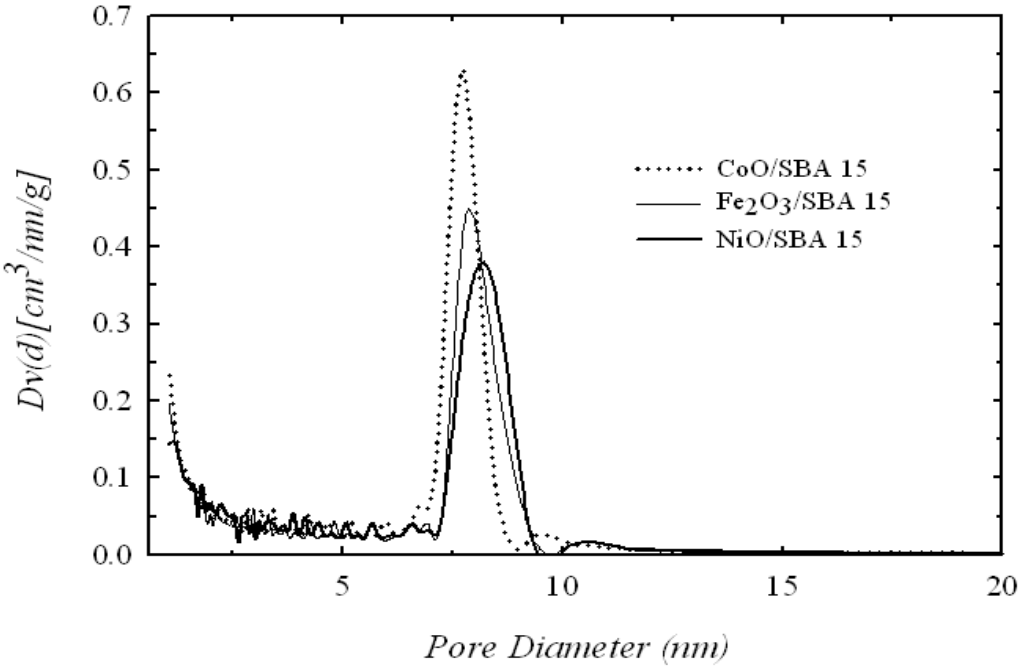

b)

Figure 4-15: (a) N_2 Sorption Isotherms for the Fe_2O_3/SBA15, CoO/SBA15, and NiO/SBA15, (b) Pore Size Distribution

Table 4-4: Pore Structure of the Metals Nano-oxides in SBA15

Samples	BET Surface Area ($m^2 g^{-1}$)	Total Pore Volume ($cm^3 g^{-1}$)	Average Pore Diameter (nm)
Fe_2O_3/SBA-15	621	0.84	7.42
CoO/SBA-15	661	0.91	7.38
NiO/SBA-15	606	0.81	7.50

The prepared Fe_2O_3/SBA-15, CoO/SBA-15, and NiO/SBA-15 samples were carbonized and transformed into Fe_2O_3-MC, CoO-MC, and NiO-MC samples as explained in the experimental section. The specific surface area and porosity of the Fe_2O_3-MC, CoO-MC, and NiO-MC samples were measured by N_2 physisorption and the results are shown in Figure 4-16 and Table 4-5. In Figure 4-16a, all the isotherms for the samples show a typical Type 1V model according to the IUPAC classification. The type 1V adsorption isotherm characterizes the existence of mesoporosity in the Fe_2O_3-MC, CoO-MC, and NiO-MC samples, which is expected to play an important role in dispersing the Pt and Ru active species.

Pore size distribution derived from the desorption branch of the N_2 hysteresis for the samples is shown in Figure 4-16b. The well-known BJH method was used to analyze the desorption branch of the isotherms at relative high pressure to obtain the pore size distribution of the Fe_2O_3-MC, CoO-MC, and NiO-MC samples. It can be observed that the desired mesoporosity is maintained in all the samples.

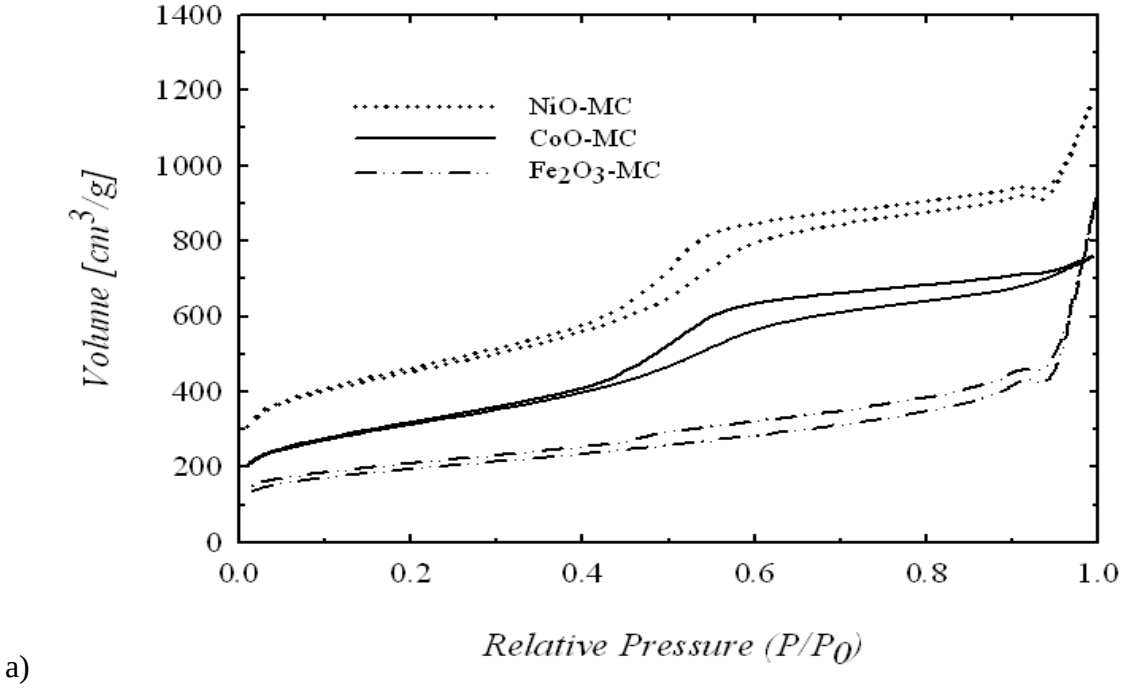

a)

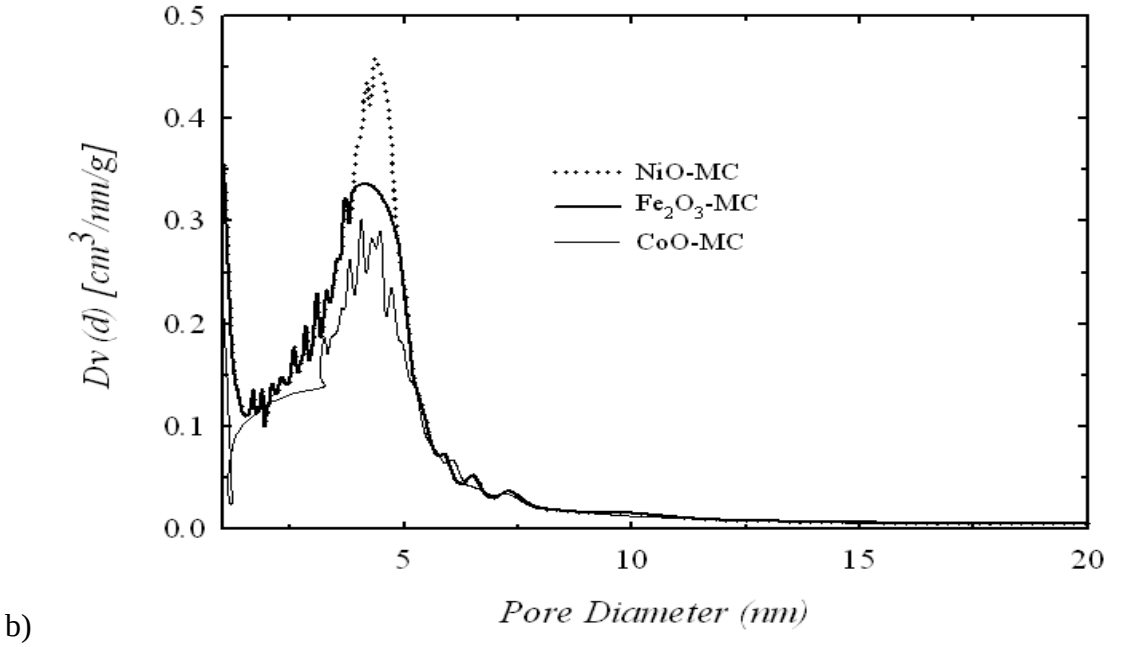

b)

Figure 4-16: (a) N_2 Sorption Isotherms for the Fe2O3-MC, CoO-MC, and NiO-MC Samples, (b) Pore Size Distribution

The textural parameters; specific surface area, pore volume and pore diameters are given in Table 4-5. It can be observed that in all the samples, there is an increase in surface area compared to the parent samples, that is, Fe_2O_3/SBA-15, CoO/SBA-15, and NiO/SBA-15 samples, which is due to the carbonization process. However, significant increase in surface area and pore volume is observed for CoO-MC and NiO-MC samples while a decrease in pore volume was observed for the Fe_2O_3-MC sample. This indicates a possible length shortening for the Fe_2O_3-MC sample during the carbonization process as indicated also by the FESEM images shown in Figure 4-17.

It is obvious from the FESEM images that longer layered structures with relatively uniform sizes, which aggregated into the rope-like macrostructures, are better formed for the NiO-MC sample, which explains why it has the lowest pore diameter, pore volume and highest surface area. In general, it can be seen that mesopores are the dominant pores in all the prepared samples, which is beneficial for the preparation of excellent CH_3OH electro-oxidation catalysts. As reported in the literature, molecules within microporous channels could suffer significantly hindered transport, while molecules in mesoporous channels can approach diffusion rates comparable to those in an open medium [119].

Table 4-5: Pore Structure Properties of the Metals Nano-oxides -Mesoporous Carbon

Sample	BET Surface Area (m^2 g^{-1})	Total Pore Volume (cm^3 g^{-1})	Average Pore Diameter (nm)
Fe_2O_3-MC	687	0.72	4.4
CoO-MC	1114	1.10	3.9
NiO-MC	1589	1.46	3.7

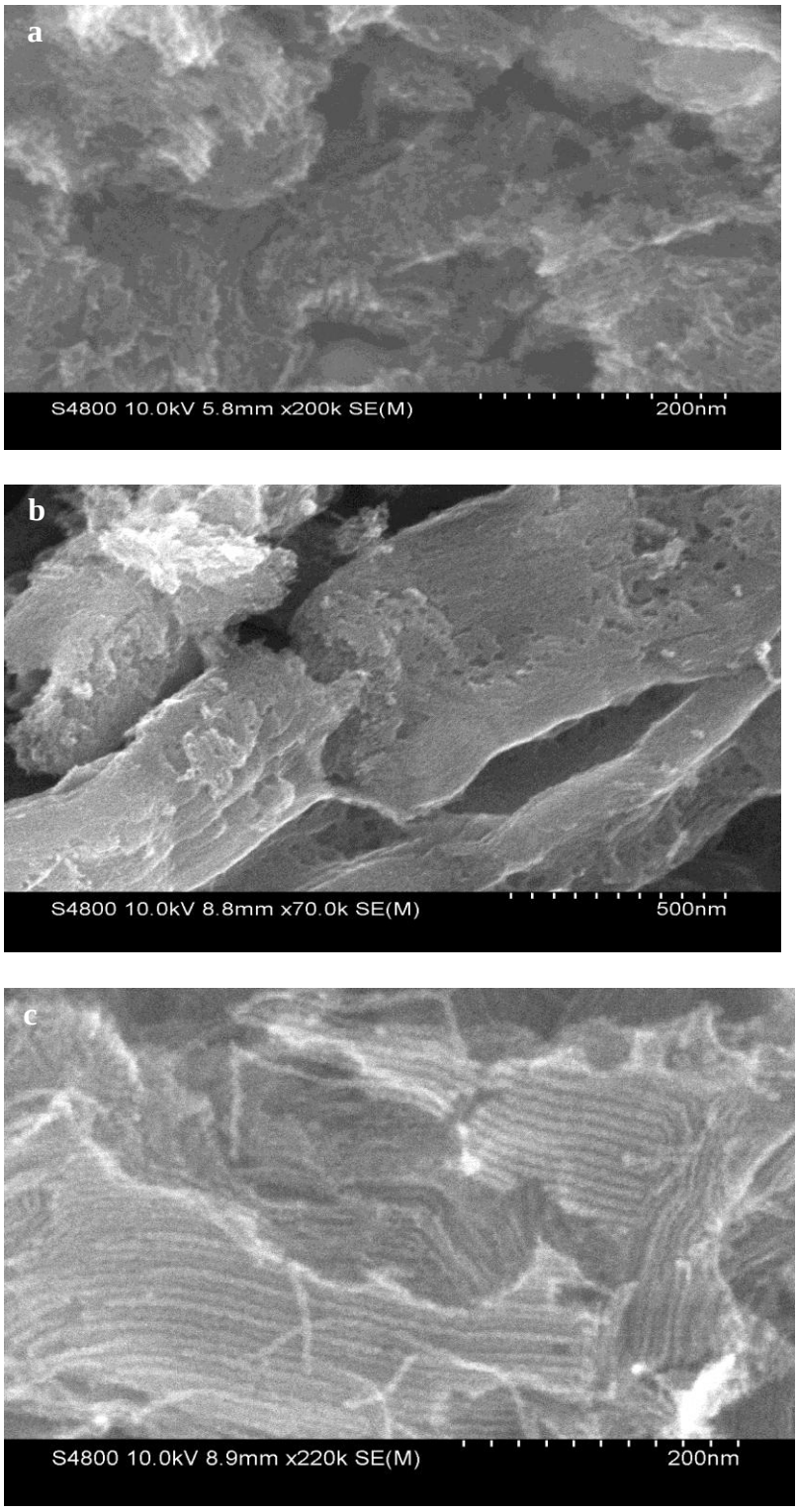

Figure 4-17: FESEM Images of (a) Fe_2O_3-MC, (b) CoO-MC, (c) NiO-MC

The prepared Fe_2O_3-MC, CoO-MC, and NiO-MC samples were then impregnated with Pt and Ru to obtain Pt-Ru/Fe_2O_3-MC, Pt-Ru/CoO-MC, and Pt-Ru/NiO-MC catalyst samples as explained in the experimental section. The catalysts composition is 15 wt% Pt-Ru (1:1 molar ratio), 15 wt% transition metal (Fe, Co, or Ni) and 70 wt% carbon & oxygen. Figure 4-18 shows high angle powder XRD patterns obtained for the prepared catalyst samples. In all the samples, the presence of the face-centred cubic (fcc) structure typical of platinum metal could be inferred from the strong diffractions represented by the crystalline planes (111), (200), and (220), near 2θ of 40.0°, 46.0°, and 68.5° respectively.

Peaks associated with metallic Ru were not observed in all the samples. If the reflection intensities of the Ru metal is low compared with those of the Pt and/or the Ru is present as amorphous compound it will not be detected in the diffractograms.

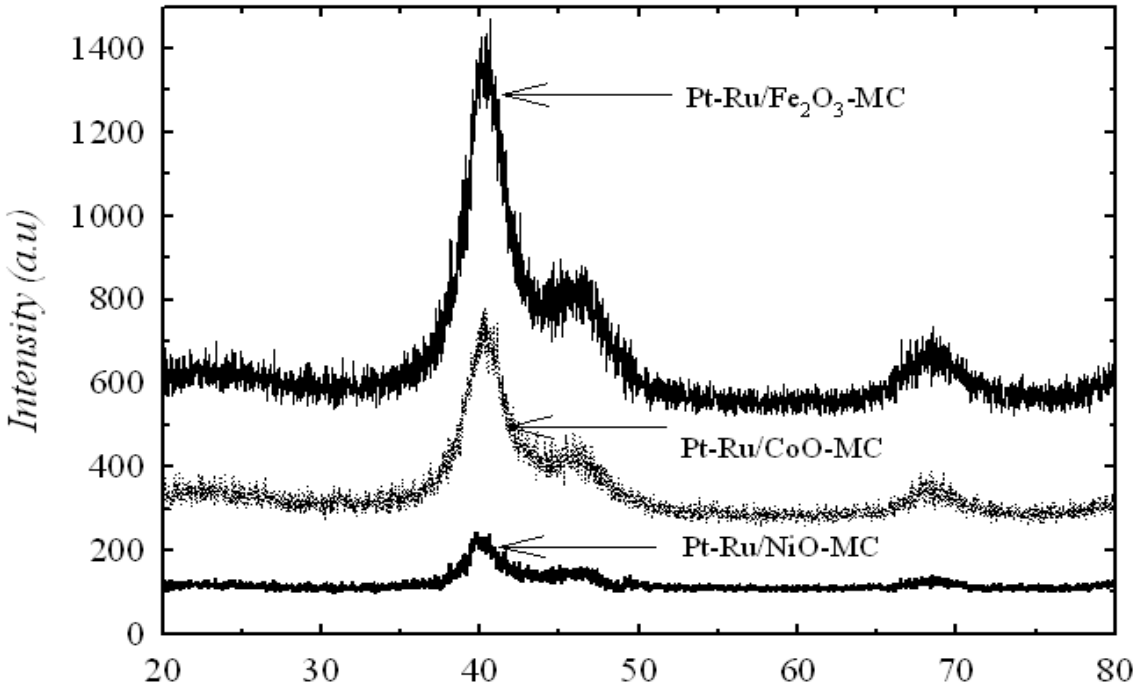

Figure 4-18: High Angle Powder XRD Patterns of the Prepared Catalysts

The XRD pattern did not indicate the presence of metallic Ru, which confirms that Ru is not segregated in a separate phase; it is contained in bimetallic (Pt-Ru) alloy nanoparticles. The Pt-Ru crystal size was calculated using the Debye-Scherrer's equation while d-spacing and lattice parameter were determined using the Bragg's equation and the relationship between d-spacing and lattice parameter for cubic systems respectively [123]. To determine the Pt-Ru crystal size, the (220) reflection was used because even though it is not the strongest, it is completely outside the region of the broad band produced by the carbon support.

Pt-Ru crystal size and lattice parameter for the prepared catalyst samples are given in Table 4-6. From the Table, it can be seen that all the three catalyst samples showed almost the same Pt-Ru crystal size (1.4 - 1.5 nm) with a little variation in lattice parameter values. Appropriate lattice parameter value is beneficial for improving catalyst performance because neither too close inter-particles distance nor scattering of the particles is good for the catalyst performance.

Table 4-6: XRD Data Analysis Results for the Prepared Catalyst Samples

Catalyst Sample	**Peak Position at fcc 220 (*deg*)**	**FWHM (*rad*)**	**Crystal Size (*nm*)**	**d_{hkl} (*Å*)**	**Lattice Parameter (*Å*) (a)**
Pt-Ru/ Fe_2O_3-MC	68.3	0.1100	1.5	1.3722	3.8812
Pt-Ru/CoO-MC	68.2	0.1169	1.4	1.3739	3.8860
Pt-Ru/NiO-MC	68.0	0.1222	1.4	1.3775	3.8962

4.2.2 Performance Test Results

The activity of the prepared catalyst samples for CH_3OH electro-oxidation was measured using the cyclic voltammetry technique. Figure 4-19 shows the CV curves of CH_3OH electro-oxidation activity for the prepared catalyst samples and commercial Pt-Ru/C (E-TEK) measured in N_2 purged 1M H_2SO_4 + 2M CH_3OH solution. The anodic peaks for CH_3OH electro-oxidation are clearly observed for all the catalyst samples between 0.65 – 0.69 V. Highest CH_3OH electro-oxidation peak is observed for the Pt-Ru/NiO-MC. As shown in Table 4-7, all the prepared catalyst samples showed higher activity compared to the commercial Pt-Ru/C (E-TEK). In addition, the catalyst samples showed lower onset potential for CH_3OH electro-oxidation than the commercial Pt-Ru/C (E-TEK). This indicates that NiO, CoO and Fe_2O_3 play a positive role in enhancing the CH_3OH electro-oxidation reaction. Furthermore, incorporating these oxides into the mesoporous carbon during the preparation stage provides large surface area for good dispersion of the Pt and Ru metal species, which leads to better catalyst activity.

Table 4-7: CV Analysis Results for the Prepared Catalyst Samples and E-TEK

Catalyst Sample	Peak Position *V vs. SCE*	Current Density (*mA/cm^{-2}*)	Mass Activity (*mA/mg*)
Pt-Ru/NiO-MC	0.65	55	12.36
Pt-Ru/CoO-MC	0.74	49	11.01
Pt-Ru/ Fe_2O_3-MC	0.69	47	10.56
Pt-Ru/C (E-TEK)	0.66	45	10.11

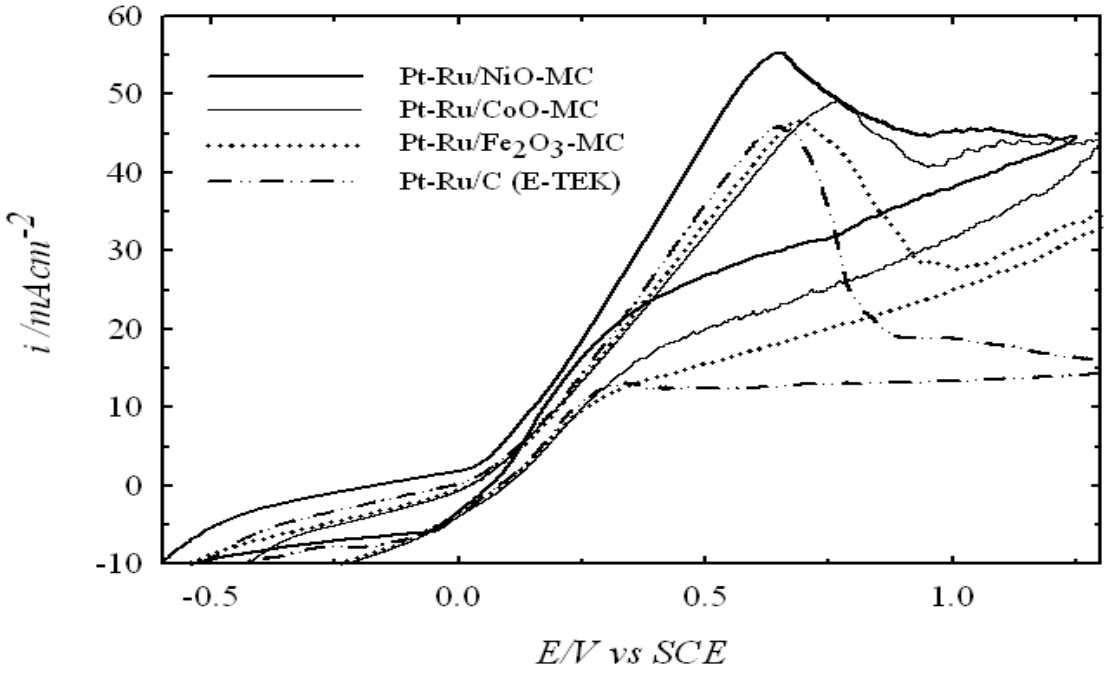

Figure 4-19: CV Curves for the Prepared Catalysts' Activity in 2M CH_3OH + 1M H_2SO_4 at a Scan Rate of 25 mV/s

Apart from the activity test, a preliminary stability test (tolerance to the adsorbed carbon monoxide and other organic intermediate) for the prepared catalyst samples was conducted by doing 20 scans of CV at a scan rate of 25 mVs^{-1} for each of the catalyst sample in order to see their deterioration trend. Figures 4-20 and Figure 4-21 show the 20^{th} scan of the CV curves and the variation in mass activity with time for all the catalyst samples respectively. The catalysts mass activity decreased by 27.3%, 22.4 %, 23.4 % and 24.4 % from its initial value for the Pt-Ru/NiO-MC, Pt-Ru/CoO-MC, Pt-Ru/ Fe_2O_3-MC and commercial Pt-Ru/C (E-TEK) respectively. It is observed that there is a sharp decrease in activity for the Pt-Ru/NiO-MC catalyst sample, which is attributed to its high activity. All the catalyst samples showed a shift towards higher potential for the CH_3OH electro-oxidation during the 20^{th} scan compared with the initial potential during the 1^{st} scan. This means, more potential is required for the CH_3OH electro-oxidation as the catalyst activity decreases.

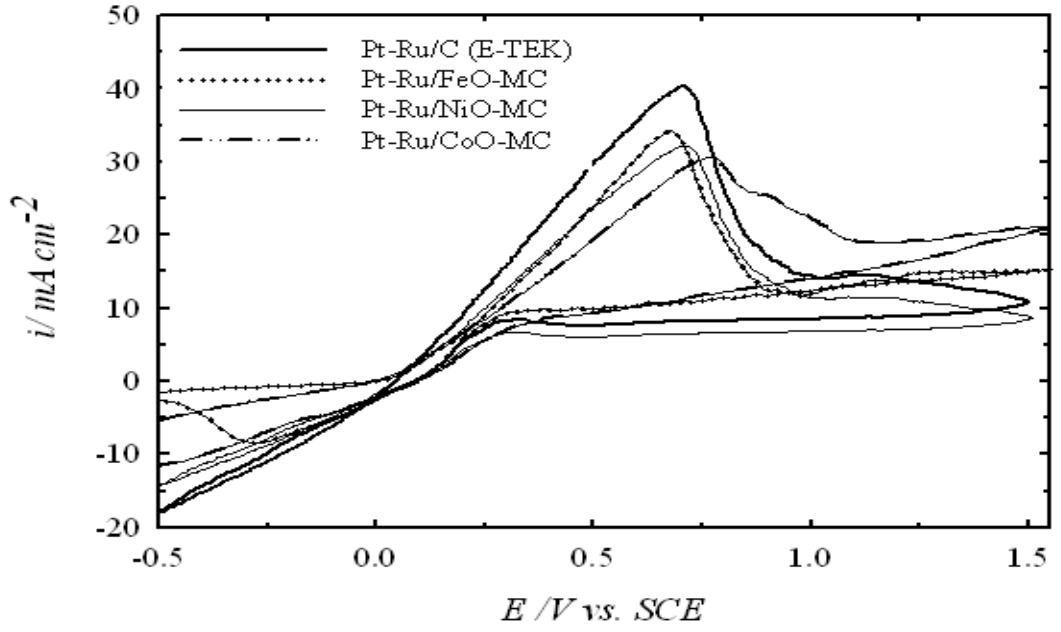

Figure 4-20: CV Curves for Stability Test for all the Prepared Catalysts in 2M CH_3OH + 1M H_2SO_4 at a Scan Rate of 25 mV/s

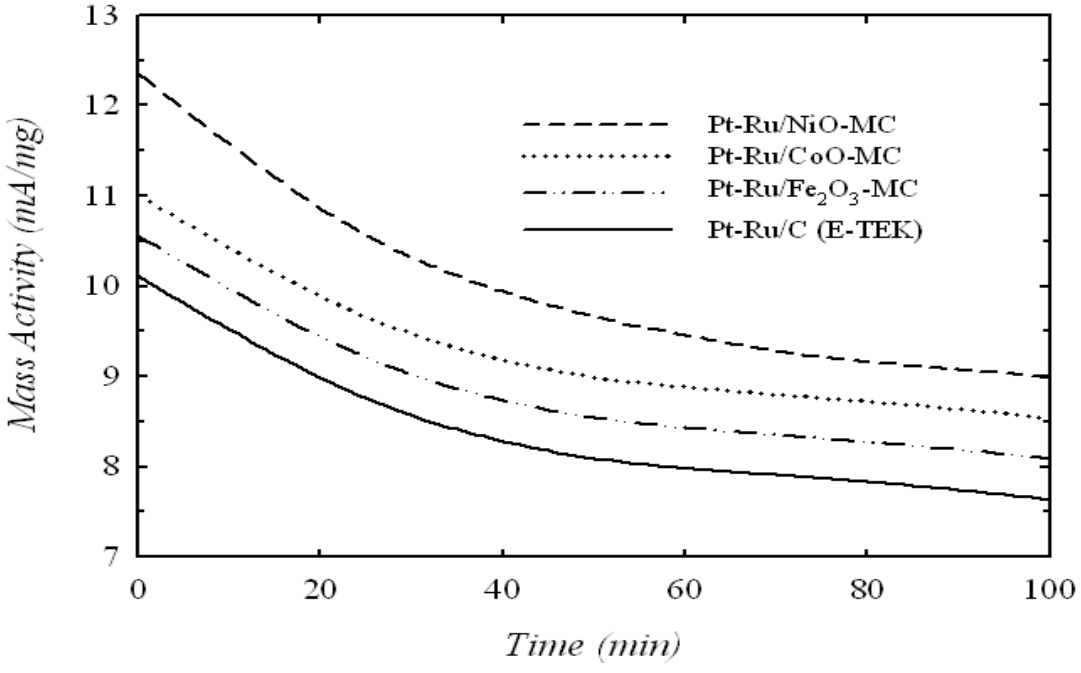

Figure 4-21: Variation of Mass Activity with Time for the Prepared Catalysts

4.3 On non-Ru based Methanol Electro-Oxidation Catalysts

In this third part, characterization and performance evaluation results for Pt/CeO_2-MC, Pt/PrO_2-MC, Pt/NdO_2-MC, and Pt/SmO_2-MC catalysts prepared for methanol electro-oxidation are presented. Among the various catalyst formulations, Pt-Ru alloy has shown the best results for the methanol electro-oxidation. Following a bi-functional mechanism, the Ru-OH species act as a source of atomic oxygen, required for the electro-oxidation of the adsorbed carbon monoxide to carbon dioxide, thus liberating active sites on the surface of the catalyst material near a Pt atom.

However, the use of the noble metals, that is, Pt and Ru contribute to the high cost of the methanol electro-oxidation catalysts, which affects the overall cost of the direct methanol fuel cell. Thus, development of active methanol electro-oxidation catalysts with less amount of Pt and without using Ru is very much desired. In this regard, binary methanol electro-oxidation catalysts such as Pt-CeO_2/C, Pt-Mo/C and PtNi/C have been investigated and reported in the literature as discussed in Chapter 2 (section 2.3.2). In this work, for the first time, the prospect of using rare earth metals: Pr, Nd, and Sm in combination with Pt to prepare low-cost catalyst for methanol electro-oxidation, is revealed. In addition, the traditional Vulcan XC-72 support was not used instead a novel method was used to synthesis mesoporous carbon (MC)-based high surface area nanooxides of CeO_2-MC, PrO_2-MC, NdO_2-MC, and SmO_2-MC. Then the Pt was impregnated to form the desired Pt/CeO_2-MC, Pt/PrO_2-MC, Pt/NdO_2-MC, and Pt/SmO_2-MC catalysts for methanol electro-oxidation. In the next sections, characterization & performance test results for these catalysts are presented.

4.3.1 Characterization Results

Figure 4-22 shows low angle powder X-ray diffraction (XRD) patterns for SBA15, CeO_2/SBA15, PrO_2/SBA15, NdO_2/SBA15 and SmO_2/SBA15 samples. The obtained XRD patterns for CeO_2/SBA15, PrO_2/SBA15, NdO_2/SBA15 and SmO_2/SBA15 samples are very much similar to that of the host SBA15 sample, which indicates that the structure of the SBA15 is successfully maintained [46]. The XRD patterns for all the samples show three well-resolved diffraction peaks for the 2θ *deg* near 1.0, 1.65, and 2.0, which are characteristics of hexagonally-arranged mesoporous materials. However, there is a slight shift towards the higher angle for the PrO_2/SBA15, NdO_2/SBA15, and SmO_2/SBA15 samples unlike the CeO_2/SBA15 sample, which means better alloying for the CeO_2/SBA15 sample. This suggests that there is better synergic interaction between CeO_2 and SBA15, which lead to more homogeneous mixture compared to the other samples.

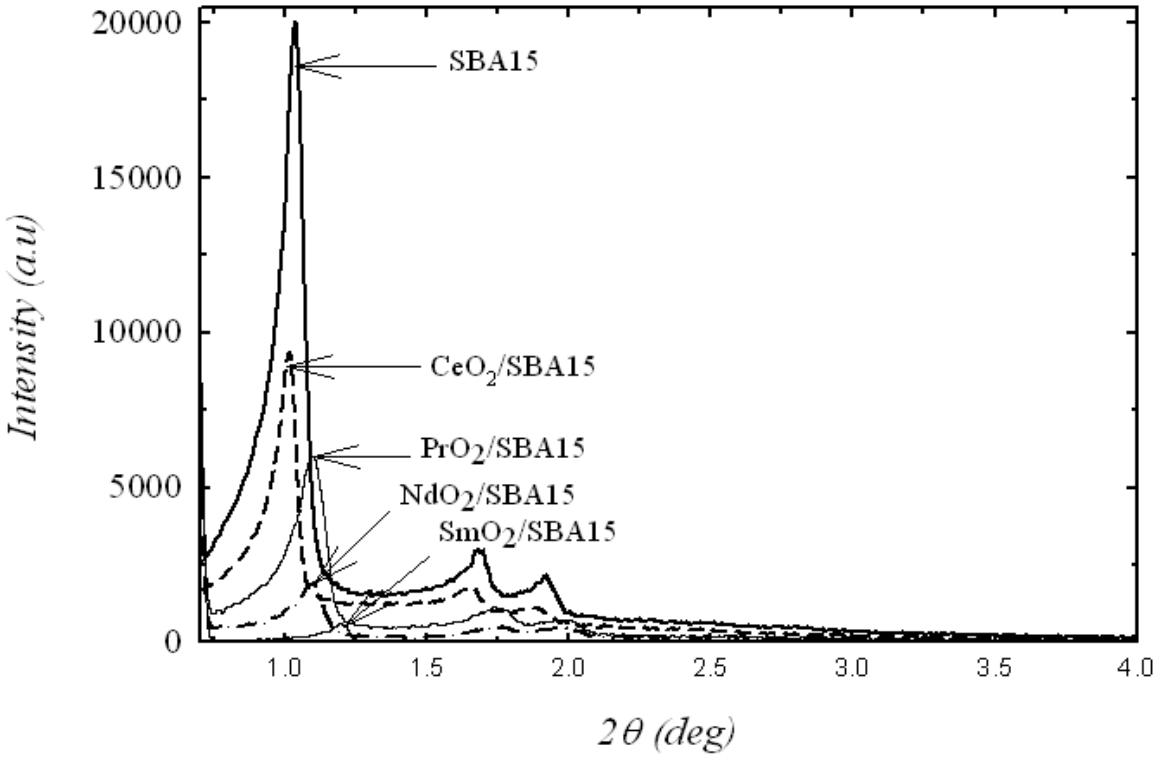

Figure 4-22: Low Angle Powder XRD Patterns for SBA15, CeO_2/SBA15, PrO_2/SBA15, NdO_2/SBA15 and SmO_2/SBA15

Figure 4-23 and Table 4-8 show details of specific surface area and porosity of CeO_2/SBA15, PrO_2/SBA15, NdO_2/SBA15 and SmO_2/SBA15 samples measured by N_2 physisorption. In Figure 4-23a, all the isotherms for the samples show a typical Type 1V model according to the IUPAC classification and have a H1 hysteresis loop at the high pressure side that is representative of mesopores. The type 1V adsorption isotherm characterizes the existence of mesoporosity in CeO_2/SBA15, PrO_2/SBA15, NdO_2/SBA15 and SmO_2/SBA15 samples. The shape of the N_2 adsorption-desorption isotherms further confirms that a well ordered mesoporous structure similar to that of the host SBA-15 was obtained for all the samples [46].

The sharp inflections between the relative pressures (P/P_0) 0.6 - 0.8 in the isotherms correspond to capillary condensation within the uniform mesopores. The sharpness of the inflection step demonstrates the extent of uniform pore size distribution in CeO_2/SBA15, PrO_2/SBA15, NdO_2/SBA15 and SmO_2/SBA15 samples. The textural parameters such as the specific surface area, pore volume and pore diameters are given in Table 4-8.

Figure 4-23b shows the pore size distribution derived from desorption branch of the N_2 hysteresis for the samples. The well-known BJH method was used to analyze the desorption branch of the isotherms at relative high pressure to obtain the pore size distribution of CeO_2/SBA15, PrO_2/SBA15, NdO_2/SBA15 and SmO_2/SBA15 samples.

Table 4-8: Pore Structure Properties of the Metals Nano-oxides in SBA15

Sample	BET Surface Area ($m^2 g^{-1}$)	Total Pore Volume ($cm^3 g^{-1}$)	Average Pore Diameter (nm)
CeO_2/SBA15	571	0.91	7.6
PrO_2/SBA-15	504	0.71	7.7
NdO_2/SBA-15	490	0.69	7.8
SmO_2/SBA-15	526	0.75	7.7

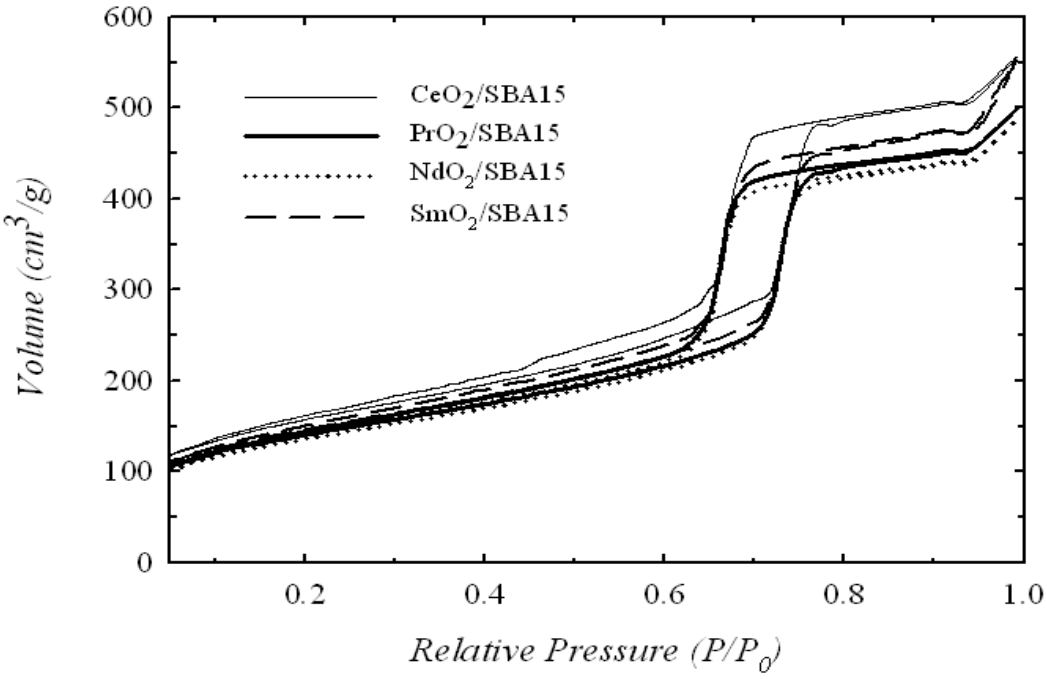

a)

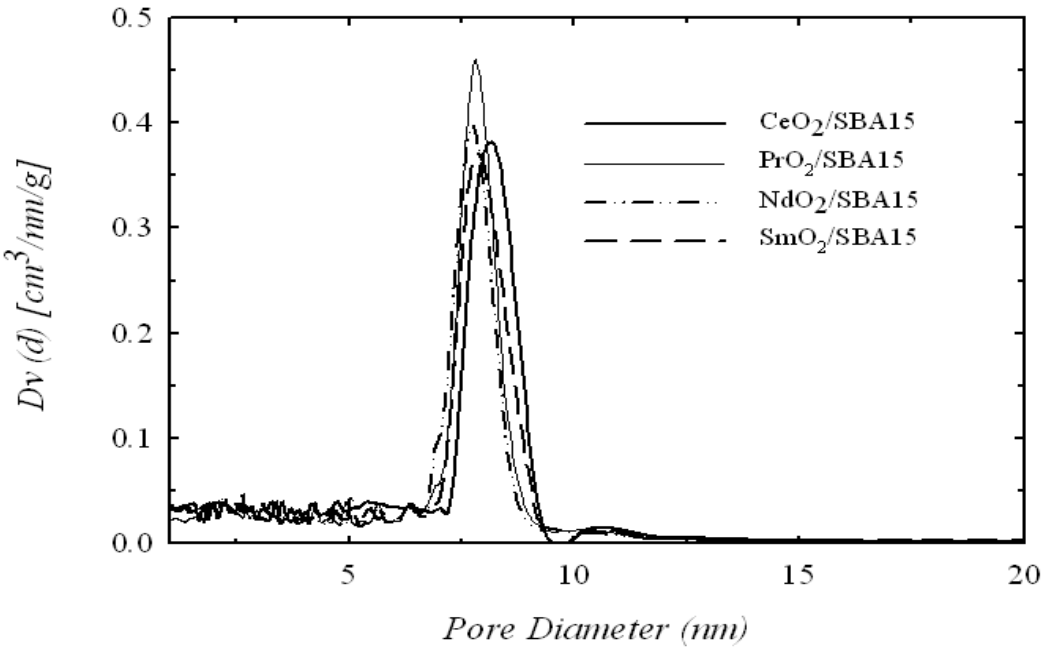

b)

Figure 4-23: (a) N_2 Sorption Isotherms for the CeO_2/SBA15, PrO_2/SBA15, NdO_2/SBA15 and SmO_2/SBA15, (b) Pore Size Distribution

The prepared CeO_2/SBA15, PrO_2/SBA15, NdO_2/SBA15 and SmO_2/SBA15 samples were carbonized and transformed into CeO_2-MC, PrO_2-MC, NdO_2-MC and SmO_2-MC samples as explained in the experimental section. The specific surface area and porosity of the CeO_2-MC, PrO_2-MC, NdO_2-MC and SmO_2-MC samples were measured by N_2 physisorption and the results are shown in Figure 4-24 and Table 4-9. Again, in Figure 4-24a, all the isotherms for the samples show a typical Type 1V model.

Pore size distribution derived from the desorption branch of the N_2 hysteresis for the samples is shown in Figure 4-24b. The well-known BJH method was used to analyze the desorption branch of the isotherms at relative high pressure to obtain the pore size distribution of the CeO_2-MC, PrO_2-MC, NdO_2-MC and SmO_2-MC samples. It can be observed that the desired mesoporosity is maintained in all the samples. The textural parameters such as specific surface area, pore volume and pore diameters are given in Table 4-9. It can be seen that in all the samples, there is a significant increase in surface area and decrease in pore diameter compared to the parent samples, that is, the CeO_2/SBA15, PrO_2/SBA15, NdO_2/SBA15 and SmO_2/SBA15 samples, which is due to the carbonization process.

The increase in surface area is expected to play a key role in forming excellent catalyst samples by providing sufficient space for dispersing the Pt particles. In addition, it can be seen that mesopores are the dominant pores in all the prepared catalyst samples, which is beneficial for the preparation of excellent methanol electro-oxidation catalysts.

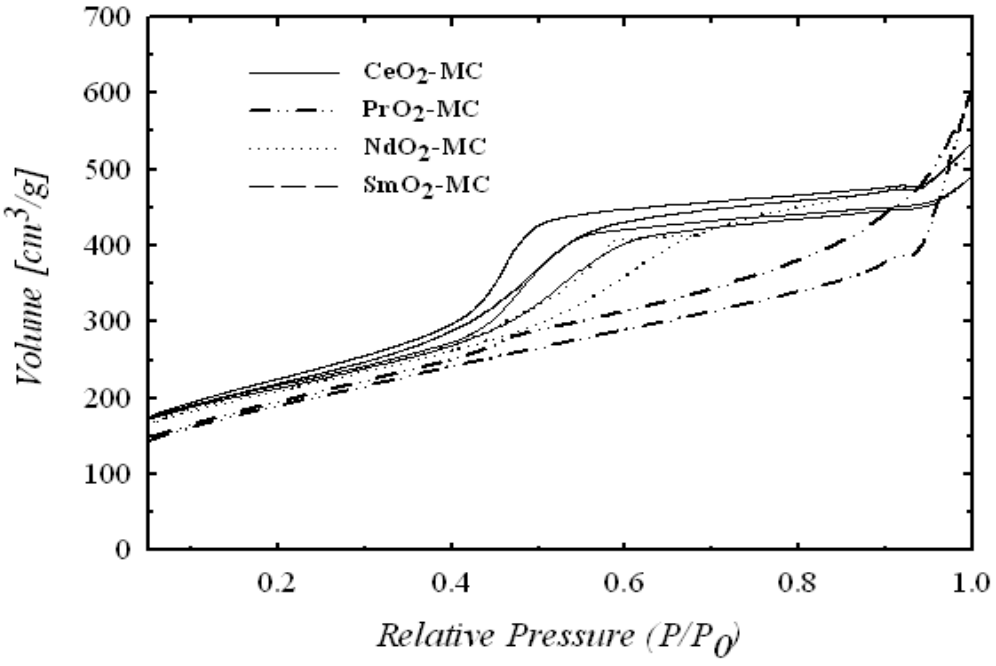

a)

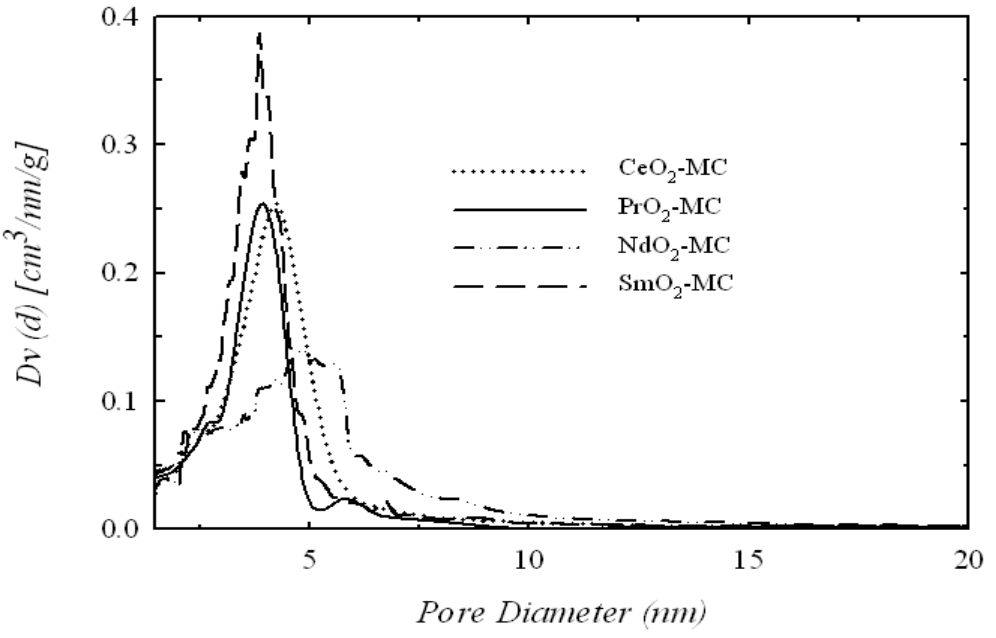

b)

Figure 4-24: (a) N_2 Sorption Isotherms for the CeO_2-MC, PrO_2-MC, NdO_2-MC and SmO_2-MC, (b) Pore Size Distribution

Table 4-9: Pore Structure Properties of the Metals Nano-oxides in Mesoporous Carbon

Sample	BET Surface Area ($m^2\ g^{-1}$)	Total Pore Volume ($cm^3\ g^{-1}$)	Average Pore Diameter (nm)
CeO_2-MC	732	0.72	3.9
PrO_2-MC	684	0.65	4.0
NdO_2-MC	742	0.73	3.8
SmO_2-MC	778	0.75	3.8

The prepared CeO_2-MC, PrO_2-MC, NdO_2-MC and SmO_2-MC samples were then impregnated with Pt to obtain the Pt/CeO_2-MC, Pt/PrO_2-MC, Pt/NdO_2-MC and Pt/SmO_2-MC catalyst samples as explained in the experimental section. Energy dispersive spectroscopy (EDS) was used to determine the elemental composition of the prepared catalyst samples and the corresponding results are shown in Figure 4-25 and Table 4-10. From the Figure, it can be observed that in all the catalyst samples, Pt appear as one of the major elements, which confirm that the prepared CeO_2-MC, PrO_2-MC, NdO_2-MC and SmO_2-MC samples were successfully impregnated with Pt particles.

However, 15 wt% Pt, Ce, Pr, Nd, and Sm each was used in the preparation of the catalyst samples but based on the EDS results shown in Table 4-10, it can be observed that the Pt amount ranges between 12.36 - 13.92 wt% while that of the Ce, Pr, Nd, and Sm ranges between 10.29 – 12.37 wt%. The range is within an acceptable limit since the EDS measures the bulk composition.

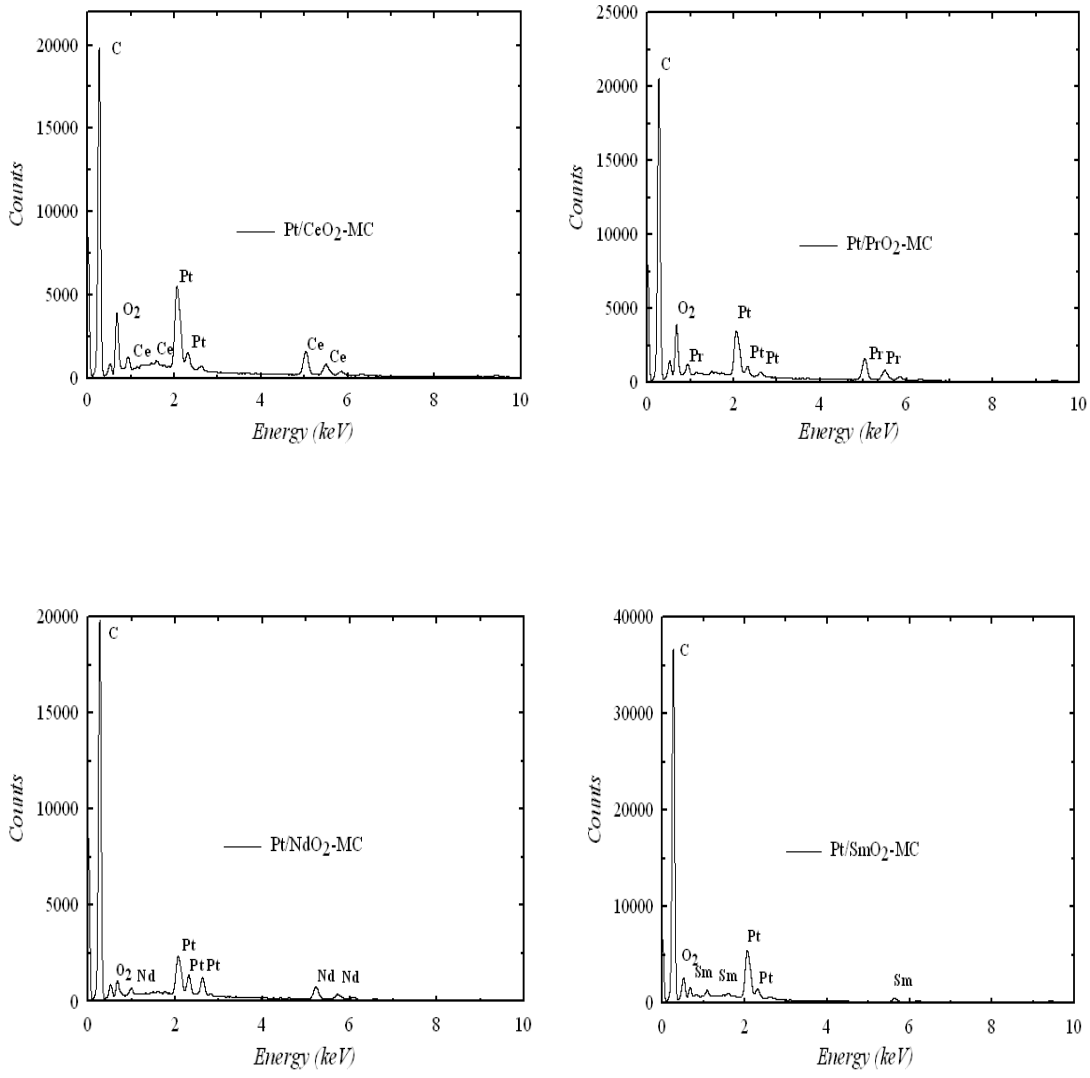

Figure 4-25: EDS Patterns of the Prepared Catalysts

Table 4-10: Elemental Composition of the Prepared Catalysts from the EDS Results

Catalyst	Element	Weight %	Atomic %
Pt/CeO_2-MC	Pt	13.92	2.10
	Ce	11.05	1.85
	O_2	8.76	8.80
	C	66.27	88.25
Pt/PrO_2-MC	Pt	13.85	1.23
	Pr	12.37	2.10
	O_2	7.42	8.04
	C	66.36	88.63
Pt/NdO_2-MC	Pt	12.94	1.16
	Nd	10.29	3.91
	O_2	6.20	6.15
	C	70.57	88.78
Pt/SmO_2-MC	Pt	12.36	0.99
	Sm	10.63	1.15
	O_2	6.51	6.34
	C	70.50	91.52

Figure 4-26 shows the high angle powder XRD patterns obtained for the prepared catalyst samples. In all the samples, the presence of the face-centred cubic (fcc) structure typical of platinum metal could be inferred from the strong diffractions represented by the crystalline planes (111), (200), and (220), near 2θ of 40.0°, 46.0°, and 68.5° respectively. The Pt crystal size was calculated using the Debye-Scherrer's equation while the d-spacing and lattice parameter were determined using the Bragg's equation [123].

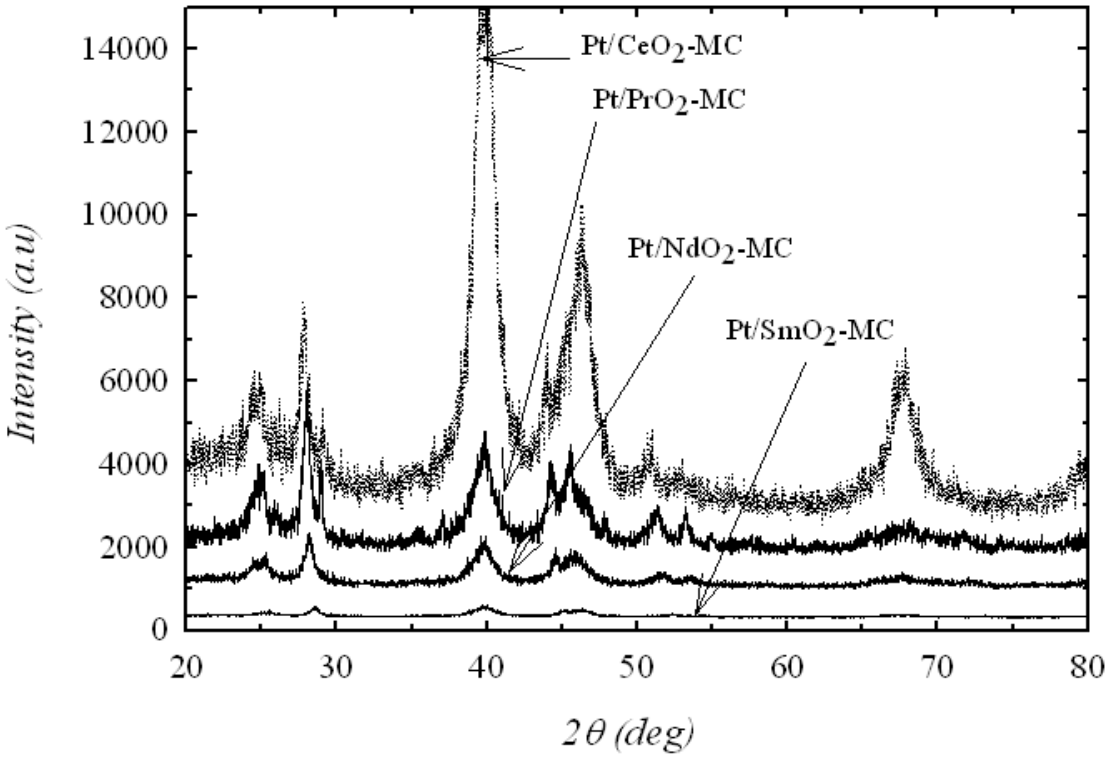

Figure 4-26: High Angle Powder XRD Patterns of the Prepared Catalysts

For the purpose of determining the Pt crystal size, the (220) reflection was used because even though it is not the strongest, it is completely outside the region of the broad band produced by the carbon support, thus there is no overlap. Pt crystal size and lattice parameter for the prepared catalyst samples are given in Table 4-11. From the Table, it can be seen that Pt/SmO_2-MC catalyst sample showed the least Pt crystal size of 1.3 nm and the highest lattice parameter of 3.8911 Å.

Table 4-11: XRD Data Analysis Results for the Prepared Catalysts

Catalyst Sample	Peak Position at fcc 220 (*deg*)	FWHM (*rad*)	Crystal Size (*nm*)	d_{hkl} (*Å*)	Lattice Parameter (*Å*) (a)
Pt/ CeO_2-MC	68.5	0.1222	1.4	1.3686	3.8710
Pt/ PrO_2-MC	68.6	0.1187	1.4	1.3669	3.8662
Pt/ NdO_2-MC	68.3	0.1239	1.4	1.3722	3.8812
Pt/ SmO_2-MC	68.1	0.1257	1.3	1.3757	3.8911

4.3.2 Performance Test Results

Cyclic voltammetry was employed to study the activity of the prepared catalysts for CH_3OH electro-oxidation. Figure 4-27 shows the cyclic voltammogram curves of CH_3OH electro-oxidation activity for the prepared catalyst samples and commercial Pt-Ru/C (E-TEK) measured in deareated 1M H_2SO_4 + 2M CH_3OH solution. The anodic peaks for CH_3OH electro-oxidation are clearly observed for all the catalyst samples between 0.62 – 0.69 V. In addition, similar onset potential is observed for all the catalyst samples.

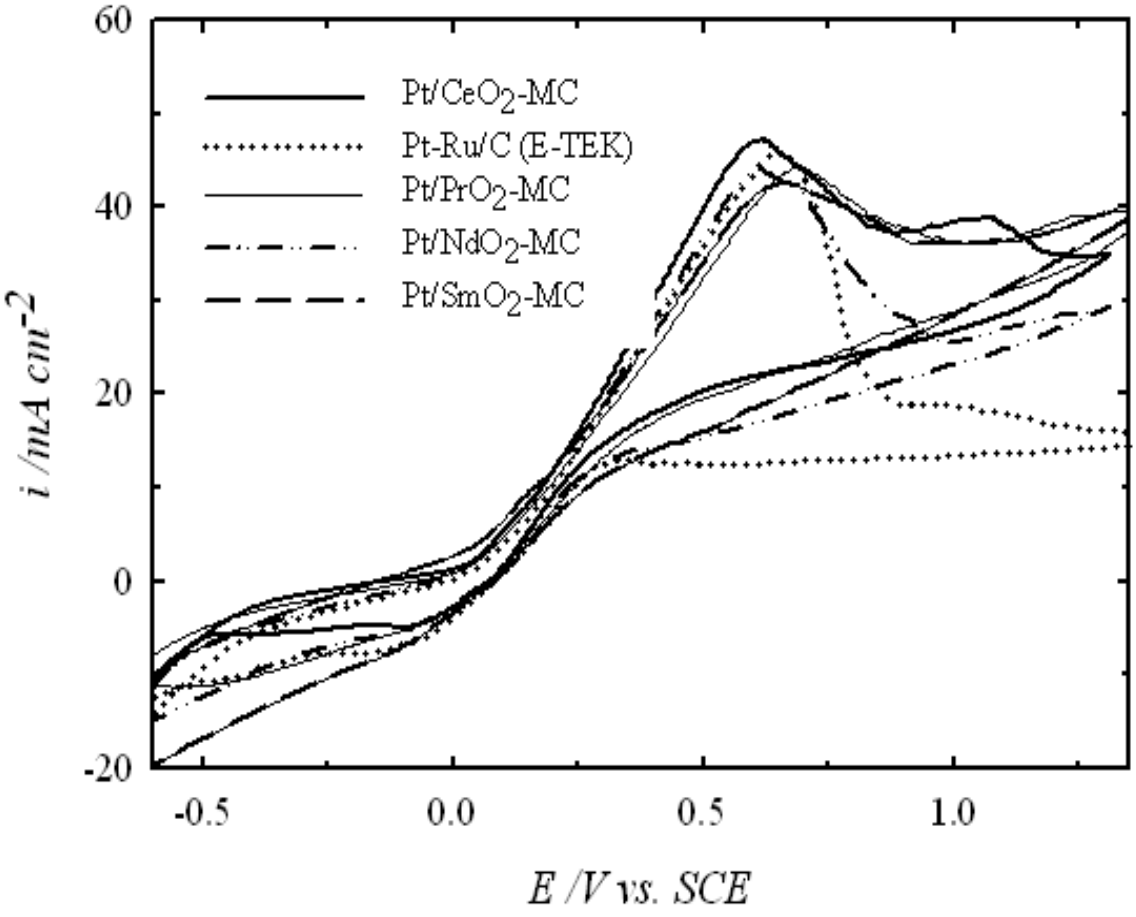

Figure 4-27: CV Curves for the Catalysts' Activity Test in 2M CH_3OH + 1M H_2SO_4 at a Scan Rate of 25 mV/s

As shown in Table 4-12, Pt/CeO_2-MC catalyst sample showed the highest activity for CH_3OH electro-oxidation, which is about 3.5% more than that of the commercial Pt-Ru/C (E-TEK). However, the other prepared catalyst samples showed a slightly lower activity compared to the commercial Pt-Ru/C (E-TEK).

Table 4-12: CV Analysis Results for the Prepared Catalysts and E-TEK

Catalyst Sample	Peak Position *V vs. SCE*	Current Density (*mA/cm^{-2}*)	Mass Activity (*mA/mg*)
Pt/CeO_2-MC	0.62	47	10.56
Pt/PrO_2-MC	0.69	43	9.66
Pt/NdO_2-MC	0.62	42	9.44
Pt/SmO_2-MC	0.66	41	9.21
Pt-Ru/C (E-TEK)	0.66	45	10.11

The reason for the high activity of Pt/CeO_2-MC catalyst sample is due to better synergic interaction between CeO_2 and the support, which has been confirmed from the low angle XRD pattern. In addition, from the EDS results, the highest amount of Pt, which is 13.92 wt% was found in the Pt/CeO_2-MC catalyst sample. This means that it has accommodated more Pt because of better synergy and more amount of platinum translates to better catalyst activity. Furthermore, CeO_2-MC sample has moderate specific surface area of 732 m^2/g while Pt/CeO_2-MC catalyst sample showed Pt crystal size of 1.4 nm and lattice parameter of 3.8710 Å, which could lead to good dispersion. This is unlike the Pt/SmO_2-MC catalyst sample, which showed the least catalytic activity that can be attributed to its lowest Pt crystal size of 1.3 nm,

highest lattice parameter of 3.8911 Å and highest specific surface area of 778 m^2/g for the SmO_2-MC sample that can result in scattering of the Pt particles instead of good dispersion. The mechanism of CO_{ads} electro-oxidation in the presence of CeO_2, PrO_2, NdO_2, or SmO_2 can be tentatively represented as [127]:

$$CeO_2 + H_2O \rightarrow CeO_2 - OH_{ads} + H^+ + e^- \quad (4.4)$$

$$Pt - CO_{ads} + CeO_2 - OH_{ads} \rightarrow Pt + CeO_2 + CO_2 + H^+ + e^- \quad (4.5)$$

The most significant achievement in this work is the fact that expensive Ru was not used and the Pt content in the prepared catalyst samples is 15 wt% only, which is low compared to the 30 - 40 wt% metals (Pt & Ru) content that is normally used in the commercial catalysts. Thus, with reduced noble metals content and relatively high activity, the prepared catalysts have potential for use in CH_3OH electro-oxidation.

A preliminary stability test (tolerance to CO_{ads} and other intermediate organic compounds) was conducted for the Pt/CeO_2-MC catalyst sample, as shown in Figure 4-28. A gradual decay in current density with time is observed, especially after the 5^{th} scan. This is an indication of good tolerance or removal of CO_{ads} and other intermediates compounds that normally poison the catalyst. The preliminary stability test was also conducted for all the prepared catalyst samples and the commercial Pt-Ru/C (E-TEK) catalyst by doing 20 scans of CV at a scan rate of 25 mVs^{-1} in order to see their deterioration trend.

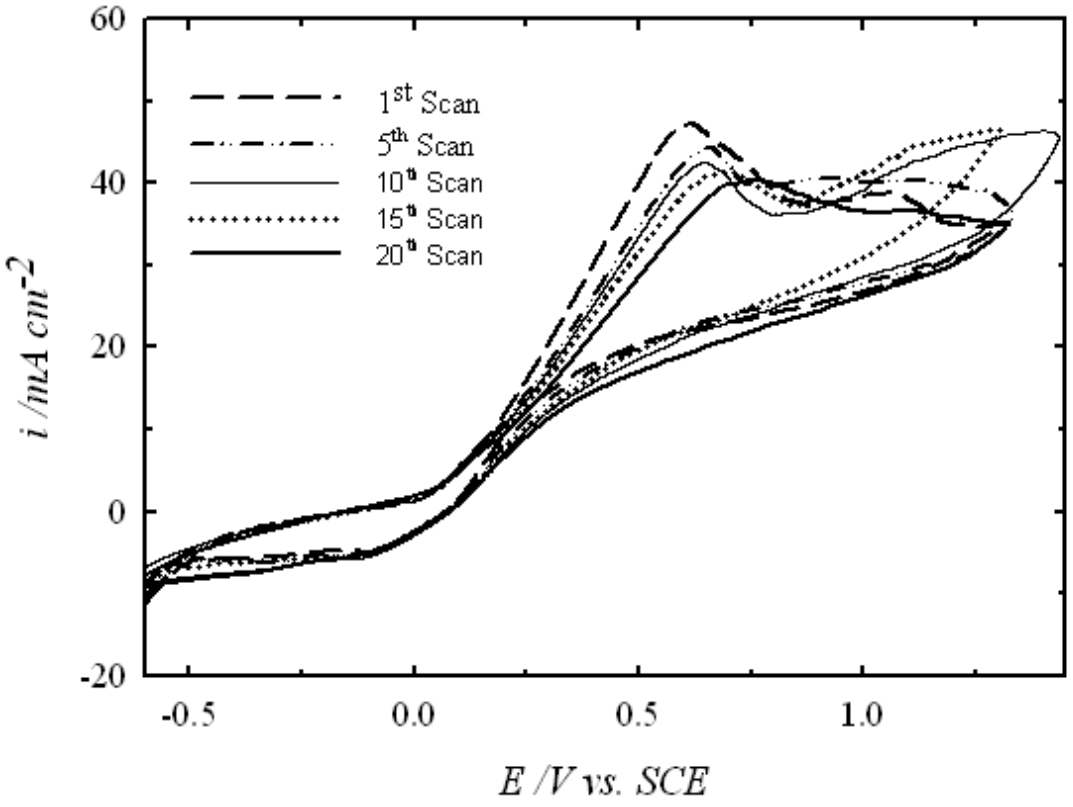

Figure 4-28: CV Curves for the Pt/CeO_2-MC Catalyst Stability Test in 2M CH_3OH + 1M H_2SO_4 at a Scan Rate of 25 mV/s

Figures 4-29 and 4-30 show the 20^{th} scan of the CV curves and variation of mass activity with time for all the catalyst samples, respectively. All the catalyst samples showed a shift towards higher potential for the CH_3OH electro-oxidation during the 20^{th} scan compared with the initial potential during the 1^{st} scan. This means, more potential is required for the CH_3OH electro-oxidation as the catalyst activity decreases. The catalysts mass activity decreased by 19.1 %, 23.2 %, 23.8 %, 24.4 % and 26.8 % from its initial value for the Pt/CeO_2-MC, Pt/PrO_2-MC, Pt/NdO_2-MC, commercial Pt-Ru/C (E-TEK) and Pt/SmO_2-MC respectively. In general, a gradual decay in mass activity with time is observed for all the catalyst samples. Despite the fact that the prepared catalysts do not contain Ru and have less Pt content (which means cheaper) but they showed reasonable activity and stability. Thus, they have great potential for use as the anode catalyst of direct methanol fuel cell.

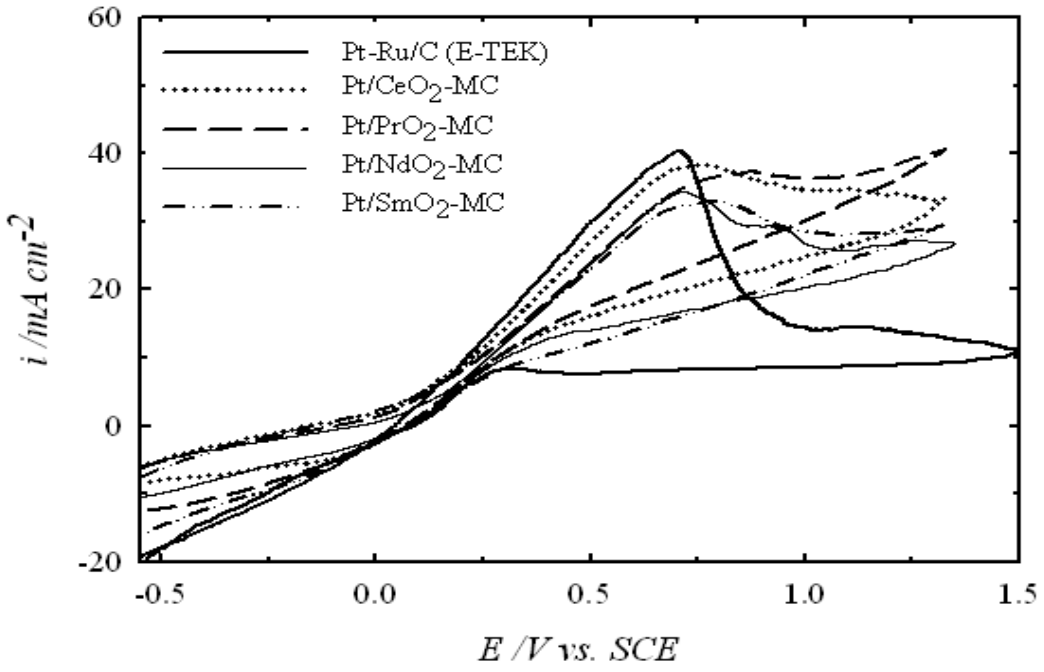

Figure 4-29: CV Curves for all the Prepared Catalysts Stability Test in 2M CH_3OH + 1M H_2SO_4 at a Scan Rate of 25 mV/s

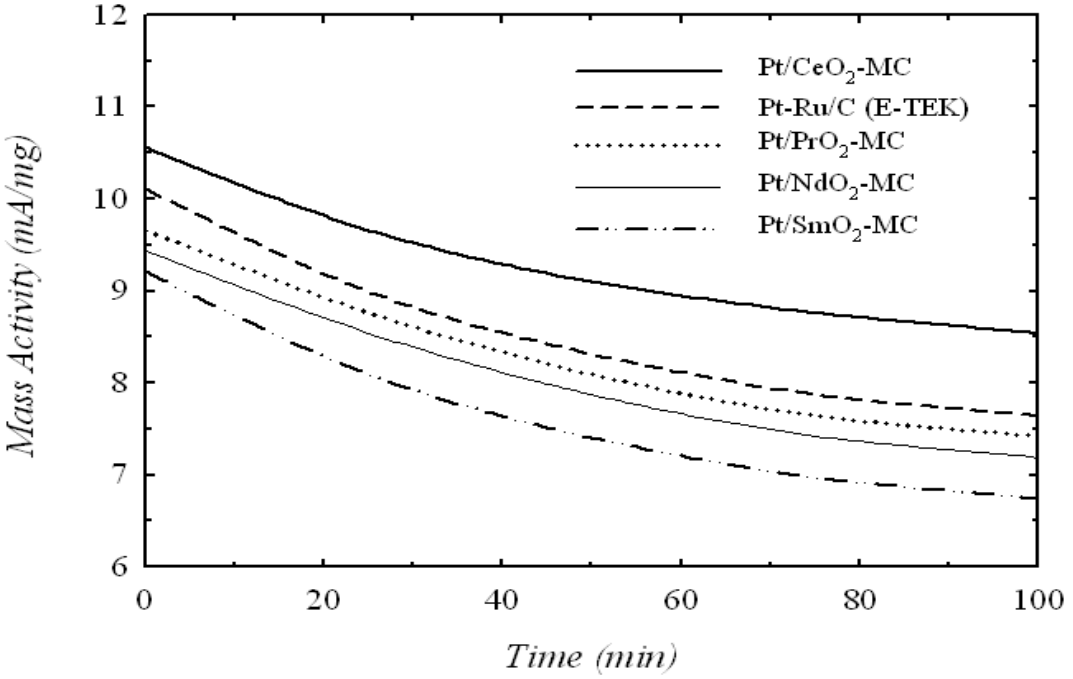

Figure 4-30: Variation in Mass Activity with Time for the Prepared Catalysts

4.4 Performance of Catalysts for DMFC

Based on the cyclic voltammetry results, six (6) catalyst samples prepared using different support materials were selected because of their superior activity and reasonable stability. The selected catalysts samples were then used to fabricate membrane electrode assemblies (MEAs) as explained section 3.7 (Chapter 3). The MEA samples are labeled B1-B6 and contain:

- B1: Pt-Ru/MCN-150, Pt/C, GDLs on Nafion® 117 Membrane
- B2: Pt-Ru/MCN-130, Pt/C, GDLs on Nafion® 117 Membrane
- B3: Pt-Ru/MCN-100, Pt/C, GDLs on Nafion® 117 Membrane
- B4: Pt-Ru/F-MWCNTs, Pt/C, GDLs on Nafion® 117 Membrane
- B5: Pt-Ru/Vulcan-XC, Pt/C, GDLs on Nafion® 117 Membrane
- B6: Pt-Ru/C (E-TEK) , Pt/C, GDLs on Nafion® 117 Membrane

Figures 4-31 show a representative picture of one of the fabricated MEAs. The MEAs were tested in ARBIN Fuel Cell Test Station. The test conditions are:

- Cell Temperature: 70°C & 80 °C
- Cell Pressure: Atmospheric
- Methanol Concentration: 2M
- Methanol flow rate: 2 ml/min
- Oxygen flow rate: 160 ml/min)
- Air Humidification Temperature: 80 °C
- Applied Voltage: 0 to 1

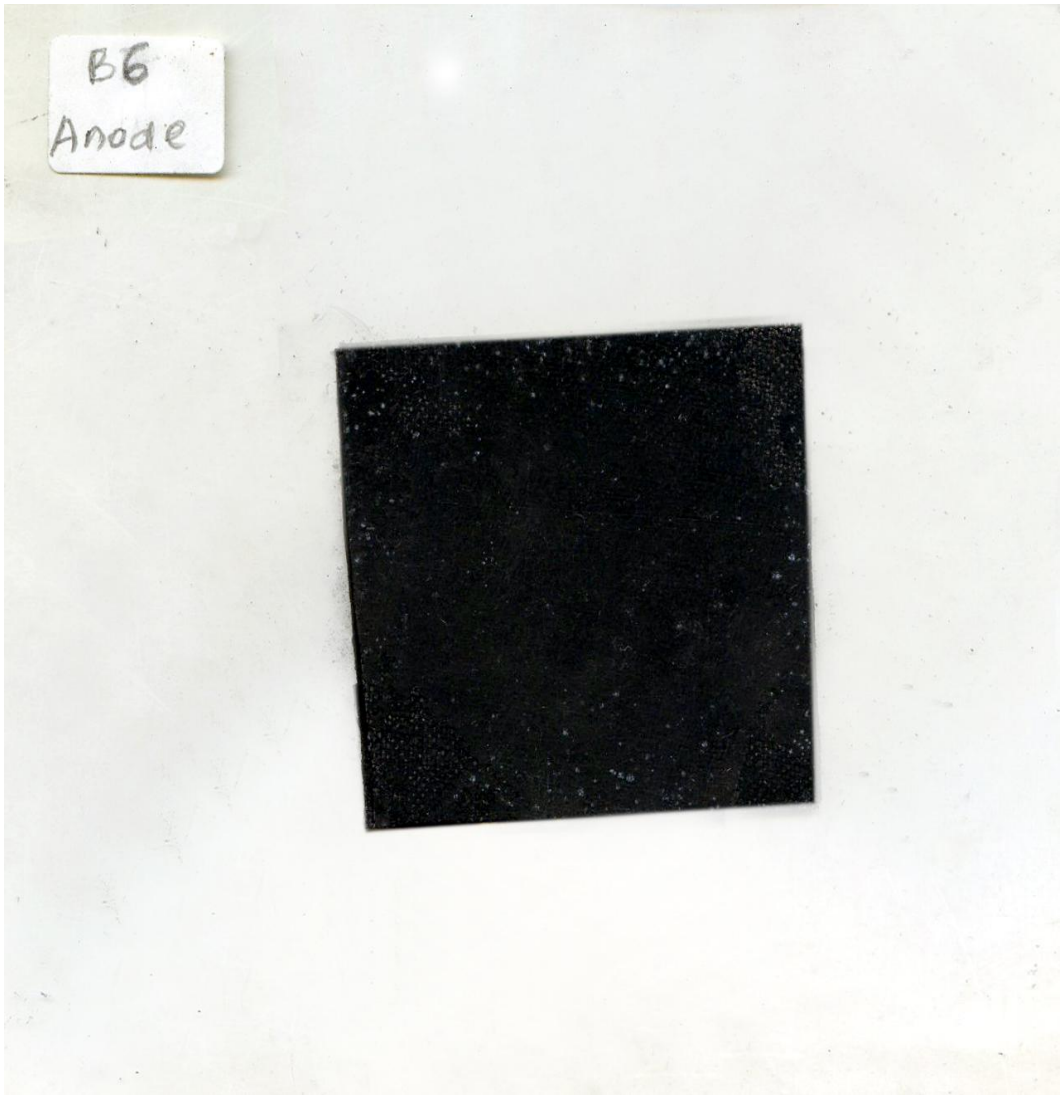

Figure 4-31: MEA Sample B6

As shown in Table 4-13, the Pt-Ru/MCN-150 showed the highest power density, which is consistent with the screening results. As mentioned earlier, this is attributed to the suitable surface area and pore diameter of the MCN-150 support material of about 600 m^2/g and 6.4 nm respectively. In addition, among the catalysts samples, Pt-Ru/MCN-150 catalysts showed moderate PtRu crystal size and lattice parameter of 2.1 nm and 3.8812 Å, respectively. This results in excellent dispersion of the active metal species (Pt-Ru). It is mostly agreed that the catalytic activity is strongly dependent on the shape, size and distribution of the active metal (s) particles. Thus, the extent of dispersion of the Pt particles in the catalysts significantly affects the performance of the catalysts. However, Pt-Ru/Vulcan XC-72 prepared in our laboratory showed the lowest power density, which is suggested to be due to the inferiority of the Vulcan carbon support compared to both the multi-walled carbon nanotubes and the mesoporous carbon materials.

Table 4-13: Power Density for the Fabricated MEAs

Sample	Power Density mW/cm^2	
	70 ^oC	**80 ^oC**
MEA 1 : Pt-Ru/MCN-150	41.4	56.3
MEA 2 : Pt-Ru/MCN-130	37.8	43.49
MEA 3 : Pt-Ru/MCN-100	38.0	53.8
MEA 4 : Pt-Ru/F-MWCNTs	24.97	29.3
MEA 5 : Pt-Ru/Vulcan XC -72	21.0	23.0
MEA 6 : Pt-Ru/C (Commercial)	21.9	23.59

Figures 4-32 to 4-43 show polarization curves (which are all similar) for the various MEAs including the maximum power density. In most of the experimental and theoretical studies on fuel cells, the polarization of the anode has been considered negligible unless the operating current density is high enough so that mass transport polarization effects arise on the anode. Comparing the Figures with a typical polarization curve (Figure 2-6, Chapter 2), it is evident that the methanol electro-oxidation reaction using the prepared MEAs is not limited by mass transport rather it is limited by reaction rate and ohmic resistance. This implies that there is still room for improvement on the prepared catalyst systems for enhanced anode kinetics. When the mass transport rate of the system is much faster than the rate of the dissociative adsorption reaction, the difference between the concentration of CH_3OH in the anode catalyst layer and the CH_3OH in the bulk solution will be very small and diffusion (external transport resistance) limitation will have negligible effect on the overall reaction rate. In comparison, when the mass transport rate is low, the diffusion of CH_3OH molecules will play a significant role on the reaction rate.

In general, operating the DMFC at the maximum power condition decreases its efficiency. Thus, in practice normally an optimum condition is used that will generate reasonable power with good efficiency.

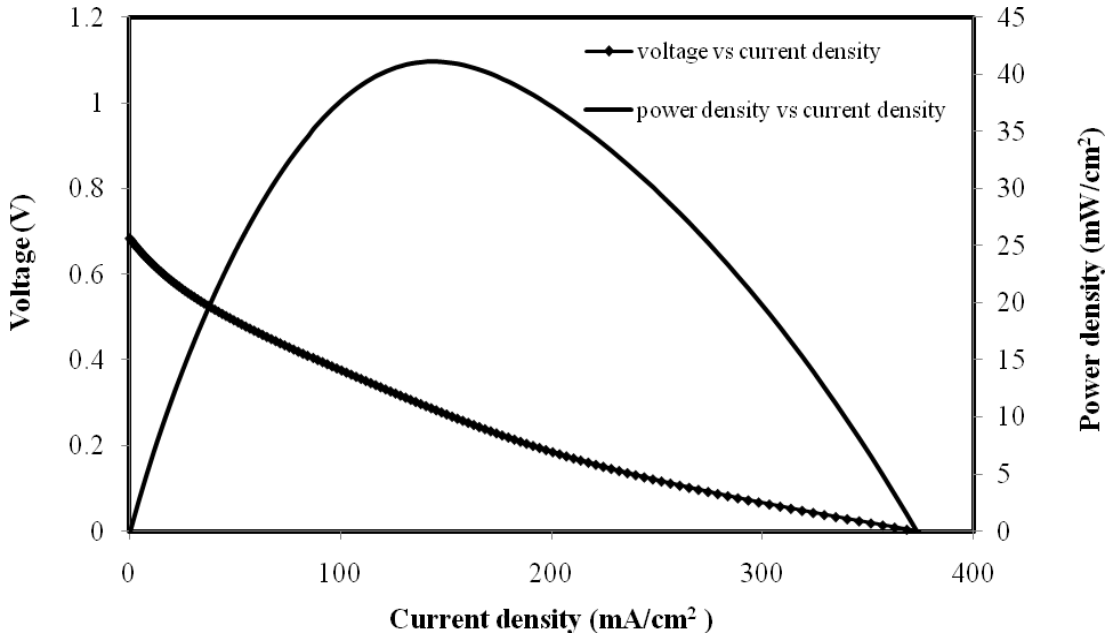

Figure 4-32: Polarization Curve at 70 ^{o}C for the MEA Sample B1

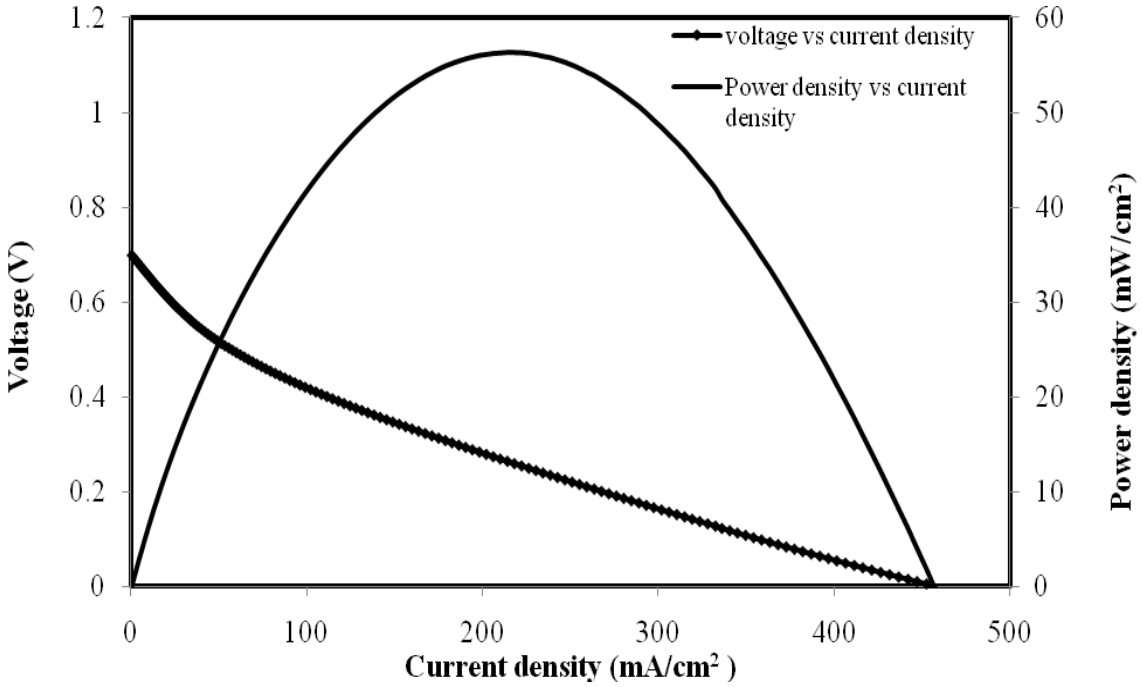

Figure 4-33: Polarization Curve at 80 ^{o}C for the MEA Sample B1

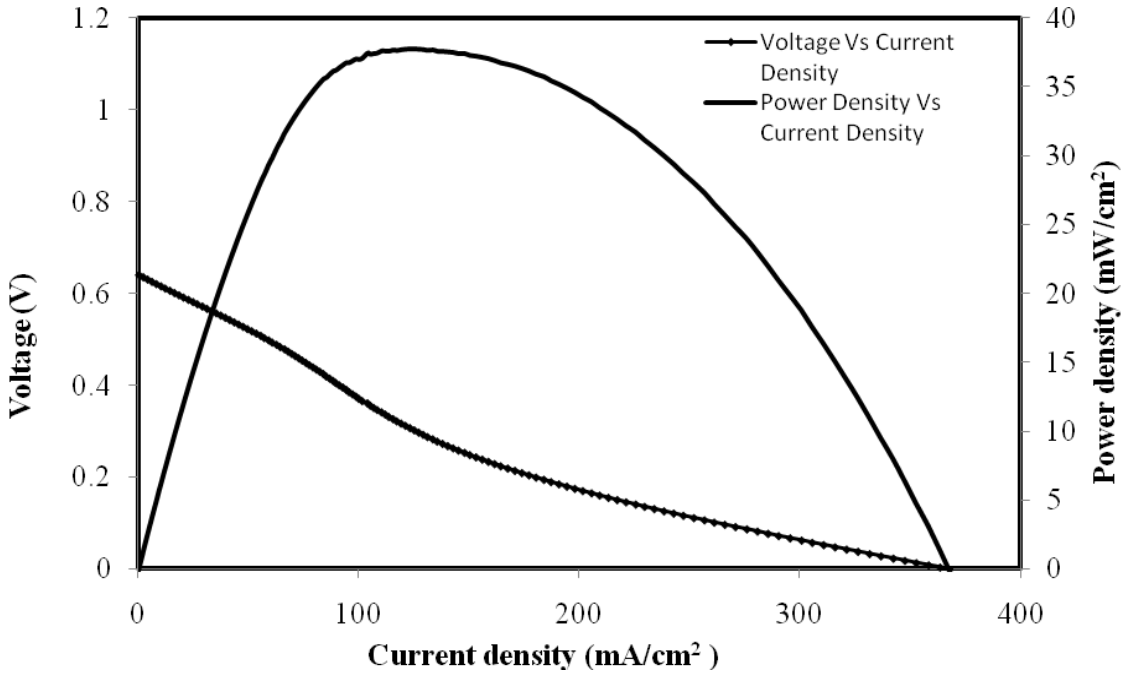

Figure 4-34: Polarization Curve at 70 ^{o}C for the MEA Sample B2

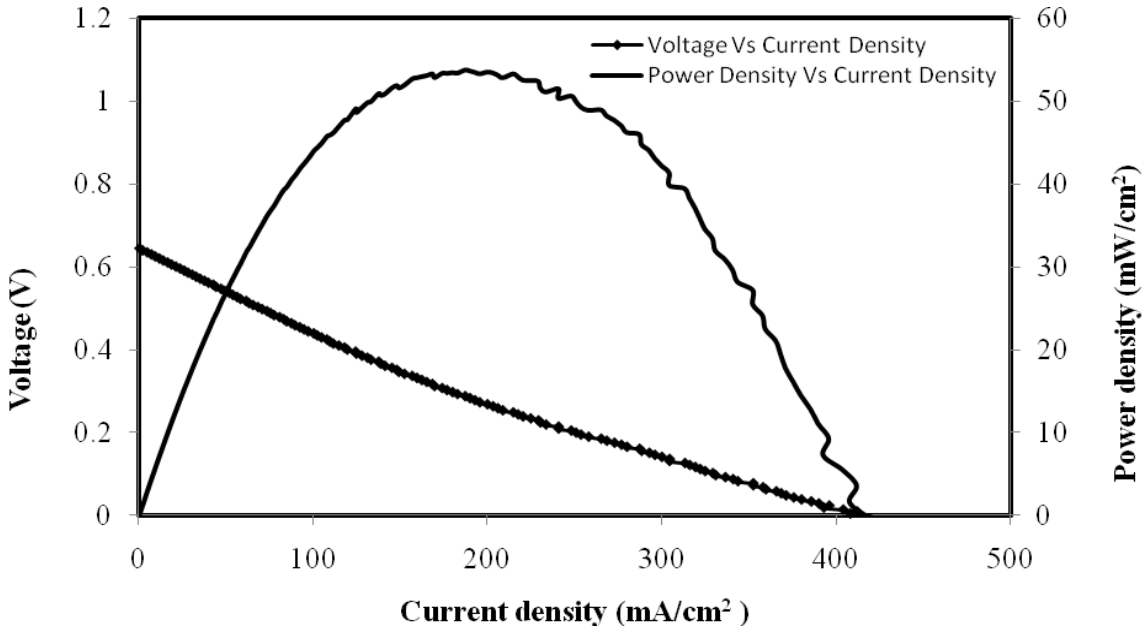

Figure 4-35: Polarization Curve at 80 ^{o}C for the MEA Sample B2

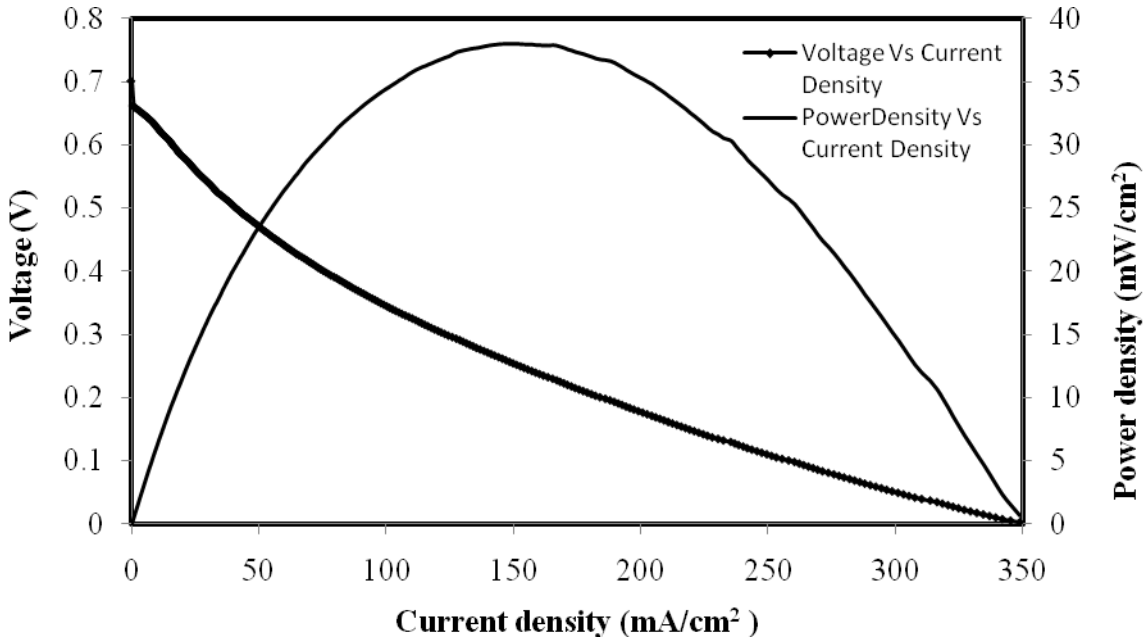

Figure 4-36: Polarization Curve at 70 °C for the MEA Sample B3

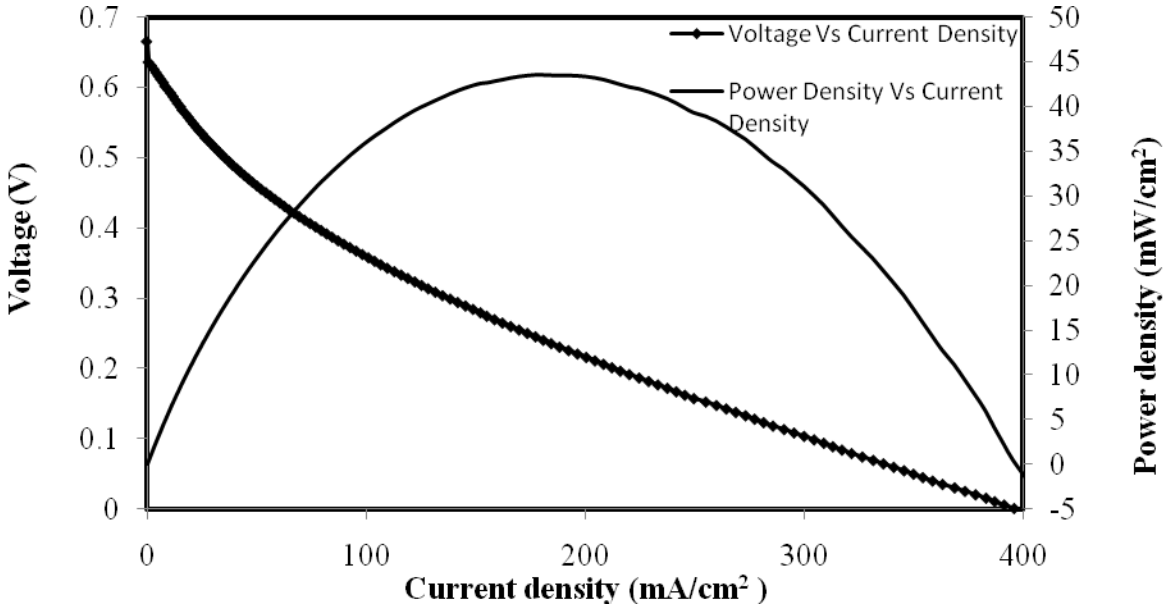

Figure 4-37: Polarization Curve at 80 °C for the MEA Sample B3

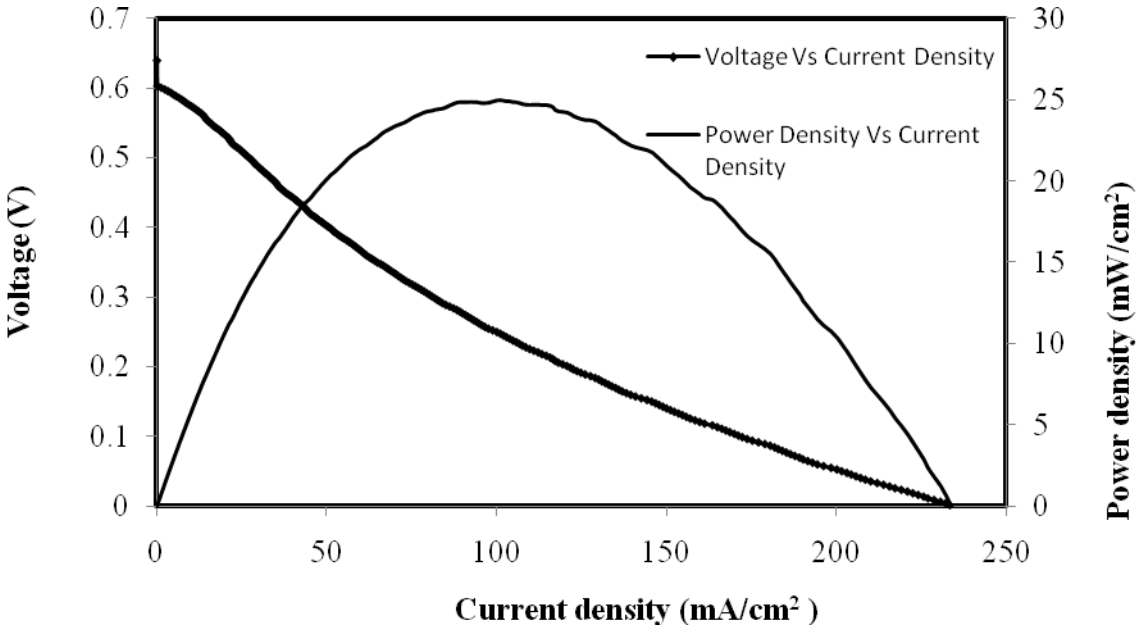

Figure 4-38: Polarization Curve at 70 °C for the MEA Sample B4

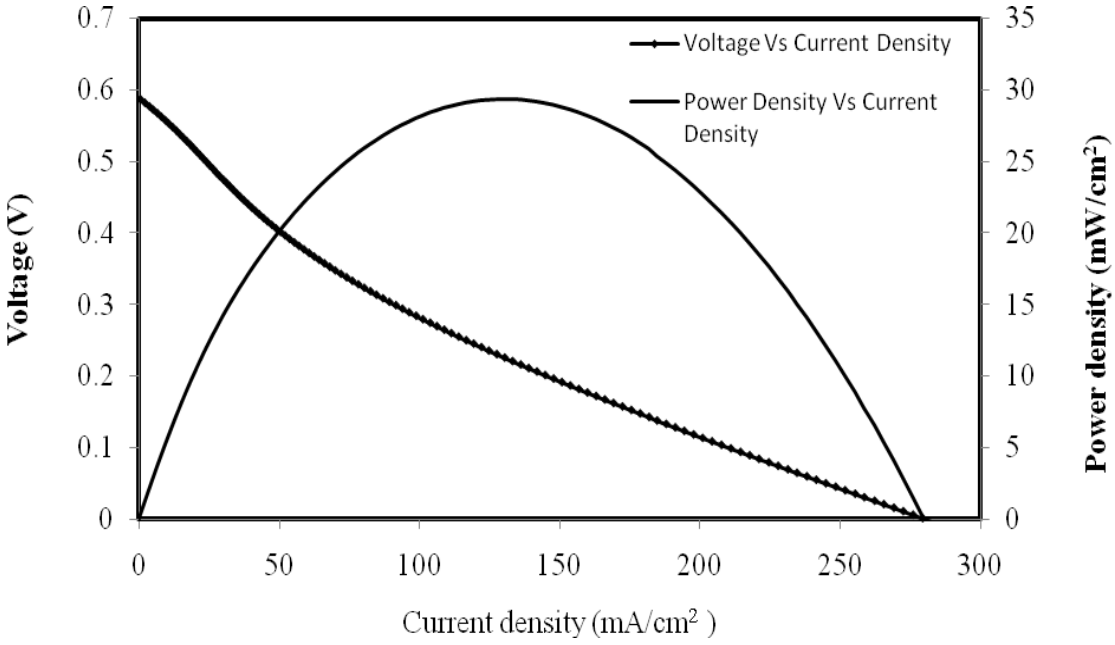

Figure 4-39: Polarization Curve at 80 °C for the MEA Sample B4

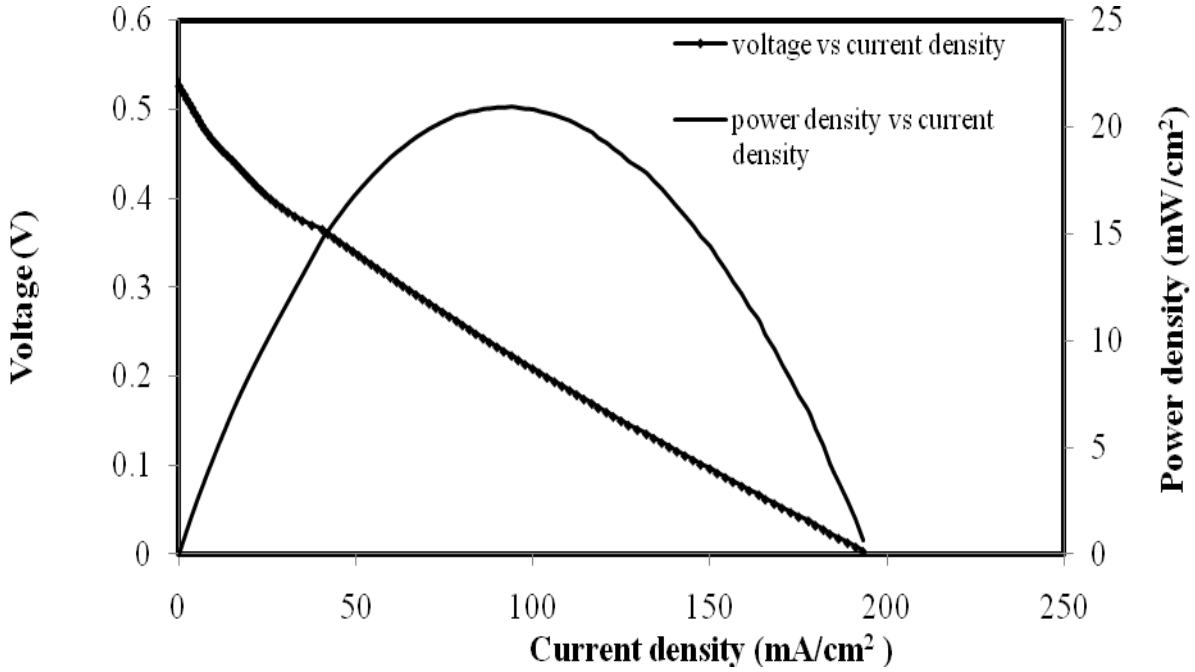

Figure 4-40 Polarization Curve at 70 ^{o}C for the MEA Sample B5

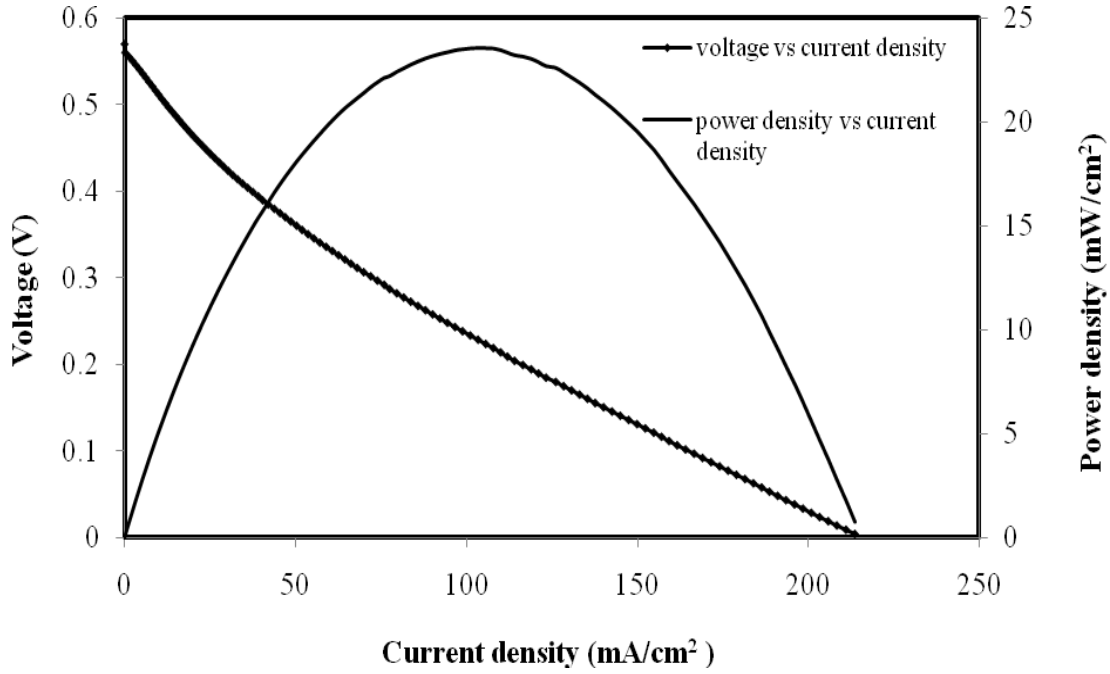

Figure 4-41: Polarization Curve at 80 ^{o}C for the MEA Sample B5

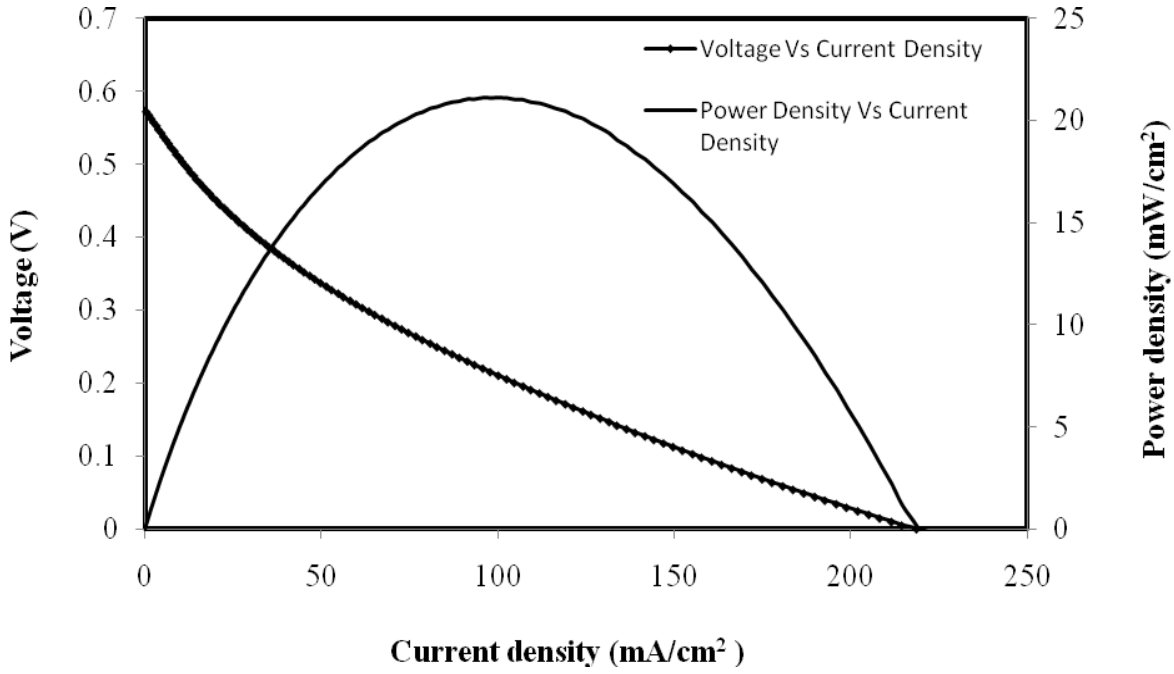

Figure 4-42: Polarization Curve at 70 °C for the MEA Sample B6

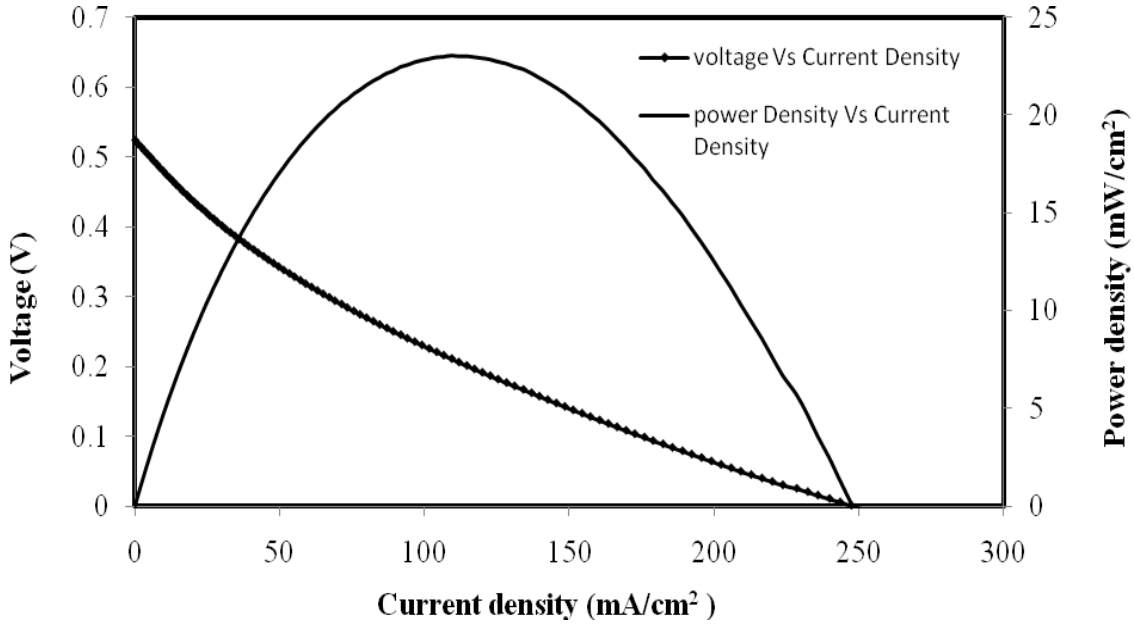

Figure 4-43: Polarization Curve at 80 °C for the MEA Sample B6

To further determine whether there is mass transport effect, a theoretical one-dimensional, steady-state, isothermal model reported in the literature was used to estimate the concentration profile within the MEAs [67]. However, a different boundary condition at the membrane/cathode catalyst layer (CCL) interface was assumed, that is, 40% of the CH_3OH that reaches the ACL/membrane interface crosses over to the membrane/CCL. The following equations were solved numerically using MATLAB to obtain the concentration profiles in the GDL, CL (of the anode) and membrane:

- GDL:

$$\frac{d^2 c_{CH_3OH}^{GDL}}{dx^2} = 0 \tag{4.6}$$

The boundary conditions are given as:

$$At\ x = 0: \qquad c_{CH_3OH}^{GDL} = c_b \tag{4.7}$$

$$At\ x = x_I: \qquad c_{CH_3OH}^{GDL} = c_I^{GDL} = \frac{c_I^{CL}}{K_I} \tag{4.8}$$

- CL

$$D_A \frac{d^2 c_{CH_3OH}^{CL}}{dx^2} = \frac{j}{6F} \tag{4.9}$$

where j is the volumetric current density (A/cm^3) given as [67]:

$$j = a I_{0,ref}^{CH_3OH} \frac{k C_{CH_3OH}^{CL}}{C_{CH_3OH}^{CL} + \lambda \exp\left(\frac{\alpha_a \eta_a F}{RT}\right)} \exp\left(\frac{\alpha_a \eta_a F}{RT}\right) \tag{4.10}$$

where a is the specific surface area of the anode (cm^{-1}), k & λ are constants, and $I_{0,ref}^{CH_3OH}$ is the exchange current density of methanol (A/cm^2).

The boundary conditions are:

$$At\ x = x_{\mathrm{I}}: \quad c_{CH_3OH}^{CL} = c_{\mathrm{I}}^{CL} \tag{4.11}$$

$$At\ x = x_{\mathrm{II}}: \quad c_{CH_3OH}^{CL} = c_{\mathrm{II}}^{CL} \tag{4.12}$$

- Membrane

The governing equation for the CH_3OH in the membrane is given as:

$$\frac{d^2 c_{CH_3OH}^{m}}{dx^2} = 0 \tag{4.13}$$

$$At\ x = x_{\mathrm{II}}: \quad c_{CH_3OH}^{m} = c_{\mathrm{II}}^{m} = \frac{c_{\mathrm{II}}^{CL}}{K_{\mathrm{II}}} \tag{4.14}$$

$$At\ x = x_{\mathrm{III}}: \quad c_{CH_3OH}^{m} = 0.4\, c_{II}^{m} \tag{4.15}$$

The CH_3OH concentration at the interfaces (C_I & C_{II}) is expressed as:

$$c_{\mathrm{I}}^{CL} = \frac{\delta_{CL} D_m K_{II}\left(D_{GDL} c_b - \frac{I_{Cell}\,\delta_{GDL}}{12F}\right) + \delta_m D_{CL}\left(D_{GDL} c_b - \left(1 + 6\xi_{CH_3OH}\right)\frac{I_{Cell}\,\delta_{GDL}}{6F}\right)}{D_{GDL} K_I\left(\delta_{CL} D_m K_{II} + \delta_m D_{CL}\right) + \delta_{GDL} D_{CL} D_m K_{II}} \tag{4.16}$$

$$c_{\mathrm{II}}^{CL} = \frac{\delta_m\left(D_{CL} D_{GDL} c_b - \delta_{CL} D_{GDL} K_I\left(1 + 12\xi_{CH_3OH}\right)\frac{I_{Cell}}{2nF}\right) - \delta_{GDL} D_{CL}\left(1 + 6\xi_{CH_3OH}\right)\frac{I_{Cell}}{6F}}{D_{GDL} K_I\left(\delta_{CL} D_m K_{II} + \delta_m D_{CL}\right) + \delta_{GDL} D_{CL} D_m K_{II}} \tag{4.17}$$

where $\delta_{GDL,}$ $\delta_{CL\ \&}$ δ_m are the GDL, CL & membrane thickness; 0.02, 0.001 and 0.02 *cm*, respectively. K_I & K_{II} are the partition coefficients (0.8), c_b is the CH_3OH bulk concentration in the flow channel (0.5 x 10^{-3} mol/cm^3), I_{Cell} is the cell current density (assumed as $0.5 A/cm^2$), ξ_{CH3OH} is the mole fraction of CH_3OH (0.0092 mol/mol), $D_{GDL,}$ D_{CL} & D_m are the CH_3OH effective diffusivities in the GDL, CL & the membrane (cm^2/s) given as [67]:

$$D_{GDL} = 8.7 x 10^{-5}\, cm^2\, s^{-1}$$

$$D_{CL} = 2.8 x 10^{-5} \exp 2436\left(\frac{1}{353} - \frac{1}{T}\right) cm^2\, s^{-1}$$

$$D_m = 4.9 x 10^{-6} \exp 2436\left(\frac{1}{333} - \frac{1}{T}\right) cm^2\, s^{-1}$$

Figure 4-44 shows the predicted concentration profiles across the MEA. From the Figure, a negligible drop in CH_3OH concentration from the bulk to the GDL/CL interface can be observed, which signifies the negligible external mass transfer resistance. In situations where the resistance is very much, it can be overcome or reduce by increasing the CH_3OH feed volumetric flow rate or decreasing its concentration.

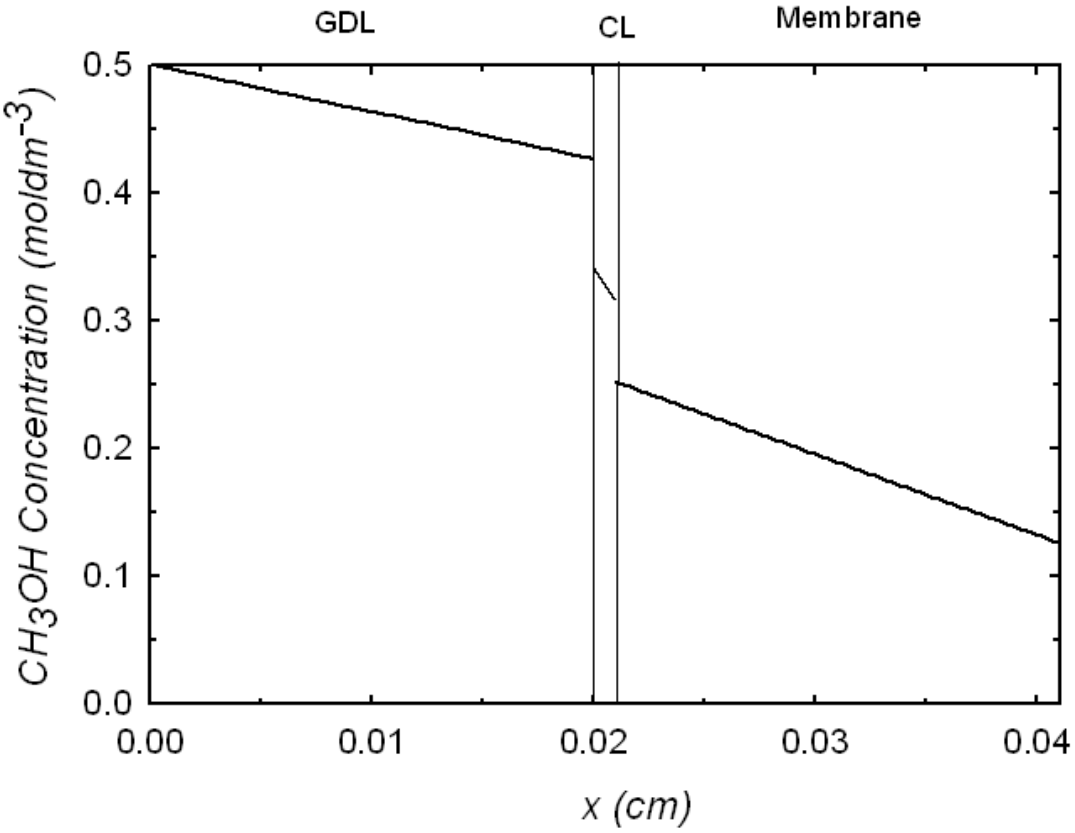

Figure 4-44: Predicted Methanol Concentration Profile across the MEAs

CHAPTER 5

5. CONCLUSION

In this work, several catalyst systems for methanol electro-oxidation reaction in direct methanol fuel cell (DMFC) were synthesized, characterized and tested. The potential of using mesoporous carbon nitride (MCN) materials as support for the methanol electro-oxidation catalysts was investigated. Initially, SBA15 at different aging temperatures of 100 °C, 130 °C and 150 °C were synthesized and used as template for the preparation of the MCN materials, denoted as MCN-100, MCN130 and MCN150. The MCN materials showed different textural properties: specific surface area, pore volume and pore diameter. However, all the MCN materials showed large pore volume and high specific surface area in the range 597 – 688 m^2/g compared to about 250 m^2/g for the commercial Vulcan XC-72 and multi-walled carbon nanotubes (MWCNTs) support materials. The prepared MCN materials, Vulcan XC-72 and functionalized MWCNTs were used as support in the preparation of catalysts for methanol electro-oxidation. Performance of the prepared catalysts (using the different support materials) for methanol electro-oxidation reaction was determined and compared with that of the commercial Pt-Ru/C (E-TEK) catalyst.

Among the prepared and screened catalysts, Pt-Ru/MCN-150 showed the highest activity, which is about 30% more than that of the commercial Pt-Ru/C (E-TEK). The variation in the catalysts performance is attributed to be mainly due to the difference in the properties of the support materials that were used. The excellent activity showed by the Pt-Ru/MCN catalysts is believed to be due to the higher surface area, large pore volume, highly interconnected uniform pore structure of the MCN support material, moderate Pt-Ru particles size and appropriate inter-distance between the PtRu-PtRu particles.

A new technique was also used in this work to synthesize high activity and less noble metals content catalysts for the methanol electro-oxidation reaction. This was achieved by synthesizing high surface area (687 – 1589 m^2/g) and large pore volume (0.72 – 1.46 cm^3/g) Fe_2O_3-MC, CoO-MC and NiO-MC. The transition metals-oxides were incorporated during synthesis of mesoporous carbon followed by impregnation with Pt and Ru active metal species to form Pt-Ru/NiO-MC, Pt-Ru/CoO-MC and Pt-Ru/Fe_2O_3-MC catalyst systems. All the prepared catalyst samples showed higher activity and lower onset potential compared to the commercial Pt-Ru/C (E-TEK). This shows that NiO, CoO and Fe_2O_3 contribute towards the methanol electro-oxidation reaction. In addition, incorporating these nano-oxides into the mesoporous carbon during the preparation stage provides large surface area for good dispersion of the Pt and Ru metal species, which also enhances the catalyst activity.

Apart from the noble and transition metals, in this work it has been shown that some rare earth metals namely: Ce, Pr, Nd, and Sm in combination with Pt have potential to

be used as catalysts for the methanol electro-oxidation reaction. The catalyst systems were prepared without using Ru and contain 15 wt% Pt only. Among the prepared and screened catalysts, that is, Pt/CeO_2-MC, Pt/PrO_2-MC, Pt/NdO_2-MC, Pt/SmO_2-MC and PtRu/C (E-TEK), the Pt/CeO_2-MC showed the highest activity, which is 3.5 % more than that of the commercial PtRu/C (E-TEK) catalyst. All the prepared catalysts show reasonable activity and stability. Thus, the prepared catalysts have potential to be used for the methanol electro-oxidation reaction in the DMFC. Table 5-1 shows all the catalyst samples prepared in this work.

From the screening (cyclic voltammetry) results, 6 (six) samples namely; Pt-Ru/MCN-100, Pt-Ru/MCN-130, Pt-Ru/MCN-150, Pt-Ru/FMWCNTs, Pt-Ru/Vulcan XC 72 and Pt-Ru/C (Commercial) were selected and used to fabricate membrane electrode assemblies (MEAs). The DMFC test results revealed that the MEA with the catalyst Pt-Ru/MCN-150 as anode showed the highest power density of 41.4 mW/cm^2 and 56.3 mW/cm^2 at 70^{o}C and 80^{o}C, respectively. This is about 2 to 2.5 times more than that of the MEA in which the commercial catalyst (Pt-Ru/C (E-TEK)) was used as the anode. All the three MEAs prepared using the MCN-based catalysts as anode showed higher power density compared to that of the MEA prepared using the commercial catalyst as an anode. Thus, the DMFC test results further confirm the superiority of the catalyst systems prepared using the MCN materials. This reveals the suitability of the MCN materials as catalysts support for methanol electro-oxidation reaction in DMFC.

Table 5-1: Summary of all the Prepared Catalyst Samples

Catalyst Sample	Mass Activity (mA/mg)	% Reduction in Mass Activity
Pt-Ru/MCN-150	14.61	38.5
Pt-Ru/NiO-MC	12.36	27.3
Pt-Ru/MCN-100	11.69	25.1
Pt-Ru/CoO-MC	11.01	22.4
Pt-Ru/F-MWCNTs	10.56	21.3
Pt-Ru/Fe_2O_3-MC	10.56	23.4
Pt/CeO_2-MC	10.56	19.1
Pt-Ru/C (Commercial)	10.11	24.43
Pt/PrO_2-MC	9.66	23.2
Pt/NdO_2-MC	9.44	23.8
Pt-Ru/MCN-130	9.44	33.4
Pt/SmO_2-MC	9.21	26.8
Pt-Ru/Vulcan XC-72	7.64	26.4

REFERENCES

1. Barbie, F., "PEM Fuel Cells: Theory and Practice*", Elsevier Inc.*, 2005.
2. Baldauf, M., Preidel, W., *Journal of Power Sources* **84** (1999) 161
3. Hammet, A., *Philos. Trans. R. Soc. London*, **A 354** (1996) 1653
4. Narayanan, S. R., Kindler, A., Jeffries-Nakamura, B., Chun, W., Frank, H., Smart, M., Valdez, T. I., Surampudi, S., Halpert, G., Kosek, J., and Creply, C., *Proceedings of 11th Annual Battery Conference Applied Advances*, **113** (1996).
5. Handbook of Fuel Cells "Fundamental Technology and Applications", *John Wiley*, **Vol. 1** (2003)
6. Bello, M., Zaidi, S. M. J, Rahman, S. U, *ECS Transactions*, **17** (1) (2009) 477
7. Bello, M., Zaidi, S. M. J, Rahman, S. U, *Journal of Membrane Science*, **322** (2008) 218
8. Bello, M., Zaidi, S. M. J, Rahman, S. U, *ECS Transactions*, **5** (1) (2007) 69
9. Zaidi, S. M. J., Mikhailenko, S.D., Robertson, G.P., Guiver, M.D., Kaliaguine, S., *Journal of Membrane Science* **173** (2000), 17
10. Ponce, M. L., Prado, L., Ruffmann, B., Richau, K., Mohr, R., Nunes, S.P, *Journal of Membrane Science*, **217** (1-2), (2003) 5
11. Chang, J. H., Park, J. H., Park, G-G., Kim, C-S., Park, O-Ok., *Journal of Power Sources* **124** (2003), 18
12. Mikhailenko, S. D., Zaidi, S. M. J., Kaliaguine, S., *Catalysis Today* **67** (2000), 225
13. Beden, B., Kardigan, F., Lamy, J. M. Leger, *Journal of Electroanalytical Chemistry* **127** (1-3) (1981) 75

14. Arico, A. S., Kim, H., Shukla, A. K., Ravikumar, M. K., Antonucci, V., Giordano, N., *Electrochimica Acta* **39** (5) (1994) 691

15. Saffarin, H. M., Srinivasan, R., Chu, D., Gilman, S., *Electrochimica Acta* **44** (8-9) (1998) 1447

16. Kabbabi, R. F., R. Durand, R., Beden, B., Hahn, F., Leger, J. M., Lamy, C., *Journal of Electroanalytical Chemistry* **444** (1998) 41

17. Zeng, J. H., Lee, J. Y., *Journal of Power Sources* **140** (2005) 268

18. Zhong, C. J., Maye, M. M., *Advanced Materials* **13** (2001), pp1507

19. Yang, L., Chen, J. H., Zhong, X. X., Cui, K. Z., Xu, Y., Kuang, Y. F., *Colloids Surface* **A295** (2007) 21

20. Markovic, M. M., Ross Jr, P. N., *Surface Science Reports* **45** (2002) 117

21. Shukla, A. K., Ravikumar, M. K., Arico, A. S., Candiano, G., Antonucci, V., Giordano, N., Hamnett, A., *Journal of Applied Electrochemistry* **25** (6), (1995) 528

22. Strasser, P., Fan, Q., Devenney, M., Weinberg, W. H., Liu, P., Norskov, J. K., Journal of *Physical Chemistry B* **107** (2003) 11013.

23. Liang, Y., Zhang, H., Zhong, H., Zhu, X., Tian, Z., Xu, D., Yi, B., *Journal of Catalysis* **238** (2006) 468

24. Jeon, M. K., Lee, K. R., Daimon, H., Nakahara, A., Woo, S. I., *Catalysis Today* **132** (2008) 123

25. Gasteiger, N., Markovic, N., Ross, P. N., *Electrochimica Acta* **41** (1996) 2587

26. Schmidt, T. J., Gasteiger, H. A., Stab, G. D., Urban, P. M., Kolb, D. M., Behm, R. J., *Journal of Electrochemical Society* **145** (1998) 2354

27. Hills, C. W., Nashner, M. S., Frenkel, A. I., Shapley, J. R., Nuzzo, R. G., *Langmuir* **15** (1999) 690

28. Iwasita, T., Hoster, H., John-Anacker, A., Lin, W. F., Vielstich, W., *Langmuir* **16** (2000) 522

29. Takasu, T., Fujiwara, T., Murakami, Y., Sasaki, K., Oguri, M., Asaki, T., Sugimoto, W., *Journal of Electrochemical Society*, **147** (2000) 4421

30. Hoster, H., Iwasita, T., Baumgartner, H., Vielstich, W., *Journal of Electrochemical Society* **148** (2001) A496

31. Kardash, D., Korzeniewski, C., Markovic, N., *Journal of Electroanalytical Chemistry* **500** (2001) 518

32. Lu, C., Rice, C., Masel, R. I., Babu, P. K., Waszczuk, P., Kim, H. S., Oilfield, E., Wieckowski, A., *Journal of Physical Chemistry B* **106** (2002) 9581

33. Lizcano-Valbuena, W. H., Pagani, V. A., Gonzalez, E. R., *Electrochimica Acta*, **47** (2002) 3715

34. Iwasita, T., *Electrochimica Acta* **47** (2002) 3663

35. Arico, A. S., Srinivasan, S., Antonucci, V., *Fuel Cells* **2** (2001) 133

36. Takasu, Y., Kawaguchi, T., Sugimoto, W., Murakami, Y., *Electrochimica Acta* **48** (2003) 3861

37. Chen, G., Lakshmi, B. B., Martin, C. R., Fisher, E. R., *Langmuir* **15** (1999) 750

38. Rajesh, B., Karthik, V., Karthikeyan, S., Thampi, K. R., Bonard, J. M., Viswanathan, B., *Fuel* **81** (2002) 2177

39. Li, W., Liang, C., Qiu, J., Zhou, W., Han, H., Wei, Z., Sun, G., Xin, Q., *Carbon* **40** (2002) 791

40. Li, W., Liang, C., Qiu, J., Zhou, W., Zhou, A., Wei, Z., Sun, G., Xin, Q., *Journal of Physical Chemistry B* **107** (2003) 6292

41. Rajesh, B., Thampi, K. R., Bonard, J. M., Xanthopoulus, N. X., Mathieu, H. J., Viswanathan, B., *Journal of Physical Chemistry B* **107** (2003) 2701

42. Li, W., Liang, C., Zhou, W., Qiu, J., Li, H., Sun, G., Xin, Q., *Carbon* **42** (2004), 436

43. Carmo, M., Paganin, V. A., Rosolen, J. M., Gonzalez, E. R., *Journal of Power Sources* **142** (2005) 169

44. Yang, L., Chen, J., Wei, X., Liu, B., Kuang, Y., *Electrochimica Acta* **53** (2007) 777

45. Ching-Fa, C., Ming-Chang, Y., Hung-Shan, W., *Journal of Power Sources* **193** (2009) 462

46. Vinu, A., *Advanced Functional Materials* **18** (2008) 816

47. Yu, J. S., Kang, S., Yoon, S. B., Chai, G., *Journal of American Chemical Society* **124** (2002) 9382

48. Chai, G., Yoon, S. B., Yu, J. S., Choi, J. H., Sung, Y. E., *Journal of Physical Chemistry B* **108** (2004) 7074

49. Chai, G., Yoon, S. B., Kang, S., Choi, J. H., Sung, Y. E., Ahn, Y. S., Kim, H. S., Yu, J. S., *Electrochimica Acta* (2004) 823

50. Raghuveer, V., Manthiram, A., *Electrochemical Solid State Letters* **7** (2004) 336

51. Raghuveer, V., Manthiram, A., *Journal of Electrochemical Society* **152** (2005) 1504

52. Watannabe, M., Zhu, Y., Uchida, H., *Journal of Physical Chemistry B* **104** (2000) 1762

53. Sivakumar, P., Tricoli, V., *Electrochem. Solid-state Letters* **9** (2006) A167

54. Wang, Z. B., Yin, G. P., Shi, P. F., Sun, Y. C., *Electrochem. Solid-state Letters* **9** (2006) A13

55. Jeon, M. K., Won, J. Y., Lee, K. R., Woo, S. I., *Electrochemistry Communications* **9** (2007) 2163

56. Takahashi, M., Mori, T., Ye, F., Vinu, A., *Journal of American Ceramic Society*, **90** (4) (2007) 1291

57. Deivaraj, T. C., Chen, W., Lee, J. Y., *Journal of Material Chemistry* **13** (2003), 2555

58. Huang, J., Yang, H., Huang, Q., Tang, T., Lu, T., Akins, D. L., *Journal of Electrochemical Society* **151** (2004) A1810

59. Xu, J., Hua, K., Sun, G., Wang, C., Lv, X., Wang, Y., *Electrochemistry Communications* **8** (2006) 982

60. Grove, W. R., "On Voltaic Series and Combination of gases by Platinum" *Philosophical Magazine and Journal of Science*, Series 3, 14, 127- 130, 1839.

61. Grove, W. R., "On a Gaseous Voltaic Battery" *London and Edinburgh Philosophical Magazine and Journal of Science*, Series 3, **21** (1842) 417.

62. http://americanhistory.si.edu/fuelcells/ Accessed November, 2010

63. Kordesch, K., Simader, G., "Fuel Cell and Their Applications", *VCH Publishers Inc*., New York, 1996, pp 151.

64. Eric, C., “Fuel Cell Technology History in Fuel Cell Technology Handbook” Gregor H., Ed., CRC Press LLC, New York, USA (2003) pp. 2-1 to 2-40
65. Handbook of Fuel Cells, “Fundamental Technology and Applications”, *John Wiley*, **Vol. 4** (2003)
66. Zhao, T. S., Xu, C., Chen, R., Yang, W. W., *Progress in Energy and Combustion Science* **35** (2009) 275
67. Brenda, L. G., Vijay, A. S., John, W. W., Ralph, E. W., Roger, D., *Journal of Fuel Cell Science and Technology*, **Vol.1** (2004) 43
68. Ota, Y., Nakagawa, M., Takahashi, *Journal of Electroanalytical Chemistry*, **179** (1984) 179
69. Beden, B., Lamy, C., Bewick, A., Kunimatsu, K., *Journal of Electroanalytical Chemistry* **121** (1981) 343
70. Wilhelm, S., Iwasita, T., Vielstich, W., *Journal of Electroanalytical Chemistry* **238** (1987) 383
71. Iwasita, T., Nart, F. C., *Journal of Electroanalytical Chemistry* **317** (1991) 291
72. Sugimoto, W., Aoyama, K., Kawaguchi, T., Murakami, Y., Takasu, Y., *Journal of Electroanalytical Chemistry* **576** (2005) 215
73. Iwasita, T., in: H. Gerischer, C. Tobias (Eds), Advances in Electrochemical Science and Engineering, **Vol. 1**, *Verlag Chemie* (1990) p127
74. Gasteiger, H., Markovic, N., Ross, P. N., Cairns, E. J., *Journal of Physical Chemistry* **97** (1993) 12020
75. Christensen, P. A., Hammett, A., Troughton, G. L., *Journal of Electroanalytical Chemistry* **362** (1993) 207

76. Xia, X. H., Iwasita, T., *Journal of Electroanalytical Chemistry* **411** (1996) 95

77. Iwasita, T., Xia, X. H., Liess, H. D., Vielstich, W., *Journal of Physical Chemistry B* **101** (1997) 7542

78. Waszczuk, P., Lu, G. Q., Wieckowski, A., Lu, C., Rise, C., Masel, R. I., *Electrochim. Acta* **47** (2002) 3637.

79. Gojkovic´, S., Vidakovic´, T. R., Durovic´ D. R., *Electrochimica Acta* **48** (2003) 3607

80. Ryan, O-H., Suk-Won, C., Whitney, C., Fritz, B. P., "Fuel Cell Fundamentals" *John Wiley & Sons Inc., Hoboken, New Jersey* (2006) p32-135

81. Bagotzky, V. S., Vassiliev, Y. B., Electrochimica Acta **11** (1966) 1439

82. Bagotzky, V. S., Vassiliev, Y. B., Electrochimica Acta **12** (1967) 1323

83. Markovic, N., Ross, P. N., Journal of Electroanalytical Chemistry **330** (1992) 499

84. Kita, H., Gao, Y., Hattori, H., Journal of Electroanalytical Chemistry **373** (1994) 177

85. Me´li, G., Le´ger, J. M., Lamy, C., Durand, R., Journal of Applied Electrochemistry **23** (1993) 197

86. Sundmacher, K., Schulz, T., Zhou, S., Scott, K., Ginkel, M., Gilles, E. D., Chemical Engineering Science **56** (2001). 333

87. Fogler, H. S., Elements of Chemical Reaction Engineering, Third Edition, *Prentice Hall International, Inc*. (1999)

88. Harvey, D., Pharoah, J. G., Karan, K., *Journal of Power Sources* **179** (2008) 209

89. Sui, J., Lu, J., Li, W. S., *Chinese Battery Industry* **9** (2004) 101

90. Teng, Z-H., Wang, G., Wu, B., Gao, Y., *Journal of Power Sources* **164** (2007) 105

91. Wan, L. J., Wu, B., Gao, Y., *Chinese Journal of Inorganic Chemistry* **20** (2004) 1108

92. Dicks, A. L., *Journal of Power Sources* **156** (2006) 128

93. Gang, W., G., Bo-Qing, X., *Journal of Power Sources* **174** (2007) 148

94. Li, L., Gang, W., G., Bo-Qing, X., *Carbon* **44** (2006) 2973

95. Chen, C. C., Chen, C. F., Chen, C. M., Chuang, F. T., *Electrochemical Communication* **9** (2007) 159

96. Girishkumar, G., Ruttier, M., Underhile, R., Binz, D., Vinodgopal, K., P. McGinn, P., Kamat, P., *Langmuir* **21** (2005) 8487

97. Davies, J. C., Bonde, J., Logadottir, A., Norskov, J. K., Chorkendorff, I., *Fuel Cells* **5** (2005) 429

98. Dinh, H. N., Ren, X., Garzon, F. H., Zelenay, P., Gottesfeld, S., *Journal of Electroanalytical Chemistry* **491** (2000) 222

99. Hyun, M-S., Kim, S-K., Lee, B., Peck, D., Shul, Y., Jung, D., *Catalysis Today* **132** (2008) 138

100. Zeng, J., Lee, J. Y., *Materials Chemistry and Physics* **104** (2007) 336

101. Wang Z-B., Yin, G-P., Shi, P-F., *Journal of Power Sources* **163** (2007) 688

102. Morimoto, Y., Yeager, E. B., *Journal of Electroanaytical Chemistry* **444**(1998) 95

103. Hepel, M., Dela, I., Hepel, T., Luo, J., Zhong, C. J., *Electrochimica Acta* **52** (2007) 5529

104. Song, H., Qiu, X., Li, F., *Electrochimica Acta* **53** (2008) 3708

105. Takahashi, M., Mori, T., Vinu, A., Oa, D. R., Kobayashi, H., Drennan, J., Advances *in Applied Ceramics*, **107**(2) (2008) 57

106. Motoi, T., Toshiyuki, M., Fei, Y., Vinu, A., Kobayashi, H., Drennan, J., *Journal of American Ceramic Society* **90** [4] (2007)1291

107. Jeon, M. K., Lee, K. R., Daimon, H., Nakahara, A., Woo, S. I., *Catalysis Today* **132** (2008) 123

108. Chen, M., Wang, Z-B., Ding, Y., Yin, G-P., *Electrochemistry Communications* **10** (2008) 443

109. Weidner, J. W., Sethuraman, V. A., Van-Zee, J. W., *The Electrochemical Society Interface*, Winter 2003, 40-43

110. Glora, M., Wiener, M., R. Petricevic, R., Probstle, H., Fricke, J., *Journal of Non-Crystal Solids* **285** (2001) 283-287

111. Litser, S., McLean, G., *Journal of Power Sources* **130** (2004) 61-76

112. Ticianelli, E. A., Derouin, C. R., Redondo, A., Srinivasan, S., *Journal of Electrochemical Society* **135** (1988) 2209–2214

113. Wilson, M. S., U.S. Patent No. 5, 234, 777 (1993)

114. Cheng, X., Yi, B., Han, M., Zhang, J., Qiao, Y., Yu, J., *Journal of Power Sources* **79** (1999) 75–81

115. Gottesfeld, S., Zawodzinski, T., *Advanced Electrochemical Science Engineering* **5** (1997) 195 – 301

116. Mehta, V., Cooper, J, S., *Journal of Power Sources* **114** (2003) 32-53

117. Valentini, L., Armentano, I., Puglia, D., Kenny, J. M., *Carbon* **42** (2004) 323

118. Lambert, J. B., Shurvell, H. F., Lighter, D. A., Cooks, R. G., Organic Structural Spectroscopy, Upper Saddle River (NJ), Prentice-Hall (1998) p205

119. Chen, C. C., Chen, C. F., Chen, C. M., Chuang, F. T., *Electrochemistry Communications* **9** (2007) 159

120. Rolinson, D. R., *Science* **299** (5613) (2003) 1698

121. Batyev, I. G., Karavanov, A. N., *Surface Science* **12** (1992) 83

122. Long, J. F., Stroud, R. M., Swider-Lyons, K. E., Rolison, D. R., *journal of Physical Chemistry B* **104** (2000) 9772

123. Hogarth, M. P., Ralph, T. R., *Platinum Metal Review* **46** (2002) 146

Cullity, B. D., "Elements of X-Ray Diffraction" Addison-Wesley, London, 1978, p.81

124. Park, G-G., Yang, T-H., Yoon, Y-G., Lee, W-Y., Kim, C-S., *International Journal of Hydrogen Energy* **28** (2003) 645

125. Rao, V., Simonov, P. A., Savinova, E. R., Plaksin, G. V., Cherepanova, S. V., Kryukova, G. N., Stimming, U., *Journal of Power Sources* **145** (2005) 178

126. Lou, Z., Wang, R., Sun, H., Chen, Y., Yang, Y., *Microporous and Mesoporous Materials* **110** (2008) 347

127. Wang, J. Xi, J., Bai, Y., Shen, Y., Sun, J., Chen, L., Zhu, W., Qiu, X., *Journal of Power Sources* **164** (2007) 555

VITAE

Name	Mukhtar Bello
Religion	Islam
Nationality	Nigerian
Date of Birth	May 15, 1974
Permanent Address	Shiyar Jagwanawa, Yabo Yabo Local Government Sokoto State, Nigeria.
E-mail	belloonline@yahoo.co.uk
Education	Bachelor of Engineering (B.ENG) in Chemical Engineering Ahmadu Bello University, Zaria, Nigeria, February, 2000. Master of Science (MS) in Chemical Engineering King Fahd University of Petroleum & Minerals, Dhahran, Saudi Arabia, May 2006. Doctor of Philosophy (PhD) in Chemical Engineering King Fahd University of Petroleum & Minerals, Dhahran, Saudi Arabia, July 2011.
Research Interests	Fuel Cells, Chemical Reaction Engineering and Environmental Pollution Control.